Investigating Star-Formation and Supernovae in Messier-82

By

Sibongumusa W. SHUNGUBE

UNIVERSITEIT VAN PRETORIA
UNIVERSITY OF PRETORIA
YUNIBESITHI YA PRETORIA
Denkleiers • Leading Minds • Dikgopolo tša Dihlalefi

Department of Physics
UNIVERSITY OF PRETORIA

Submitted in partial fulfilment of the requirements for the degree of MASTER OF SCIENCE (MSC) IN PHYSICS in the Faculty of Natural and Agricultural Sciences.

April 17, 2025

Supervisor: Dr. Jack F. RADCLIFFE (primary), Dr. David WILLIAMS-BALDWIN (co-supervisor)

© University of Pretoria

UNIVERSITY OF PRETORIA

Abstract

Faculty of Natural and Agricultural Sciences
Department of Physics

Master of Science (MSc) in Physics

Investigating Star-Formation and Supernovae in Messier-82

by Sibongumusa W. SHUNGUBE

Supervisor: Dr. Jack F. RADCLIFFE (primary), Dr. David WILLIAMS-BALDWIN (co-supervisor)

Context: Messier 82 (M82) is a well-studied nearby starburst galaxy, home to numerous compact radio sources, including supernova remnants (SNRs) and HII regions. The high star formation rate (SFR) in M82 leads to frequent supernovae (SNe), making it an ideal laboratory for studying compact radio sources in a dense starburst environment.

Aims. This thesis aims to catalog and analyze compact radio sources in the central region of M82 using new 1.5 GHz e-MERLIN observations. The study provides updated classifications for previously known sources and identifies new objects, contributing to our understanding of supernova (SN) activity and star formation (SF) in M82.

Methods. The dataset was obtained from e-MERLIN L-band observations in 2016, processed using CASA for calibration and imaging. Compact sources were detected using PyBDSF. Sources were selected based on a signal-to-noise ratio (S/N) threshold of 6, ensuring reliable detections. Spectral indices were derived from multi-frequency subband imaging and combined with existing C-band (5 GHz) flux measurements to refine classifications. Morphological analysis was also performed to distinguish between SNRs and HII regions.

Results. A total of 36 compact sources were identified, including 31 previously known objects and four newly detected sources. A key finding of this study is the reclassification of source 38.76+53.5, previously thought to be an HII region, as an SNR based on its steep spectral index (-1.054). This demonstrates the importance of multi-frequency spectral analysis in accurately identifying radio sources in starburst environments. Additionally, comparisons with previous studies from 2008 C-band observation confirmed the persistence of known sources while revealing discrepancies in classification. The spectral properties of 41.95+57.5 were further analyzed, contributing to the ongoing debate about its nature, while observations of SN 2008iz suggest it has now transitioned into a SNR. These findings refine existing classifications and contribute to a deeper understanding of the radio source population in M82. While this study does not establish a complete catalogue, it provides an updated dataset that enhances our knowledge of the physical processes shaping radio emission in starburst galaxies. Future multi-wavelength and long-term monitoring studies will be essential for further constraining the nature and evolution of these sources.

...

© University of Pretoria

Declaration of Authorship

I, Sibongumusa W. SHUNGUBE, declare that the thesis, which I hereby submit for the degree of MSc in Physics at the University of Pretoria, is my own work and has not previously been submitted by me for a degree at this or any other tertiary institution.

Signature: 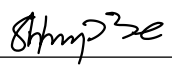

Date: 17 April 2025

© University of Pretoria

"Everyone of us is, in the cosmic perspective, precious. If a human disagrees with you, let him live. In a hundred billion galaxies, you will not find another."

Carl Sagan

© University of Pretoria

Acknowledgements

It is my great pleasure to express my deepest gratitude to all those who have supported me throughout my MSc journey and made the completion of this thesis possible.

First and foremost, I would like to extend my sincere appreciation to my advisor, Dr. Jack Radcliffe, for his exceptional guidance, patience, and unwavering support. Jack's dedication to research, teaching, and mentorship has been truly inspiring. His ability to balance rigorous scientific inquiry with a deep commitment to his students has been invaluable, and I am profoundly grateful not only for his expertise but also for his kindness and friendship. His encouragement has been instrumental in shaping both my research and my academic growth.

I am also deeply thankful to my secondary advisor, Dr. David Williams-Baldwin, whose patience and generosity with his time have been remarkable. I truly appreciate the countless conversations we had about radio interferometry and imaging techniques, as well as his willingness to assist me no matter the time zone. David's insightful advice and his readiness to support me through every challenge have been invaluable, and I am fortunate to have had the opportunity to learn from him.

I would also like to express my sincere gratitude to The National Astrophysics and Space Science Programme (NASSP) for their financial support from my Honours through to my MSc. Their sponsorship has made it possible for me to pursue my studies, and I am truly grateful for the opportunities this program has provided.

A special thank you to Theophilus Matsepane for his invaluable assistance with CASA. His willingness to help whenever I encountered difficulties made a significant difference in my research.

To my brothers at home, thank you for always being there for me. Your support meant more than I can put into words. Knowing I had people to count on made all the difference.

Lastly, I would like to express my gratitude to the MSc, PhD students, postdocs, and staff of the Department of Astronomy and Astrophysics at the University of Pretoria. The weekly journal club was a source of motivation, pushing me to challenge myself and broaden my understanding. The department became a second home, and I am grateful for the friendships, discussions, and encouragement that made this journey all the more rewarding.

To everyone who has contributed to my academic and personal growth during this time, thank you.

...

© University of Pretoria

UNIVERSITEIT VAN PRETORIA
UNIVERSITY OF PRETORIA
YUNIBESITHI YA PRETORIA

Contents

© University of Pretoria

© University of Pretoria

UNIVERSITEIT VAN PRETORIA
UNIVERSITY OF PRETORIA
YUNIBESITHI YA PRETORIA

List of Figures

© University of Pretoria

UNIVERSITEIT VAN PRETORIA
UNIVERSITY OF PRETORIA
YUNIBESITHI YA PRETORIA

© University of Pretoria

List of Tables

© University of Pretoria

UNIVERSITEIT VAN PRETORIA
UNIVERSITY OF PRETORIA
YUNIBESITHI YA PRETORIA

© University of Pretoria

This thesis is dedicated to the students who may not be the fastest, the sharpest, or the most naturally gifted—but who persist nonetheless.
This thesis is for those who fight through doubt, who struggle but refuse to surrender, who climb toward the summit of knowledge with sheer determination. May it stand as a testament that success is not reserved for the brilliant, but for those who dare to keep going…

© University of Pretoria

UNIVERSITEIT VAN PRETORIA
UNIVERSITY OF PRETORIA
YUNIBESITHI YA PRETORIA

Chapter 1

Introduction

Galaxies are a large collection of stars, gas, and dark matter bound together by gravity. The solar system that we are a part of, the stars visible at night, and the billions of other stars too faint to see with the naked eye, together with their associated planetary systems, all belong to a galaxy called the Milky Way. One of the most studied physical processes in galaxies is the rate at which massive stars form, commonly referred to as star formation rate (SFR). Star formation (SF) plays a crucial role in shaping galaxies. It consumes the gas in the interstellar medium (ISM) by forming new stars (Thackeray, 1948; Biermann, 1955; van den Bergh, 1957), influences the chemical enrichment of both the ISM and intergalactic medium (IGM), regulates energy and matter feedback within these environments, and determines the composition of stellar populations. SF serves as a bridge between the hidden universe, governed by gravity and modeled through galaxy formation theories (Katz, 1992; Springel and Hernquist, 2003; Springel, Di Matteo, and Hernquist, 2005; Stinson et al., 2006), and the observable universe, where cosmic SFRs are tracked through redshift evolution in comoving space (Madau et al., 1996; Lilly et al., 1996; Smail, Ivison, and Blain, 1997; Madau, Pozzetti, and Dickinson, 1998; Hughes et al., 1998; Steidel et al., 1999; Eales et al., 1999; Yan et al., 1999; Barger, Cowie, and Richards, 2000; Wilson et al., 2002; Giavalisco et al., 2004; Norman et al., 2004; Chapman et al., 2005; Hopkins and Beacom, 2006). Therefore, it is important to understand the laws governing SF (Kennicutt, 1998) and accurately measure the SFRs in galaxies. Unfortunately, the rate at which stars form is challenging to observe, so there is no direct measure of SFR yet. Luckily, massive stars follow a single evolutionary event that can be observed: the core collapse and subsequent supernova (SN) explosion. SN explosions are discussed in section 1.3.1, and this is when the star reaches the end of its life cycle, resulting in an explosion that injects a lot of energy into the surrounding ISM. See Fig. 1.1 for a beautiful example.

The SN explosion leaves behind a large nebula produced by the SN blast wave that expands outward from the centre of the SN into the ISM. This remnant is commonly known as a supernova remnant (SNR) and can last for hundreds up to tens of thousands of years depending on its evolutionary stage (Weiler et al., 2002).

SFR determines which class of galaxies a particular galaxy falls into. A class of galaxies called normal galaxies (Brown and Hazard, 1959) form stars at rates of a few solar masses ($M_\odot$) per year. Our Milky Way falls into this class and was estimated by Williams and McKee, 1997, to form stars at a rate of four $M_\odot$ per year.

Some galaxies form stars at exceptionally high rates, forming stars at a rate of several hundreds of $M_\odot$ per year (Larson and Tinsley, 1978). Galaxies falling into this class are the main interest of this study and are called starburst galaxies.

In a starburst galaxy, the rate of SF is so high that the galaxy consumes all of its gas reservoir, from which the stars are forming, on a time scale much shorter than the age of the galaxy (Weedman, 1987). As such, the starburst nature of a galaxy

© University of Pretoria

UNIVERSITEIT VAN PRETORIA
UNIVERSITY OF PRETORIA
YUNIBESITHI YA PRETORIA

FIGURE 1.1: Hubble Space Telescope (HST) image of supernova 1994D in galaxy NGC 4526. Image credit - NASA/ESA, The Hubble Key Project Team and The High-Z Supernova Search Team.

is a phase. The period of rapid SF can only last as long as there is sufficient gas to fuel the enhanced rate of SF and cannot be maintained for the entire lifetime of the galaxy. The SF in a starburst galaxy is often triggered by a close encounter between two or more galaxies. Merging galaxies can also result in periods of extreme SF. From simulations, the starburst resulting from mergers is believed to be a result of the tidal interactions of the galaxies that compress and shock the gas, which results in the rapid formation of stars (Barnes, 2004; Kim, Wise, and Abel, 2009; Saitoh et al., 2009). Such shock-induced SF in mergers has also been observed (Schweizer, 2009).

The central regions of starburst galaxies usually contain large quantities of dust and cannot be properly seen at optical wavelengths. Thus it is very difficult to optically detect supernovae (SNe) and SNRs that may be present in the central regions. Fortunately, radio emission, which is unaffected by dust and can penetrate through it, allows the central regions of starburst galaxies to be probed to detect SNe and SNRs, and to reveal the underlying physical processes responsible for the detected emission.

In the radio regime, star-forming galaxies emit both thermal (free-free) radiation arising from HII regions and non-thermal (synchrotron) radiation arising from acceleration of particles (usually electrons) to relativistic speeds via SN explosions (Condon, 1992; Reynolds, 2008). The emission spectra are usually dominated by non-thermal radiation (Klein and Emerson, 1981; Gioia, Gregorini, and Klein, 1982).

Fig. 1.2 shows one of the nearby starburst galaxies which has been extensively studied, the dwarf galaxy NGC 5253. The adopted distance to NGC 5253 is 2.8 Mpc (Turner, Ho, and Beck, 1998), it shows an intense nuclear starburst of luminosity 3×10^9 solar luminosity ($L_\odot$; Beck et al., 1996). Rieke, Lebofsky, and Walker, 1988, suggested that NGC 5253 has the youngest starburst known. This suggestion was based on the weak CO band head absorption. The starburst is believed to be driven by an ongoing accretion event (Turner, Beck, and Hurt, 1997, among others).

© University of Pretoria

UNIVERSITEIT VAN PRETORIA
UNIVERSITY OF PRETORIA
YUNIBESITHI YA PRETORIA

Hα (Caldwell and Phillips, 1989; Calzetti et al., 1997), infrared (IR) line (Kawara, Nishida, and Phillips, 1989), and radio observations (Beck et al., 1996) indicate that the center of NGC 5253 is now the site of an obscured, concentrated, and an extremely young burst of SF. Numerous large clusters are seen in the ultraviolet (UV; Meurer et al., 1995) and optical (Gorjian, 1996; Calzetti et al., 1997) Hubble Space Telescope (HST) images that indicate that the starburst is forming super star clusters, which are thought to be the precursors of globular clusters. NGC 5253 is of great observational interest at the present time as a nearby and well-resolved example of the starburst phenomenon.

Another nearby starburst galaxy that has been observed for decades is Messier-82 (M82). Over 50 compact radio sources have been detected in the central region of M82, with many of them concluded to be SNRs and HII regions (Kronberg, Biermann, and Schwab, 1985; Kronberg and Sramek, 1985; Kronberg, 1988; Muxlow et al., 1994; Beswick et al., 2006; Fenech et al., 2008). This is the galaxy of interest in this study and will be introduced in section 1.4 when we lay down the aim of this study.

Studying extragalactic SNRs has several advantages over studying similar SNRs in our galaxy (Milky Way). Firstly, it allows us to observe young SNRs, which can provide crucial information about the early stages of their evolution. The youngest known SNR in the Milky Way[1], G1.9+0.3, initially identified by Green and Gull, 1984, is estimated to be approximately 150 years old (Green et al., 2008) and exhibits characteristics strongly consistent with a Type Ia origin (Green et al., 2008; Reynolds et al., 2008). Type Ia SNe are relatively rare events, especially in the radio regime, where core-collapse SNe dominate (SNe types are discussed in section 1.3.1). In contrast, the youngest known SNR in M82 is just over 40 years old (Beswick et al., 2006). Secondly, the distances to SNRs in the Milky Way are uncertain, but although the relative distances between the SNRs in M82 differ by approximately a few hundred parsecs (pc), which is small compared with the overall distance of 3.4 Mpc (Freedman et al., 1994), they can effectively be treated as being at the same distance, thus providing a sample of SNRs that can be studied with essentially the same linear resolution and sensitivity. The observing tools, together with their resolution and sensitivity, are discussed in chapter 2.

[1] see Green, 2025, for an update in Galactic SNRs

© University of Pretoria

UNIVERSITEIT VAN PRETORIA
UNIVERSITY OF PRETORIA
YUNIBESITHI YA PRETORIA

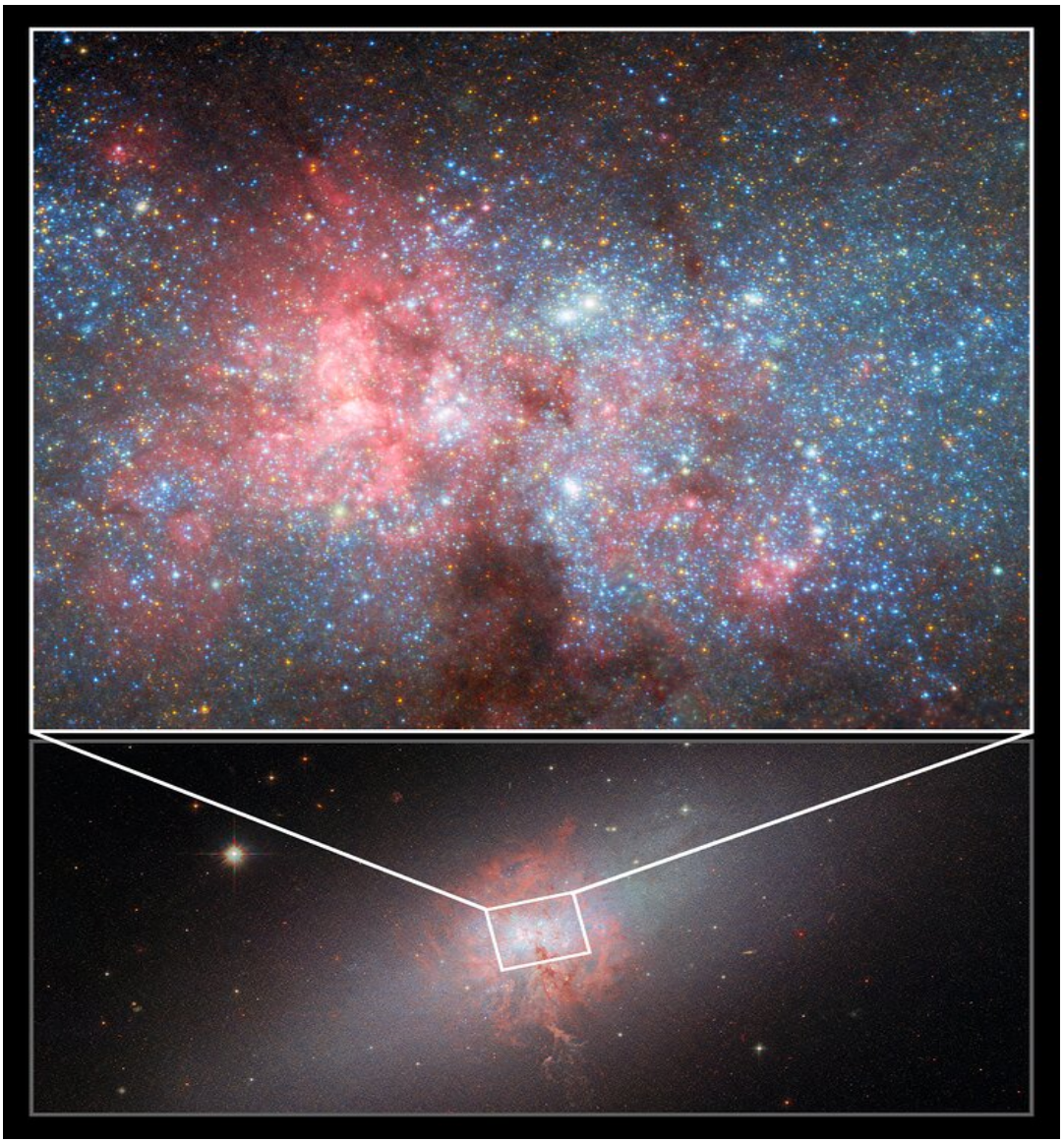

FIGURE 1.2: A composite image of the dwarf starburst galaxy NGC 5253, captured by the NASA/ESA Hubble Space Telescope (HST) over a decade. The lower portion of the montage presents a wide-field view of the entire galaxy against a dark background, revealing dense clouds of gas and dust illuminated by bright, hot star clusters. This image was created using data from Hubble's Advanced Camera for Surveys (ACS) Wide Field Channel and the older Wide Field and Planetary Camera 2. A white box outlines a specific central region of the galaxy, linked by a pullout to the upper image. The upper portion is a high-resolution close-up of NGC 5253's core, obtained using the ACS High Resolution Channel (HRC). This zoomed-in view highlights the dust-filled core and super star clusters embedded within, where intense star formation is taking place. The contrast between the detailed inset and the broader galaxy view emphasizes the intricate structure of this starburst region. Image-credit: ESA/Hubble & NASA, A. Zezas, W. D. Vacca, D. Calzetti

© University of Pretoria

UNIVERSITEIT VAN PRETORIA
UNIVERSITY OF PRETORIA
YUNIBESITHI YA PRETORIA

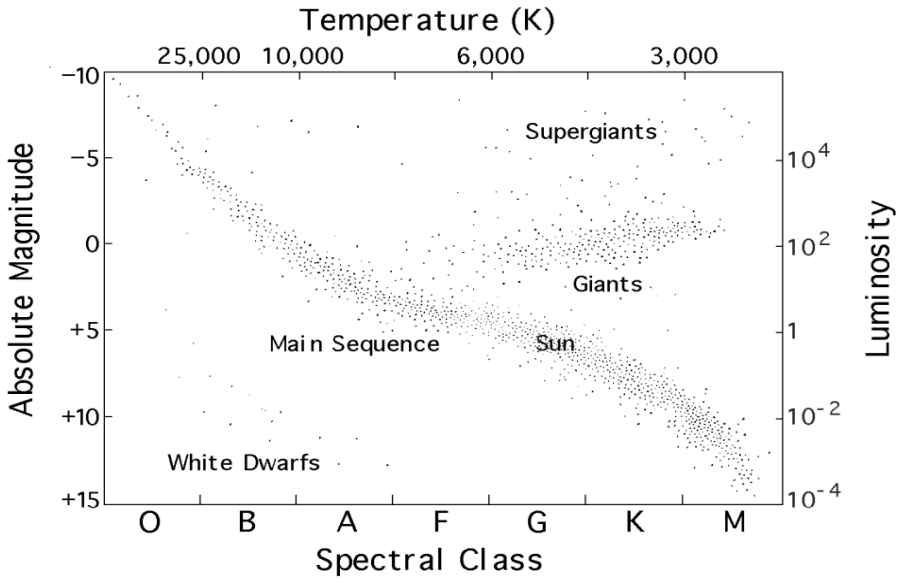

FIGURE 1.3: A Hertzsprung-Russell diagram illustrating the main sequence, where a solar-type star spends the majority of its life. Image credit - Ward-Thompson and Whitworth, 2011.

1.1 Star Formation

The Hertzsprung-Russell (HR) diagram is a key tool in understanding stellar evolution. It displays a star's luminosity in relation to its color. Most stars fall along a distinct band called the main sequence, where the hottest and most luminous stars appear blue, while the cooler and dimmer ones appear red.

Fig. 1.3 shows the location of the main sequence and where the Sun fits within it as a typical main sequence star. A star with a mass of about $M \approx 1\ M_{\odot}$ remains in this phase for most of its life, continuously fusing hydrogen into helium in its core through nuclear fusion. However, before a star reaches the main sequence phase, it has to be formed from the material in the ISM. The ISM material is gas and dust. The gas is predominantly hydrogen, whilst the dust is about 1% of the ISM mass and includes carbon compounds and silicates. SF is the conversion of gas to stars that ultimately builds all galaxies and determine the galaxy's morphology. Meanwhile, the dust causes interstellar reddening and extinction of stellar light, which makes observations at optical wavelengths more challenging.

As a star ages and depletes most of its core hydrogen through nuclear fusion, it exits the main sequence, expands into a giant or supergiant, and begins shedding mass in different stages. The most dramatic of these occurs in the most massive stars, leading to a SN explosion, as discussed in section 1.3.1. Lower-mass stars also undergo phases where they eject material. This ejected material from both SNe and lower mass stars becomes part of the ISM and is the ingredient from which the next generation of stars are formed. Hence, stars undergo a life cycle in which a new generation of stars is formed in part from the remains of the previous generation of stars.

© University of Pretoria

UNIVERSITEIT VAN PRETORIA
UNIVERSITY OF PRETORIA
YUNIBESITHI YA PRETORIA

1.1.1 Star Formation in Starburst Galaxies

The process by which stars are formed is similar in both normal and starburst galaxies. Stars form in regions of the ISM where the gas is predominantly molecular. These regions are called giant molecular clouds (GMCs). Initially, the GMCs are diffuse and turbulent, with gas particles exhibiting random motions. This random motion arises due to thermal energy, external pressure, magnetic fields, and turbulence. The gas particles in a GMC have kinetic energy due to their random motions and potential energy because they are being pulled toward each other by their mutual gravitational pull. If the cloud is stable, the kinetic energy balances the gravitational potential energy. This balance is described by the virial theorem (Ward-Thompson and Whitworth, 2011). Using this relationship, we can estimate the mass that the GMC must have to remain stable, known as the virial mass (Ward-Thompson and Whitworth, 2011).

Stars form in GMCs when the mass of the cloud exceeds its virial mass. In this case, the cloud becomes gravitationally unstable, collapses under its own gravity, contracts, and fragments into smaller, dense regions. This process, known as gravitational collapse, leads to the formation of stars or star systems within each dense, collapsed region.

Generally, in starburst galaxies there is a higher-than-normal rate of infall of gas towards the central region of the galaxy from the surrounding area. These infall rates are believed to be driven by the merger (see, e.g., Armus, Heckman, and Miley, 1990; Sanders et al., 1988a; Sanders et al., 1988b) or collision of two or more galaxies. The gravitational collapse of the gas in starbursts leads to the formation of many O-type and B-type stars. These are young and massive stars with mass $\approx 8M_{\odot}$ or more. They are both extremely hot with surface temperatures $T \gtrsim 20000$ K and extremely luminous, with $L \gtrsim 10^4\ L_{\odot}$. These are the stars leading the HR diagram shown in Fig. 1.3. These stars cannot maintain nuclear fusion for billions of years like less massive and cooler stars, leading to shorter lifespans ($\sim$ 10Myrs; Whipple, 1946). Because of their short lifespans, these stars quickly evolve into SNe (discussed in section 1.3.1), further fueling the cycle of SF.

However, before evolving into SNe, the light from newly formed stars is generally absorbed by the surrounding dust and then re-radiated at IR wavelengths (Rieke et al., 1980). This class of galaxies can be very bright in the IR, and if their IR luminosity is greater than $10^{12}\ L_{\odot}$ they are referred to as ultra-luminous IR galaxies (ULIRGs; Sanders, Surace, and Ishida, 1999). Such high IR luminosity is a diagnostic of starbursts as studies show that the great majority of the most luminous IR galaxies are made luminous by high rates of SF (Lawrence et al., 1986; Rieke and Lebofsky, 1986).

A corollary is that the characteristics of a starburst galaxy across different wavelengths are largely shaped by the starburst itself. This includes X-rays from SNRs and compact accretors linked to massive stars, UV and optical emission from dust re-radiation, and radio waves from hot gas and SNRs.

1.2 Radio Emission Processes

Starburst galaxies emit both thermal (free-free or Bremsstrahlung) and non-thermal (synchrotron) radiation in the radio regime (Condon, 1992). The thermal free-free emission originates from HII regions (discussed in section 1.3.3) surrounding young, massive stars, while the non-thermal synchrotron emission arises from relativistic electrons spiralling around magnetic fields.

© University of Pretoria

UNIVERSITEIT VAN PRETORIA
UNIVERSITY OF PRETORIA
YUNIBESITHI YA PRETORIA

1.2.1 Free-Free Radiation

Free-free emission, also known as Bremsstrahlung radiation, is a form of thermal radiation produced when free electrons are decelerated or deflected by the Coulomb fields of ions. In HII regions (discussed in section 1.3.3), this radiation arises from interactions between free electrons and positively charged ions within the photoionized gas. These regions, typically surrounding massive OB stars, are areas where intense UV radiation ionizes hydrogen gas, creating a hot, ionized plasma with temperatures around $T \sim 10^4$ K.

The process of free-free emission is governed by the density and temperature of the ionized gas. The intensity of the radiation is directly proportional to the square of the electron density (n_e) and the ion density, as well as the volume of the ionized region. The free-free absorption coefficient (κ) for an HII region can be approximated as:

$$\kappa \approx 3.3 \times 10^{-7} \left(\frac{n_e}{\text{cm}^{-3}}\right)^2 \left(\frac{T_e}{10^4\ \text{K}}\right)^{-1.35} \left(\frac{\nu}{\text{GHz}}\right)^{-2.1}, \tag{1.1}$$

Free-free emission is a critical diagnostic tool for studying the physical properties of ionized gas. In most cases, it is optically thin, producing a flat spectrum ($S_\nu \propto \nu^{-0.1}$). However, in optically thick conditions, the spectrum rises steeply ($S_\nu \propto \nu^2$). This behaviour makes free-free emission an effective tracer of the electron density, temperature, and emission measure of the gas. These parameters can be used to estimate the ionizing photon flux and, consequently, the SFR in galaxies. The strength of free-free emission correlates with the number of massive, short-lived stars that ionize the gas, making it a robust indicator of recent star formation.

In star-forming galaxies such as M82, free-free emission contributes significantly to the observed radio continuum spectrum at frequencies above the synchrotron turnover frequency. By disentangling the contributions of free-free and synchrotron emission through spectral fitting, astronomers can gain a deeper understanding of the physical processes within HII regions. Additionally, free-free emission provides a means to map the spatial distribution of ionized gas and identify compact HII regions associated with young, massive stars. Observations at radio wavelengths are particularly valuable because free-free emission is unaffected by dust extinction, allowing for a clearer view of these regions even when they are enshrouded in dense gas and dust.

At low radio frequencies, free-free absorption can also influence the spectra of both thermal and synchrotron sources, limiting their maximum brightness temperatures and shaping the overall radio spectra of normal galaxies. The observed free-free emission highlights the connection between ionized gas and star formation, providing insights into the ongoing stellar activity within the galaxy.

1.2.2 Synchrotron radiation

Generally, synchrotron radiation is emitted by relativistic electrons spiralling around magnetic field lines (Blumenthal and Gould, 1970). However, the non-thermal synchrotron radiation that is observed in starburst galaxies arises from relativistic electrons spiralling around magnetic field lines as they are being accelerated at the SNR shocks (Vink, 2012). First-order Fermi acceleration (proposed by Enrico Fermi, 1949), also known as diffusive shock acceleration (DSA), is the accepted mechanism for the acceleration of the electrons (Chevalier, 1982a; Chevalier, 1982b). The basic idea

© University of Pretoria

UNIVERSITEIT VAN PRETORIA
UNIVERSITY OF PRETORIA
YUNIBESITHI YA PRETORIA

of DSA is that the SNR shock front advances supersonically, compressing and amplifying the local magnetic field. This creates a region of enhanced magnetic field downstream of the shock. The ionized high-density circumstellar medium (CSM) contains electrons in a Maxwellian distribution. These electrons are run over by the shock front and brought downstream. The electrons in the tail of the Maxwellian distribution have sufficient energy to cross the shock and go back upstream due to the irregularity in the magnetic field. Once these electrons are back upstream, they will diffuse until they are run over again by the shock. The process repeats itself, and the electrons in the DSA process are accelerated by each crossing. This acceleration process results in the electrons accelerated to relativistic speeds, where they emit low-energy photons observed as synchrotron radiation at radio wavelengths. Bell, 1978, and Reynolds, 2008, provide a detailed review of particle acceleration at SNR shocks.

The polarizations and continuum spectrum of synchrotron radiation are unique. Synchrotron radiation is beamed. The faster the electron is moving, the larger the Lorentz factor and the narrower the beam of emission becomes (Wilson, Rohlfs, and Hüttemeister, 2013). The ultra-relativistic electrons that are needed for synchrotron emission follow a power law distribution, a non-thermal distribution. For radio synchrotron emission, newly accelerated electrons typically exhibit a power-law index of approximately $\Gamma = 2.4$, consistent with the first-order Fermi acceleration mechanism. This corresponds to a spectral index of roughly $\alpha = -0.7$ (Dulk, 1985). Magnetic fields within galactic disks tend to be more uniform in regions with low star formation activity, whereas they become more turbulent in areas with high star formation rates, such as spiral arms, regions with large HII regions, molecular clouds, or near the galactic nucleus (Condon, 1992). Below, we provide an analytical treatment of synchrotron radiation.

When a relativistic electron enters a region of a magnetic field, it experiences a force perpendicular to its velocity, which causes the electron to accelerate and travel in a helical path around the magnetic field lines. This acceleration results in a radiation of photons (Longair, 2011; Pacholczyk, 1970; Rybicki and Lightman, 1986). The highly relativistic electron loses energy at a rate given by

$$-\frac{\mathrm{d}E}{\mathrm{d}t} = \frac{4}{3}\sigma_T c U_B \gamma^2 \beta^2, \tag{1.2}$$

where σ_T is the Thompson cross-section, c is the speed of light, U_B is the energy density of the magnetic field in the ISM, γ is the Lorentz factor, and β is the velocity of the electron in units of c. The energy density of the ambient magnetic field is given by

$$U_B = \frac{B^2}{8\pi}. \tag{1.3}$$

The total power emitted at a frequency ν by a relativistic electron gyrating in a magnetic field is given by

$$P_{\text{emitted}}(\nu) = \frac{\sqrt{3}e^3 B \sin\alpha}{m_e c^2} F\left(\frac{\nu}{\nu_c}\right), \tag{1.4}$$

where e is the elementary charge of the electron, m_e is the rest mass of the electron, α is the angle between the magnetic field vector and the electron's velocity vector (the pitch angle), F is called the first synchrotron function and is an integral over an irregular modified Bessel function (a detailed description of the function F can be found in Rybicki and Lightman, 1986), and ν_c is called the critical frequency (the

© University of Pretoria

UNIVERSITEIT VAN PRETORIA
UNIVERSITY OF PRETORIA
YUNIBESITHI YA PRETORIA

frequency at which most of the power is radiated). The critical frequency is given by

$$\nu_c = \frac{3eB\gamma^2}{4\pi m_e c}\sin\alpha = \nu_0\gamma^2\sin\alpha \quad \text{with} \quad \nu_0 = \frac{3eB}{4\pi m_e c}. \tag{1.5}$$

Equation (1.4) shows that the power emitted is inversely proportional to the mass. If we consider a proton, this would explain the insignificance of proton synchrotron radiation because the rest mass of the proton is ~ 2000 times greater than that of an electron.

Equation (1.2) assumes an isotropic pitch-angle distribution of the electrons. For an isotropic distribution of electrons, we define $\mathrm{N}(p,\alpha)$ as the number of electrons per unit solid angle with momentum p and pitch angle α. Houck and Allen, 2006, show that the number of radiated photons per unit time per unit energy is

$$\frac{\mathrm{d}n}{\mathrm{d}\omega\,\mathrm{d}t} = \frac{\sqrt{3}e^3B}{hm_ec^2\nu}\int \mathrm{N}(p)R\left(\frac{\omega}{\omega_0\gamma^2}\right)\mathrm{d}p, \tag{1.6}$$

where ω is the radiated photon energy, $\mathrm{N}(p) = 4\pi\mathrm{N}(p,\alpha)$ for an isotropic pitch-angle distribution, and

$$R(x) = \frac{1}{2}\int_0^\pi \sin^2(\alpha)F\left(\frac{x}{\sin\alpha}\right)\mathrm{d}\alpha\,. \tag{1.7}$$

Equation (1.6) is known as the differential photon-emissivity spectrum.

1.3 Sources of Radio Emission

1.3.1 Supernovae

When a star reaches the end of its life cycle, it undergoes an explosion called a supernova (SN) that releases a huge amount of energy ($\sim 10^{46}$ J) and material into the surrounding ISM. The SN explosion can be either Type I or Type II, depending on the mass of the star before the explosion. During its main sequence phase, a star constantly converts hydrogen into helium at its core in a process known as nuclear fusion, while at the same time, a gravitational force constantly pulls the star's material inward, always trying to collapse it into a smaller and denser state. The pressure created as a result of nuclear fusion acts against the gravitational force to prevent the star from collapsing. As the star ages, it slowly runs out of hydrogen to convert to helium at its core, and when this fusion process slows down, it can no longer create the pressure necessary to act against the gravitational force pulling the star's material inward, it then results in a sudden core collapse. If the star has a mass greater than $8\,M_\odot$, the energy released from the core collapse results in a huge violent explosion observed as Type II SN, leading to the formation of a neutron star or a black hole. Unlike core collapse SNe, which result from the collapse of massive stars exceeding $8\,M_\odot$, Type Ia SNe arise from a different mechanism involving lower mass stars. Stars with initial masses below $8\,M_\odot$ evolve to shed their outer layers, forming planetary nebulae, and leaving behind a dense white dwarf. These white dwarfs are roughly the size of Earth, with masses below the Chandrasekhar limit of $1.4\,M_\odot$. If such a white dwarf is part of a binary system with a giant companion star, it can accrete matter from its companion. This accretion increases the white dwarf's mass. When the white dwarf's mass approaches the Chandrasekhar limit, the increasing

© University of Pretoria

UNIVERSITEIT VAN PRETORIA
UNIVERSITY OF PRETORIA
YUNIBESITHI YA PRETORIA

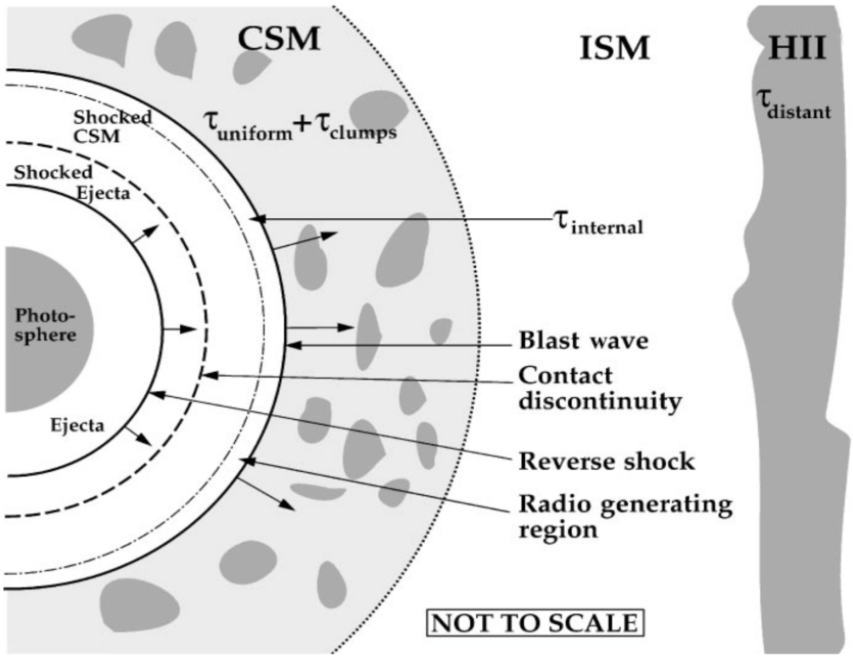

FIGURE 1.4: A schematic (not to scale) depicting a supernova (SN) and its shock waves, along with the circumstellar medium (CSM) shaped by stellar winds, the interstellar medium (ISM), and ionized hydrogen (HII) gas in the background. Radio emission is believed to originate near the blast wave front. Image credit: Weiler et al., 2002.

density and pressure trigger a runaway thermonuclear explosion, resulting in a Type Ia SN.

Type I and Type II SNe were the first division (Minkowski, 1941) and were based on whether the spectrum contained emission due to hydrogen or not. Type I spectrum shows a deficiency in hydrogen, and today, Type I SNe can be divided further into subdivisions (Ia, Ib, Ic; Sugimoto, Lamb, and Schramm, 1981; Woosley, Taam, and Weaver, 1986; Filippenko, 1997; James and Anderson, 2006). Type Ia spectrum show strong emission lines due to Si II, Type Ib spectrum show strong emission lines due to He I, and Type Ic spectrum show neither. The thermonuclear explosion described here is today generally accepted as Type Ia SNe. Type Ib and Type Ic SNe are also thought to be due to core collapse in massive stars and are more similar, in terms of the underlying physics, to Type II SNe than to Type Ia.

Most of the energy from a SN explosion is released as neutrinos, but the electromagnetic radiation, including emission and absorption spectra, provides crucial insights into their properties and classifications.

When observed at radio wavelengths, SNe are called radio supernovae (RSNe). A large number of physical properties can be determined from radio observations. Very long baseline interferometry (VLBI, discussed in Chapter 2) imaging reveals the symmetry of the SN blast wave and the structure of the local circumstellar medium (CSM). It can be used to estimate the speed and deceleration of the expanding blast wave and, under assumptions of symmetry and optical line/radio-sphere velocities, provides an independent method for determining distance (Bartel et al., 1985; Marcaide et al., 1997).

In general, RSNe are rare events. Notably, all radio-detected SNe to date have been associated with core-collapse events. The best known example is SN 1993J in

© University of Pretoria

UNIVERSITEIT VAN PRETORIA
UNIVERSITY OF PRETORIA
YUNIBESITHI YA PRETORIA

Messier-81 (M81, Martí-Vidal et al., 2011a; Martí-Vidal et al., 2011b), which has been studied extensively because of its proximity (3.63 Mpc, Freedman et al., 1994), environment (which allows for multi-wavelength observations), and galaxy orientation (M81 is seen almost face-on). In contrast, Type Ia SNe, which lack significant radio emission, remain undetected even at the sensitivity limits of instruments such as the Very Large Array (VLA; Panagia et al., 2007). Type Ib and Type Ic are radio luminous and show no radio differences, hence they are usually referred to as Type Ib/c.

The radio emission from core collapse SNe is generally modeled as originating from the interaction between the shockwave generated by the explosion and the circumstellar material produced by the progenitor's stellar wind prior to the explosion (Kirk, Duffy, and Ball, 1994). This situation is shown in Fig. 1.4, where the SN is expected to enter its SNR phase when the blast wave reaches the edge of the bubble. Hence, while SNRs are also radio-luminous, their brightness increases significantly only years after the initial explosion, resulting from the interaction between the expanding shockwave and the surrounding ISM.

As the blast wave expands, the SNR enters the Sedov-Taylor (ST) phase, also known as the adiabatic expansion phase. This phase begins when the mass of the swept-up interstellar medium (ISM) becomes comparable to the ejecta mass, and the expansion follows a self-similar solution with a radius evolving as $R \propto t^{2/5}$, where t is the age of the SNR. The shock-heated gas remains hot enough that radiative losses are inefficient, allowing the remnant to expand while conserving energy. This phase lasts for approximately 10^4 years, during which the radius of the shock grows to tens of parsecs.

Radio emission from SNe is expected to peak early in the ST phase (Parra et al., 2007). After this phase begins, the radio luminosity gradually decreases, following the surface brightness-diameter ($\Sigma - D$) relation observed in SNRs (Huang et al., 1994). During this period, Rayleigh-Taylor instabilities form at the boundary between the shockwave and the surrounding ISM, allowing RSNe to remain visible for hundreds to thousands of years. As a result, SNRs typically contribute to less than 10% of the total radio luminosity of normal galaxies, making them important tools for estimating SN rates (Condon, 1992).

All RSNe share several key characteristics. First, they emit synchrotron radiation (see section 1.2.2), which is characterized by a steeply declining spectrum, linear polarization, and a non-thermal brightness temperature. This emission arises from high-energy electrons interacting with magnetic fields (Weiler, Panagia, and Sramek, 1990). Second, the absorption of radio waves decreases over time as the SN expands and cools, causing the SN to "turn on" more quickly at shorter wavelengths and then at longer wavelengths. After the flux density stabilizes at each wavelength, a power-law decline in flux density is observed. Finally, the spectral index gradually approaches a constant negative value, indicative of optically thin, non-thermal emission (Weiler, Panagia, and Sramek, 1990).

Fitting a parameterized model

The light curve of an SN initially rises following the explosion as the material surrounding the star expands, becoming less dense and opaque. This material first becomes transparent at higher frequencies, causing the explosion to become visible at those frequencies before the light curve brightens at lower frequencies. As the envelope continues to expand, it cools. Eventually, the material no longer emits sufficient heat to be detectable at optical wavelengths, leading to the supernova fading from view.

© University of Pretoria

UNIVERSITEIT VAN PRETORIA
UNIVERSITY OF PRETORIA
YUNIBESITHI YA PRETORIA

For sources that are RSNe, whether Type Ib/c or Type II, their radio light curve can now be modelled. The radio emission is believed to originate from a spherical shell located just behind the blast wave, where it interacts with the CSM. This emission is non-thermal synchrotron radiation produced by free electrons and the amplified magnetic fields generated by the shock wave's interaction with the CSM.

The variation of radio flux density S (in mJy) over time t can be modelled using a parameterized light curve of the form proposed in Weiler et al., 2002,

$$S(\text{mJy}) = K_1 \left(\frac{\nu}{5\,\text{GHz}}\right)^{\alpha} \left(\frac{t-t_0}{1\,\text{day}}\right)^{\beta} e^{-\tau_{\text{external}}} \left(\frac{1-e^{-\tau_{\text{CSM}_{\text{clumps}}}}}{\tau_{\text{CSM}_{\text{clumps}}}}\right), \tag{1.8}$$

where ν is the observing frequency in GHz, α is the spectral index, β is a time constant, t_0 is the date of explosion, τ_{external} and $\tau_{\text{CSM}_{\text{clumps}}}$ are the optical depths due to external media and clumpy components in the CSM. The optical depth due to external media, τ_{external}, is given by

$$\tau_{\text{external}} = \tau_{\text{CSM}_{\text{uniform}}} + \tau_{\text{distant}}\,, \tag{1.9}$$

where $\tau_{\text{CSM}_{\text{uniform}}}$ and τ_{distant} are the optical depths due to uniform CSM and distant uniform ISM. The optical depth due to uniform CSM is given by

$$\tau_{\text{CSM}_{\text{uniform}}} = K_2 \left(\frac{\nu}{5\,\text{GHz}}\right)^{-2.1} \left(\frac{t-t_0}{1\,\text{day}}\right), \tag{1.10}$$

and the optical depth due to a uniform absorbing medium at some large distance from the explosion, τ_{distant}, is given by

$$\tau_{\text{distant}} = K_4 \left(\frac{\nu}{5\,\text{GHz}}\right)^{-2.1}, \tag{1.11}$$

and the optical depth from the clumpy CSM, τ_{clumps}, given by

$$\tau_{\text{CSM}_{\text{clumps}}} = K_3 \left(\frac{\nu}{5\,\text{GHz}}\right)^{-2.1} \left(\frac{t-t_0}{1\,\text{day}}\right)^{\delta'}, \tag{1.12}$$

where K_1, K_2, K_3 and K_4 are constants corresponding to flux density (K_1), absorption due to uniform CSM (K_2), clumpy CSM (K_3) and uniform distant ISM (K_4), at 5 GHz and one day after the explosion.

In cases where well-sampled data are unavailable and fitting the full model is not feasible, this model can be simplified by including only the K_1 and K_2 absorption terms. A more detailed discussion of radio emission from SN explosion and models describing the shock/ISM interactions that produce it, can be found in Weiler et al., 2002, and the references therein.

1.3.2 Supernova Remnants

Supernova remnants (SNRs) are the structures formed from the explosion of a star in a SN event, which results in a shockwave interacting with the surrounding ISM. SNRs are typically large, with sizes ranging from 1 to 100 parsecs, and they generally exhibit only small variations in flux density over time. Due to the nature of their expansion and interaction with the surrounding environment, SNRs are often identified by their characteristic radio emission, which is usually non-thermal and can appear as compact sources as seen in high resolution images of starburst galaxies

© University of Pretoria

UNIVERSITEIT VAN PRETORIA
UNIVERSITY OF PRETORIA
YUNIBESITHI YA PRETORIA

like M82 (Kronberg, Biermann, and Schwab, 1985; Muxlow et al., 1994; Fenech et al., 2008).

These remnants are classified as either young or older, with young SNe showing rapid variations in flux density, which is not always observed in many SNRs. In fact, many compact objects in galaxies like M82 do not exhibit the flux density variations required to be considered young SNe, and are therefore categorized as older remnants. The radio emission from SNRs often forms shell-like or partial-shell structures, with the radio emission concentrated along the outer edges of the remnant.

Observations using high-resolution radio techniques, such as VLBI, provide detailed insights into the size, structure, and expansion velocities of SNRs, helping to refine our understanding of their role in stellar evolution and the dynamics of the host galaxy.

The expansion velocities of SNRs can vary, with some remnants exhibiting significant expansion over time. For instance, the shell radius of an SNR can increase significantly over a decade or more, providing valuable information on the physical processes occurring within the remnant. Additionally, the size and velocity measurements of these remnants allow astronomers to estimate the SN rate within a galaxy, which can then be used to infer the SFR and the overall dynamics of the galaxy's central region. This method of calculating SN rate in this way has been employed (Muxlow et al., 1994).

1.3.3 HII Regions

HII regions are sharply defined regions of photo-ionized gas. The Orion Nebula, shown in Fig. 1.5, is a beautiful example. It is the brightest and best-studied HII region, serving as a focal point for numerous astrophysical studies (O'Dell, 2001).

The ionizing photons in HII regions typically originate from high-mass O-type and B-type stars, which are predominantly found in OB associations or clusters (Ward-Thompson and Whitworth, 2011). These OB associations, characterized by their significant populations of O and B stars, are the primary sites of extended HII regions. Given the relatively short main sequence lifetime of OB stars ($\sim$ 10 Myrs; Whipple 1946), HII regions are concentrated near sites of recent and ongoing SF, within GMCs, and along the spiral arms of disc galaxies. Consequently, much of the visible light observed at optical wavelengths in the spiral arms of galaxies is emitted by HII regions.

When an OB star (or a group of such stars) first forms, it is often buried deep within a GMC, surrounded by the remnants of the accretion envelope from which the star has grown (and may still be growing). As a consequence, the gas surrounding the OB star is very dense, and the HII region it excites is compact. These compact HII regions are not visible when observed at optical wavelengths due to dust in the surrounding gas but are detectable at radio wavelengths, as radio waves are not attenuated by dust (Condon, 1992; see Fig. 1.6 for a radio free-free image of the Orion Nebula).

HII regions form as a result of two fundamental competing processes that also determine the degree of ionization within an HII region: photo-ionization and radiative recombination. Generally, in photo-ionization, neutral atoms absorb photons with sufficient energy to eject an electron, as a result, leaving behind a positively charged ion. If the photon energy is more than the energy required to ionize the atom, the excess energy is transferred to the ejected electron as its kinetic energy. Radiative recombination, on the other hand, occurs when free electrons are captured by positively charged ions, emitting photons corresponding to the energy difference

© University of Pretoria

UNIVERSITEIT VAN PRETORIA
UNIVERSITY OF PRETORIA
YUNIBESITHI YA PRETORIA

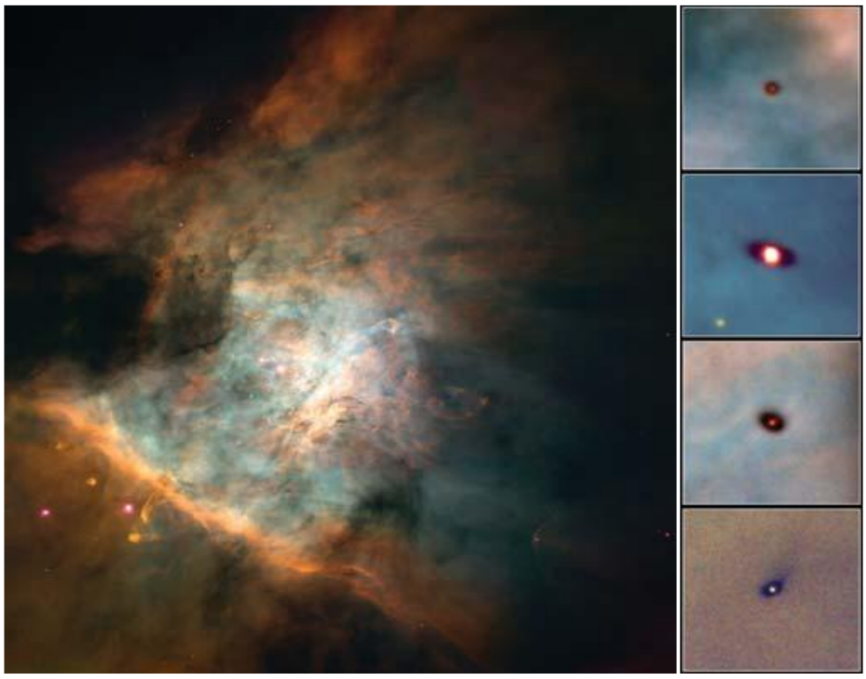

FIGURE 1.5: Center of the Orion Nebula, imaged by the Hubble Space Telescope (HST). The bright Orion Bar is an edge-on ionization front separating neutral gas at lower left from the HII region. Red=[NII]6584, gren=H α, blue=[OIII]5008. The four trapezium stars near the image center. See Fig. 1.6 for a radio free-free image. At right are images of four protoplanetary disks silhoutted against the HII region: each image is $\sim 4''$ wide (1700 AU/414 pc). Image-credit: NASA, C.R. O'Dell and S.K. Wong (Rice University), and M.J. McCaughrean (MPIA)

between the free and bound states. Photo-ionization dominates near the star, creating an ionized region, while radiative recombination becomes significant further out, defining the boundary of the ionized region.

To illustrate, consider a species X (atom, ion, or molecule) within the gas surrounding the star with two energy levels, labelled i and j, having energies E_i and E_j, where $E_j > E_i$. The energy difference $h\nu_0 = E_j - E_i$ corresponds to the photon energy required to ionize the atom. Here, h is Planck's constant, and ν_0 is the photon frequency. Photo-ionization occurs when a photon with energy $h\nu_0$ or higher removes an electron from the atom, hence ionizing the atom. Radiative recombination reverses this process, capturing a free electron into a bound state and releasing a photon of energy $h\nu_0$. The two processes compete with each other, one ionizing the surrounding gas and the other neutralizing the gas, until they establish an equilibrium that determines the overall ionization state and the boundary of the ionized region.

Neutral hydrogen (HI) is the most abundant gas around massive OB stars, with an ionization energy of 13.6 eV. Massive stars emit photons in the UV, and those with energies exceeding 13.6 eV are known as Lyman continuum photons (LyC). These LyC photons primarily ionize HI through photo-ionization, creating ionized hydrogen regions known as HII regions. While radiative recombination of hydrogen ions does occur, it is a separate process and not directly caused by the LyC photons

© University of Pretoria

UNIVERSITEIT VAN PRETORIA
UNIVERSITY OF PRETORIA
YUNIBESITHI YA PRETORIA

themselves. The balance between photo-ionization and radiative recombination determines the extent of the ionized region, which is traditionally modelled as a Stromgren sphere (Wilson and Downes, 1975).

HII regions are identified by their flat spectra, with an index of $\alpha \sim -0.1$ (McDonald et al., 2002). In M82, these regions are believed to be linked to SF. Hubble Space Telescope (HST) observations suggest that many of these regions are associated with super-star clusters, where OB stars supply the ionizing radiation (Fenech et al., 2008). As a result, these regions are thermal, emitting free-free radiation from ionized gas (McDonald et al., 2002). Fenech et al., 2008, identified 13 H II regions in M82, with an average diameter of 3.1 pc, making up about a quarter of the compact sources in the galaxy (McDonald et al., 2002).

© University of Pretoria

UNIVERSITEIT VAN PRETORIA
UNIVERSITY OF PRETORIA
YUNIBESITHI YA PRETORIA

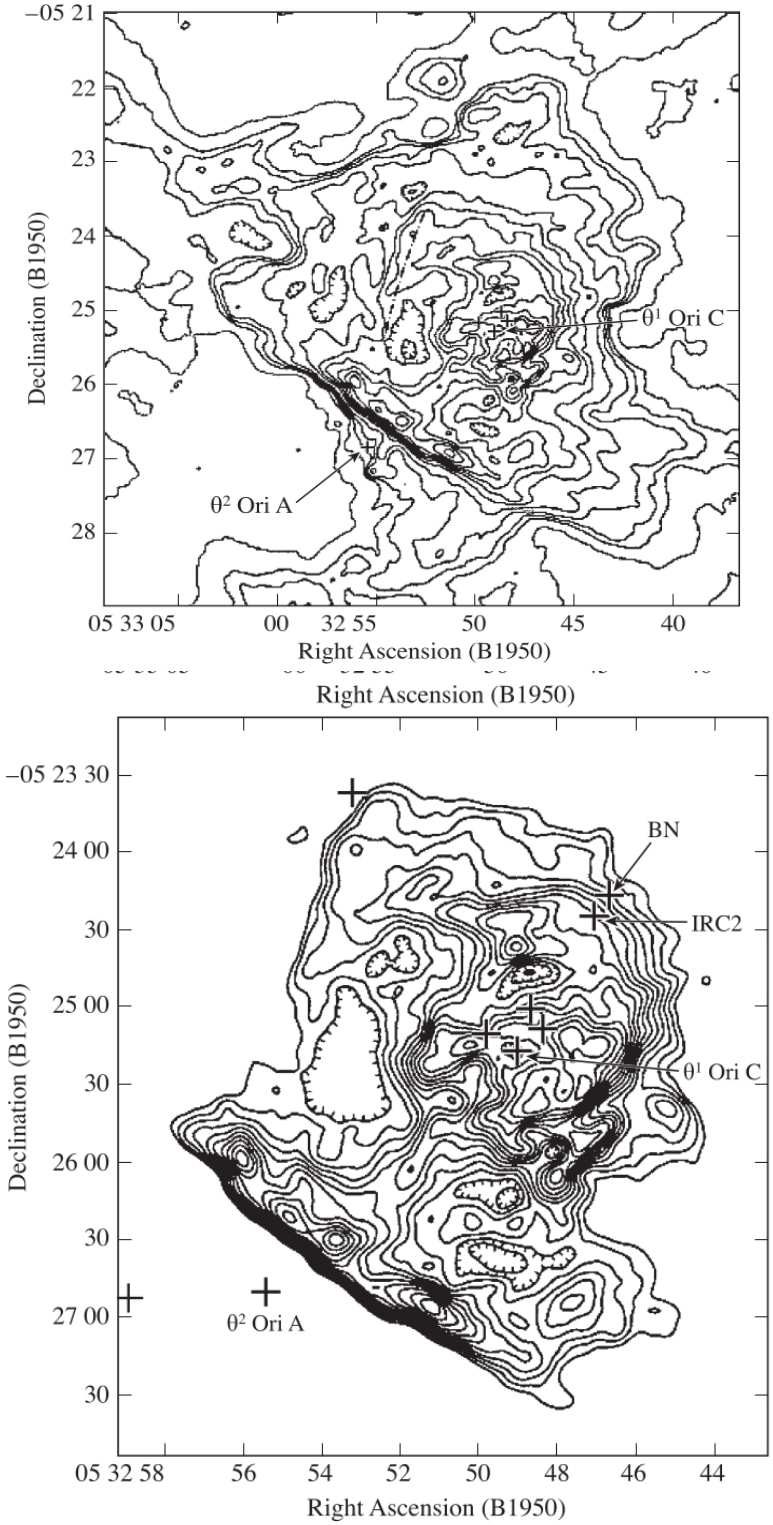

FIGURE 1.6: Maps of the Orion Nebula (M42) at $\lambda = 20$ cm, with a half-power beam width (HPBW), which represents the angular resolution of the observations, of $\approx 6.2''$. The Orion Bar ionization front is $\sim 110''$ SE of θ^1 Ori C, with a projected separation of 0.22 pc = 6×10^{17} cm. The lower map is an expanded view of the brightest region, with only the brightest contours shown. Image credit: Felli et al., 1993.

© University of Pretoria

UNIVERSITEIT VAN PRETORIA
UNIVERSITY OF PRETORIA
YUNIBESITHI YA PRETORIA

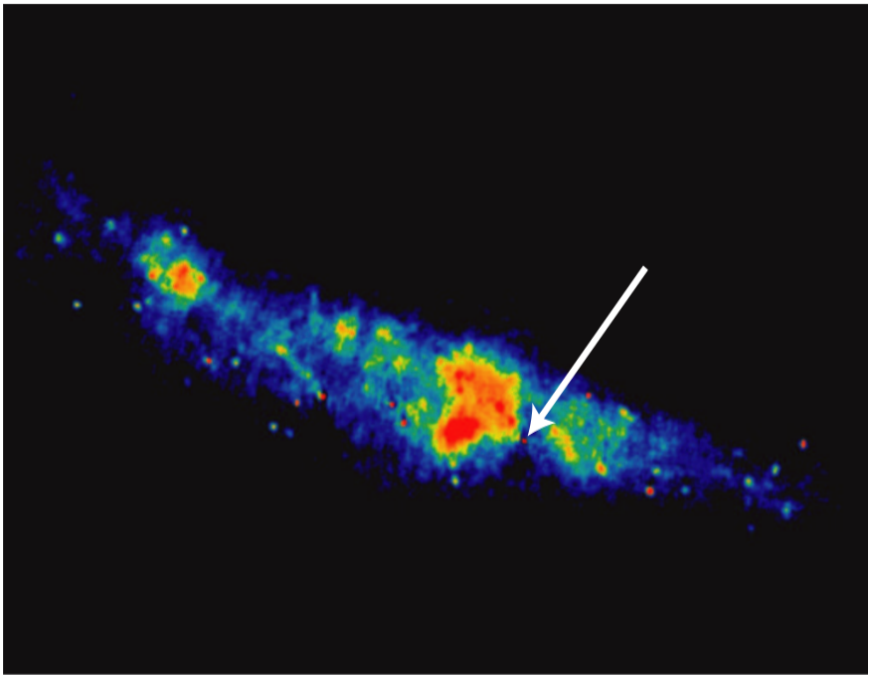

FIGURE 1.7: A combined MERLIN + VLA 5 GHz image of M82 with 41.95+57.5 indicated by the arrow. Image credit - Muxlow et al., 2005.

1.4 Thesis aim

Messier-82 (M82) is one of the most studied and most enigmatic galaxies known today. It is a member of the local group and is classified as an irregular type II. As expected for starbursts to be a result of a close encounter between two or more galaxies, it is believed that M82 interacted gravitationally with its neighbour Messier-81 (M81), 35 kpc away, over the last 1-2 $\times 10^8$ years, and that the interstellar gas was drawn into the region between the two galaxies. The supporting evidence from Yun, Ho, and Lo, 1994, discusses some clear signs of tidal interaction between M82 and M81. Also, Gottesman and Weliachew, 1977, Cottrell, 1977, and Crutcher, Rogstad, and Chu, 1978, discovered non-circular motion of neutral hydrogen (HI) on a kpc scale around M82, which also suggests the presence of gas between the galaxies. This gas falling into the central regions of M82 is believed to be triggering SF (O'Connell and Mangano, 1978), which in turn gives rise to SNe, which creates and accelerate cosmic rays (CRs) producing the synchrotron radiation (Hargrave, 1974). M82 is approximated in Freedman et al., 1994, to be at a distance of 3.4 Mpc based on a Cepheid distance to M81.

M82 is home to many bright compact radio sources in its central region. MERLIN and VLA observations, which employ the technique of very long baseline interferometry (VLBI; discussed in chapter 2), identified a population of over 50 objects which are SNRs and HII regions (Kronberg, Biermann, and Schwab, 1985; Kronberg and Sramek, 1985; Kronberg, 1988; Muxlow et al., 1994; Beswick et al., 2006; Fenech et al., 2008).

Fig. 1.7 shows the compact nature of SNRs and HII regions in the central region of M82 when imaged using VLBI. The arrow points to a source named (following the B1950 convention) as 41.95+57.5. This is a source which has attracted many observers due to its unusual morphological features, and will be discussed in this

© University of Pretoria

UNIVERSITEIT VAN PRETORIA
UNIVERSITY OF PRETORIA
YUNIBESITHI YA PRETORIA

study as well. In this study we create an image similar to Fig. 1.7 using the 2016 e-MERLIN L-band data set, except our image will not show the diffuse emission. The data set, the data reduction steps and the imaging process are described in chapter 2. The final image, out of which individual sources will be extracted and discussed, will enable M82 to be studied in greater depth, providing analysis of the physical processes responsible for the observed emission in the starburst.

This thesis aims to create a new catalogue of sources within the star-forming central region of M82. Each source in the catalogue will be labelled as either SNR or HII region. SNe are rare events, but they will also be labelled where possible. We do not produce a complete catalogue for M82 as it is unclear what the actual number of sources in M82 is from previous observations (Kronberg, Biermann, and Schwab, 1985; Kronberg and Sramek, 1985; Kronberg, 1988; Muxlow et al., 1994; Beswick et al., 2006; Fenech et al., 2008). This is due to the sensitivity and resolution of the images and equipment. However, by cataloguing these sources, it gives us information on the environment from which these sources are formed. It also gives us information to do spectral studies (especially since there aren't many L-band fluxes for some of the objects) and allows us to find new transient objects. M82 is an ideal candidate for such studies due to its close proximity.

1.5 Thesis Outline

Chapter 2 describes the basic principles of radio interferometry, gives the description of the e-MERLIN interferometer as it is used in this study, gives a desciption of the data obtained from observation, and a description of the imaging process.

Chapter 3 describes the process used to catalogue the sources. Peak flux density, integrated flux density, and size for each source are summarized. Contour maps of each source are also presented here. In section 3.1 of this chapter, the source fluxes are used to compute source luminosities. In section 3.2 the process of calculating spectral indices is presented and used together with morphological analysis of the contour maps to obtain final classification of each source.

Chapter 4 discusses the results obtained in chapter 3 for further analysis. Comparisons with previous studies is done to search for possible misclassification and to confirm some of the classification. Newly detected sources are also discussed here. Section 4.3 and section 4.4 of this chapter describes the calculated values for SN rate and SFR in M82 as obtained in this study.

© University of Pretoria

UNIVERSITEIT VAN PRETORIA
UNIVERSITY OF PRETORIA
YUNIBESITHI YA PRETORIA

Chapter 2

Radio Interferometry

Starburst galaxies, despite being sites of intense star formation (SF), are not particularly bright in visible light. This is because their starburst regions are often dense and surrounded by dust that absorbs visible light. Fortunately, radio waves can penetrate through the dust to reveal the underlying physical processes. However, many of the sources of radio emission in these galaxies, such as HII regions and supernova remnants (SNRs), are confined to small angular extents and a resolution much higher, of about 10^{-4} to 10^{-1} arcsec, is needed to understand the underlying physical processes of the radio sources. The resolution of a single dish telescope is limited by diffraction, approximated as,

$$\theta \sim \frac{\lambda}{D}, \tag{2.1}$$

where λ is the observing wavelength, and D is the diameter of the telescope. It soon becomes clear that building a single-dish telescope large enough to provide the resolutions required at radio wavelengths is almost impossible. One of the reasons why that is so is because the structure would have to be strong enough to support its weight without deforming, which becomes very difficult as the size grows. A telescope requires its surface accuracy to be precise within a fraction of the wavelength it observes. Therefore, maintaining the necessary surface accuracy over a structure kilometres in size becomes nearly impossible or very difficult. Also, the cost of building such a single-dish telescope, the environmental factors, and the technological limitations (such as the receivers needed to cover the surface) make it impractical to build a single-dish telescope. Aperture synthesis (Hogbom and Brouw, 1974; Bajaja and van Albada, 1979; Napier, Thompson, and Ekers, 1983) is a solution to the resolution problem. This technique uses a collection of single-dish telescopes (usually referred to as antennas) distributed in such a way that they synthesize a telescope whose effective diameter is the largest distance between any pair of antennas in the array. This distance is referred to as a baseline. Very long baseline interferometry (VLBI; Borkowski and Kus, 1983) is a technique that allows the baselines up to thousands of kilometres (Napier et al., 1994; Dewdney et al., 2009; Zensus and Ros, 2015), obtaining much better resolution.

From this point forward, a single-dish telescope will be referred to as an antenna, and the array of antennas that make up the synthesized telescope will be referred to as an interferometer. Using an array of antennas to synthesize an interferometer solves the resolution problem but also has drawbacks. One major drawback is that the interferometer's sensitivity is reduced, especially for astronomical sources with large angular extent. That is because sensitivity depends on the collecting area of a telescope. For an antenna, the collecting area is the parabolic dish, and for the interferometer, the collecting area is the sum of the effective collecting areas of the antennas. So, the antennas in the array act as an unfilled aperture or a gigantic

© University of Pretoria

UNIVERSITEIT VAN PRETORIA
UNIVERSITY OF PRETORIA
YUNIBESITHI YA PRETORIA

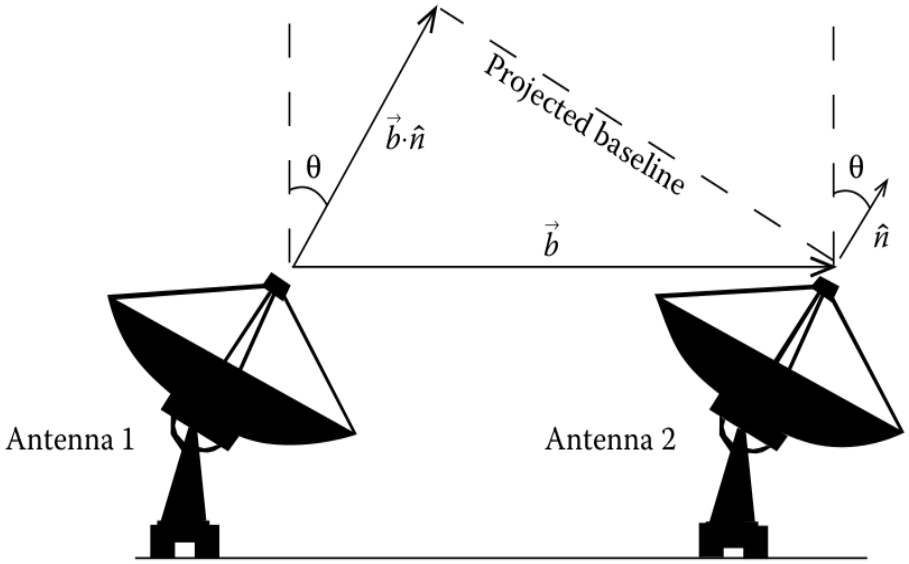

FIGURE 2.1: Diagram of a two-element interferometer. The baseline vector, $\vec{b}$, gives the distance and direction between the antennas and the unit vector, $\hat{n}$, indicates the direction of the source. The dot product, $\vec{b} \cdot \hat{n}$, is the extra path length that the signal must travel to reach antenna 1. The dashed line represents the projected baseline length. Image credit - Marr, Snell, and Kurtz, 2015.

parabolic dish with holes. The consequence is that it requires a long observation time to get meaningful images.

The basic unit of an interferometer is the two-element interferometer. Section 2.1 explains the two-element interferometer's working principles to give foundation for the techniques used to obtain the data explored in this work. Most results will be stated without derivation, and some without mathematical formulas[1].

Section 2.2 introduces the enhanced Multi-Element Radio-Linked Interferometer Network (*e*-MERLIN; Garrington et al., 2004) located in the United Kingdom. This is the interferometer used to obtain the data set being explored in this work. The concepts in the following discussions are generally described and apply equally well to any interferometer. However, where it has been necessary to give examples and visuals, the *e*-MERLIN interferometer has been used as an example, together with the visuals obtained from the data set explored in this work. The data set is a 2016 L-Band (1–2 GHz) observation of M82 and will be described in detail in section 2.4.1.

2.1 The two-element interferometer

To understand how interferometers work, it is useful to start with the simplest case: the two-element interferometer. Consider two antennas separated by a vector $\vec{b}$ receiving a radio signal from an astronomical source located at an angle θ relative to

[1]For beginners interested in studying the principles of radio interferometry, including the derivation of results, Marr, Snell, and Kurtz, 2015 is a suitable introductory text that avoids complex mathematics. More advanced readers seeking an in-depth discussion of aperture synthesis can refer to Thompson, Moran, and Swenson, 2017.

© University of Pretoria

UNIVERSITEIT VAN PRETORIA
UNIVERSITY OF PRETORIA
YUNIBESITHI YA PRETORIA

the zenith. The zenith is the position directly above the vector $\vec{b}$ and is measured from the centre of the vector. This situation is shown in Fig. 2.1 and should be referred to for the following discussions. The vector $\vec{b}$ is called the baseline vector. It gives the direction from one antenna to the other, and its magnitude, given as,

$$\left|\left|\vec{b}\right|\right| = b, \tag{2.2}$$

is the distance between the antennas. Because the astronomical source emitting the radio signal is far away (a distance referred to as far-field), the radio signal, which is radiation travelling as a wavefront, can be approximated as planar when it arrives at the antennas. This means that parts of the same wavefront enter both antennas. Antenna 2 will receive the signal first compared to antenna 1. That is because the other part of the same wavefront in the direction of antenna 1 has to travel the extra path length defined by the dot product, $\vec{b} \cdot \hat{n}$, before reaching the antenna. The time it takes to travel the extra path length is called the geometric delay and is given by,

$$\tau_g = \frac{\vec{b} \cdot \hat{n}}{c}, \tag{2.3}$$

where $\vec{b}$, as stated before, is the baseline vector separating the antennas, $\hat{n}$ is a unit vector denoting the direction of the source relative to the centre of the baseline, and c is the speed of light. Not shown in Fig. 2.1 is a correlator. This instrument connects the two antennas to bring the signals together to be processed. Because of the geometric delay, the signals experience a phase shift when they meet at the correlator. To correct for the phase shift due to geometric delay, an instrumental delay is introduced in which the signal entering antenna two is delayed by a time equal to τ_g so that they arrive at the correlator in phase. This is a process called delay tracking. The geometric delay also changes because the Earth's rotation causes the apparent position of the source relative to the baseline vector to change. So, the instrumental delay must be constantly corrected throughout the observation at regular intervals to stay equal to the changing geometric delay. After delay tracking, the signals are multiplied at the correlator and averaged over the integration time. This is a process called cross-correlation. The integration time must be greater than the period of the wavefront carrying the signals and less than or equal to a duration of time known as the coherence time. To convey the idea of coherence time, consider this: long geometric delays cause the interference of the signals at the correlator to be destructive and sometimes result in not detecting any signal at all. So, the longest geometric delay at which a signal can be detected is the coherence time. This means that signals can be detected at times that are less or equal to the coherence time. Hence, the integration time must be less or equal to the coherence time but greater than the wavefront's period carrying the signals. The coherence time depends on the observing bandwidth (which is L-Band in this work) according to the following relation;

$$t_{\text{coherence}} = \frac{1}{\Delta\nu}. \tag{2.4}$$

The coherence time becomes important when observing an astronomical source with an extended structure, as in this work. The sources within M82 are located at different positions. So, if a reference point in M82 is chosen to calculate delays relative to this reference point, the delays for these sources within M82 will differ. Still, the sources will be detected if they are within the coherence time and are bright enough.

Another essential point is that a phase shift arises from geometric delay and other

© University of Pretoria

UNIVERSITEIT VAN PRETORIA
UNIVERSITY OF PRETORIA
YUNIBESITHI YA PRETORIA

FIGURE 2.2: The locations of the *e*-MERLIN antennas (image taken from Garrington and Beswick, 2016). Clockwise from top: Jodrell Bank Lovell, Jodrell Bank Mk2, Cambridge, Defford, Knockin, Darnhall and Pickmere.

instrumental and non-instrumental factors. The overall response to these factors is an oscillating pattern (much like a sine wave) known as a fringe pattern. So, delay tracking corrects for the geometric delay, and calibration (discussed in section 2.3) corrects for other errors that would distort the fringe pattern, ultimately allowing the source's intrinsic phase to be determined. Another measurement of interest after calibration is the amplitude of the signal. The phase gives the position of the source in the sky, and the amplitude provides a physically meaningful flux density of the source. The phase and amplitude are contained within the visibility function; individual measurements of this function are called visibilities, and the visibility function is the output of cross-correlation.

2.2 The e-MERLIN telescope and observational setup

The *e*-MERLIN interferometer is located in the United Kingdom and was used to obtain the 2016 L-Band data set of M82 explored in this work. With the working principles of a two-element interferometer laid down in section 2.1, this section introduces the *e*-MERLIN interferometer, and every concept defined for the remainder of this section will be defined and/or explained in connection to the *e*-MERLIN interferometer and the L-Band continuum data set. However, the concepts apply equally well to other interferometers.

The *e*-MERLIN interferometer consists of seven antennas distributed across England, as shown in Fig. 2.2. Each antenna is connected to the Jodrell Bank Observatory in Cheshire, England, forming a highly sensitive radio interferometer. The *e*-MERLIN is a successor of MERLIN (Multi-Element Radio-Linked Interferometer Network; Thomasson, 1986) and was born of the fact that the long radio-linked baselines limited the bandwidth, and hence sensitivity. To improve the sensitivity, the antennas were connected using optical fibres instead of radio, and the bandwidth

© University of Pretoria

UNIVERSITEIT VAN PRETORIA
UNIVERSITY OF PRETORIA
YUNIBESITHI YA PRETORIA

could be increased at least 100-fold, resulting in a sensitivity of 30 times better. The history and development of the *e*-MERLIN interferometer can be found in Garrington and Beswick, 2016.

With seven antennas and each pair acting as the two-element interferometer as detailed in section 2.1, this configuration yields a total of 21 unique baselines. The longest of these baselines extends 217 km, connecting the Knockin and Cambridge stations.

The wide observation bandwidth of 1-2 GHz allows for high angular resolution. Theoretically, the best resolution achievable is limited by the highest observed frequency. For this study, the L-band spans a frequency range from 1.253 GHz to 1.765 GHz (see Table 3.4). Applying Equation (2.1) to the highest frequency, $\nu_{1.765} = 1.765$ GHz, results in a theoretical best resolution of 0.161 arcsec.

Conversely, the worst theoretical resolution is determined by the lowest observed frequency. Using Equation (2.1) with the lowest frequency, $\nu_{1.253} = 1.253$ GHz, gives a theoretical worst resolution of 0.227 arcsec. The difference in resolution between the highest and lowest frequencies within our observing bandwidth (1.765 GHz and 1.253 GHz, respectively) is approximately 0.066 arcsec.

However, the fundamental theoretical resolution is subject to degradation from several factors. These include atmospheric turbulence, caused by variations in the Earth's atmospheric density, radio frequency interference (RFI) from human-made sources such as cell phones and Wi-Fi, and imperfections in the telescope's optical system. Consequently, the effective resolution achieved in this observation is slightly lower than the theoretical limit, measured to be ~ 0.162 arcsec.

The way the antennas are arranged in the array produces an effective beam pattern of the interferometer called the synthesized beam or point spread function (PSF). This beam is narrower than the beams of the individual antennas, and its size is the effective resolution of the interferometer. When observing an astronomical source, if there is some structure in the source that is larger in angular extent than the size of the PSF, that structure is said to be resolved. If some structure is smaller in angular extent than the size of the PSF, that structure is said to be unresolved and is called a point source.

There is a plane onto which the baselines are projected, called the *uv*-plane. It can be seen in Fig. 2.1 that as the Earth rotates and the source changes position, the projected baseline is shorter than the geometric baseline. The projected baseline only equals the geometric baseline when the source is directly above the geometric baseline connecting the two antennas. This is a position known as transit. When the baseline is projected onto the *uv*-plane, it follows a track as the Earth rotates. This track, known as the *uv*-track, covers a portion of the *uv*-plane and contains the visibilities described as the interferometer output in section 2.1. Because it covers only a part of the *uv*-plane, the baseline is said to sample the *uv*-plane, and this sample reveals the structure of the astronomical source that the baseline is sensitive to. Shorter baselines are sensitive to large angular scales (often put as short baselines sample low spatial frequencies), and long baselines are sensitive to small angular scales (often put as long baselines sample high spatial frequencies). The meaning of the preceding line is that the shortest baseline in the array determines the largest angular structure of the astronomical source that one can detect.

Suppose the astronomical source has some structure larger in angular extent that requires a shorter baseline than those present in the array to be detected. In that case, it will not be detected even if it is physically present in the field. However, suppose the shortest baseline is short enough to detect the larger angular structure of the astronomical source. In that case, the longer baselines will resolve the finer

© University of Pretoria

UNIVERSITEIT VAN PRETORIA
UNIVERSITY OF PRETORIA
YUNIBESITHI YA PRETORIA

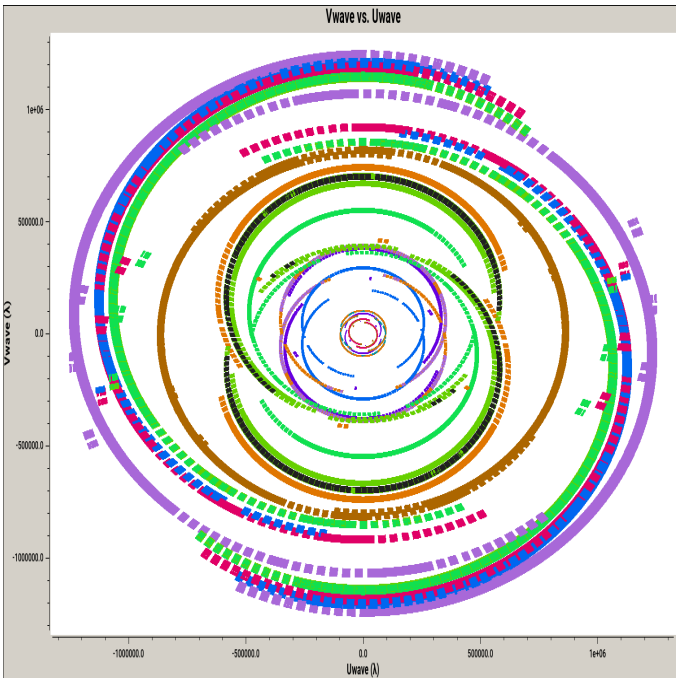

FIGURE 2.3: *uv*-plane coverage of M82 observation at 1.5 GHz obtained from the *e*-MERLIN interferometer. *uv*-tracks are colored by baseline.

details of this structure, and the details that cannot be resolved will appear as point sources if detected. For this reason, interferometers are spatial filters, allowing the freedom to arrange antennas to form baselines that will reveal the structure of the astronomical source that one is interested in while filtering out the rest of the details of the astronomical source. It makes sense then to use an array of more than two antennas and arrange them to form different baseline sizes to sample the *uv*-plane to reveal different structural scales of the astronomical source of interest, the combination of which reveals the model of the overall structure of the source. Fig. 2.3 shows the *uv*-plane coverage of the 2016 L-Band observation of M82 at 1.5 GHz explored in this work, obtained with the *e*-MERLIN interferometer. The image of the source, in this case M82, is the transformation of the *uv*-plane coordinates into an image plane. This transformation will be clarified in the next paragraphs. Ideally, the *uv*-plane should be filled to give the exact image of M82, but because it is sampled, it gives a model of the sky brightness distribution of M82.

To summarise the idea of the *uv*-plane, it is the coverage of the *uv*-plane (in this case Fig. 2.3) that determines the accuracy of the model of the targeted astronomical source (in this case M82). The more the *uv*-plane is sampled, the more the model will resemble the astronomical source. A couple of techniques are used to sample more spatial frequencies in the *uv*-plane as possible, including Earth rotation synthesis (Fomalont, 1973) and multi-frequency synthesis (MFS; Bajkova, 2008). For this observation, the Earth rotation synthesis was employed, and the orientation and projected length of the 21 baselines changed relative to the sky during the day. Each baseline follows a unique track which samples unique spatial frequencies (and hence different angular scales in the image plane), and the *uv*-coverage shown in Fig. 2.3 is a contribution from all 21 baselines, with each baseline acting as the two-element interferometer described in section 2.1.

There is a mathematical relationship between the *uv*-plane and the image plane

© University of Pretoria

UNIVERSITEIT VAN PRETORIA
UNIVERSITY OF PRETORIA
YUNIBESITHI YA PRETORIA

in which the visibilities are transformed from the uv-plane to the image plane to make the model image of the astronomical source. This relationship is called a Fourier Transform (FT; James, 2011) and is given by,

$$I(x,y) = \iint_{uv} V(u,v) e^{-2\pi i(ux+vy)} \, \mathrm{d}u \, \mathrm{d}v, \tag{2.5}$$

where x, y are the angles representing a pixel in the image plane, and u, v are the coordinates of the visibility data points in the uv-plane as in Fig. 2.3. Equation (2.5), taken from Marr, Snell, and Kurtz, 2015, is the van-Cittert-Zernike theorem. The critical point is that the baselines measure visibilities, $V(u,v)$, and a two-dimensional FT is applied to the visibilities to make a model image, $I(x,y)$, of the astronomical source. This transformation from the uv-plane to the image plane allows astronomers to construct a model of the sky brightness distribution. The FT ensures that the spatial frequency data collected by the interferometer baselines are translated into a detailed image of the astronomical source.

2.3 Calibration

After observation and correlation of the data, the signals coming from the various antennas may still be out of phase, resulting in measured visibilities diverging from their true value. Sometimes, no signal is detected at all. Some common reasons why the visibilities come out corrupted include atmospheric effects, where a signal could be attenuated from clouds passing above one antenna but not another, or radio seeing in which water vapour causes phase shifts in the data recorded by one antenna. One antenna might have a defective electronics module that causes large phase drifts or delay jumps that affect data on all baselines to this antenna but not on other baselines. Calibration is correcting for these corrupting effects, and the calibration steps include:

- **Data flagging**: Identifying and removing bad data points, such as Radio Frequency Interference (RFI), off-source data and instrumental faults.
- **Phase calibration**: Correcting for visibility phase by aligning the signals for constructive interference.
- **Amplitude calibration**: Visibility amplitude needs to be constant as all algorithms assume that the sky brightness distribution is constant in flux and position.
- **Bandpass calibration**: Correcting for variations in the instrument's response across the frequency band.
- **Gain calibration**: Determining and applying gain factors to ensure consistent amplitude measurements.
- **Flux scaling**: Determining the absolute flux density of the observed sources by comparing them to known flux calibrators. Section 2.4.1 gives the flux calibrators used in this work.

© University of Pretoria

UNIVERSITEIT VAN PRETORIA
UNIVERSITY OF PRETORIA
YUNIBESITHI YA PRETORIA

2.4 Data reduction, imaging and self-calibration

2.4.1 The *e*-MERLIN data

This study uses continuum data from a 2016 L-Band (1–2 GHz) observation of the starburst galaxy M82, obtained with the *e*-MERLIN interferometer. The observations were conducted at a central frequency of 1.5 GHz on two separate occasions, utilizing both left-left (LL) and right-right (RR) polarizations. The total bandwidth of 512 MHz was divided into 512 channels, each 0.12 MHz wide. The first epoch took place from 25 to 27 January 2016, lasting 40 hours, 9 minutes, and 45 seconds, while the second occurred from 27 to 28 January 2016, lasting 21 hours, 28 minutes, and 35 seconds. The two sessions were separated by 15 hours, 58 minutes, and 0.75 seconds. A phase reference source, 0959+695, was used to calibrate telescope phases, and data were weighted based on the relative sensitivity of each *e*-MERLIN antenna.

Once phase corrections were applied, the 2016 dataset was processed directly in the J2000 coordinate system using the calibration steps outlined earlier. An updated position for the phase calibrator, 0959+695, was obtained from VLBI observations. The final step involved imaging the target source, 0955+696 (M82).

The data was first processed using the *e*-MERLIN CASA pipeline (Moldon, 2021) for initial calibration. The Common Astronomy Software Applications (CASA; CASA Team et al., 2022) was then used to inspect the data and flag any bad points. Afterward, the dataset was sent back through the *e*-MERLIN CASA pipeline for automated calibration. Once fully calibrated, an image of the source 0955+696 (M82) was produced by converting the visibilities from the *uv*-plane to the image plane.

2.4.2 The dirty image and deconvolution of the image

When imaging, the first step is to define a *uv*-grid of regularly spaced cells. Since the *uv*-plane (Fig. 2.3) is not filled, some of the cells will not have data points in them. The Fourier Transform (FT) skips the cells without data points and effectively interpolates over these pixels, leading to an imaging error. In Section 2.2, it was established that the arrangement of antennas results in a beam pattern on the sky determined by the combination of all the different baselines that go into making the image. This beam pattern is referred to as the synthesized beam or PSF. The image reconstructed from the FT, $I(x, y)$, is a convolution of the actual image of the source (usually referred to as the true sky brightness distribution) and the PSF. This convolution is called a dirty image. The top image of Fig. 2.4 shows the PSF of the *e*-MERLIN interferometer at 1.5 GHz. The additional structures extending from the center, known as sidelobes, are an inherent feature of the PSF. These sidelobes arise from the incomplete *uv*-coverage and the resulting sampling pattern of the interferometer. Ideally, one would like a symmetric two-dimensional elliptical Gaussian pattern with no additional structure.

The PSF can be thought of as how a point source would appear in the dirty image. The bottom image of Fig. 2.4 shows the dirty image of 0955+696 (M82), the convolution of the sky brightness distribution of the source and the PSF. Sometimes, the sidelobe levels are weak, and the dirty image can be used directly to extract some science. More often, as in this case, the sidelobes are so strong that they distort the sky brightness distribution. In this case, deconvolution is required to remove the PSF. Various methods are employed to deconvolve the PSF. The most common and employed in this work is the CLEAN algorithm developed by Högbom, 1974. The basic idea of the CLEAN algorithm is, by an iterative process, to slowly subtract the

© University of Pretoria

UNIVERSITEIT VAN PRETORIA
UNIVERSITY OF PRETORIA
YUNIBESITHI YA PRETORIA

PSF pattern associated with each small piece of flux density until nothing is left but noise. The pieces of subtracted flux density are then added back into the image, but after convolving them with a new beam that reflects the resolution of the PSF from the observation and is free from sidelobes. The steps involved in their order are:

1. The brightest pixel in the dirty image is determined, and some fraction of the flux density in the pixel is inferred to be a real emission. The fraction used is called a gain. The gain and its position are then stored by the CLEAN algorithm and then recorded into a model image.

2. The clean component from step 1 is convolved with the PSF from the observation, and this convolution centred on the location of the clean component is subtracted from the dirty image, yielding a residual image. The program returns to step 1 and searches for the brightest pixel in the residual image.

3. Steps 1 and 2 are repeated until the residual image does not show any brighter pixel than its noise.

4. The algorithm then calculates a clean beam, a two-dimensional elliptical Gaussian with no sidelobes. This is calculated by fitting a two-dimensional Gaussian to the central lobe of the PSF from the observation. The clean beam aims to replicate the idealized resolution of the interferometer, free of sidelobes and other artefacts.

5. All clean components are then convolved with the clean beam and added to the residual image to produce a clean image, ensuring that the final reconstructed image reflects the intrinsic resolution of the interferometer while minimizing the impact of sidelobes.

For the observation in this work, the package used to implement the CLEAN algorithm was WSCLEAN (Offringa, McKinley, Hurley-Walker, et al., 2014; Offringa and Smirnov, 2017). The parameters used were:

- `gain` - The gain is set to 10% by default. This determines the percentage brightness removed from the highest brightness pixel for each CLEAN iteration.

- `scale` - The scale parameter sets the angular size for each pixel. This is estimated by determining the effective resolution of the interferometer. The longest UV distance for this observation is $1.2756\times10^6\lambda$ ($\lambda = 20$cm is the observing wavelength), giving an effective resolution of ~ 0.162 arcsec and cell size of 32.340 milliarcseconds (mas). The cell size is smaller than the effective resolution to ensure proper sampling of the data. According to the Nyquist sampling criterion, the pixel size is typically chosen to be 3—5 times smaller than the resolution to avoid undersampling and accurately represent the synthesized beam. This smaller cell size helps to preserve source shapes, improves the accuracy of deconvolution algorithms, and allows for more flexibility in post-processing, ensuring the image is well-sampled and high-fidelity.

- `weight` - Briggs weighting (Briggs, 1995) was used. This weighting is a balance between *natural weighting* and *uniform weighting*. Natural weighting accounts for the uneven sampling of the *uv*-plane, where some cells contain multiple visibilities while others have none. By giving more weight to cells with higher visibility density, natural weighting increases the sensitivity of the final image,

© University of Pretoria

UNIVERSITEIT VAN PRETORIA
UNIVERSITY OF PRETORIA
YUNIBESITHI YA PRETORIA

producing a high signal-to-noise ratio (S/N). This makes it particularly effective for detecting low flux density sources. However, because interferometric arrays typically have more short projected baselines than long baselines, natural weighting is biased toward short baselines, resulting in reduced resolution in the final image.

Uniform weighting addresses the resolution limitation of natural weighting by assigning equal weight to all cells, regardless of visibility density. This approach enhances resolution and simplifies the PSF but often results in a lower S/N due to reduced sensitivity.

Briggs weighting is a balance between sensitivity and resolution and can be controlled by a parameter called `robust`, which takes floating point numbers between -2 and 2. Values towards -2 prioritise resolution (uniform weighting), and values towards two prioritise sensitivity (natural weighting). For this observation, `robust 0.5` was used to detect as many sources as possible and to have a final image with good resolution.

- `auto-threshold` - This parameter sets a stopping criterion for steps 1 and 2 in the CLEAN algorithm by defining a threshold relative to the residual noise level. Steps 1 and 2 together are called the minor cycle. The major cycle involves transforming the clean components (or clean image) into model visibilities, subtracting the model visibilities from the original observed visibilities, and using the difference to recalculate the dirty image (residual image). WSCLEAN calculates the standard deviation of the residual image before the start of every major cycle and continues cleaning until no pixel in the residual image exceeds the given `auto-threshold` factor times the standard deviation of the image. The standard deviation is estimated using the median absolute deviation (MAD), which is a robust estimator that minimizes the influence of residual source structure. The first image `auto-threshold` was set to 5.

- `auto-mask` - This parameter sets a threshold for automatically generating a mask during deconvolution. The auto-mask parameter defines a signal-to-noise ratio (SNR) below which pixels are excluded from being considered real emission. It acts as a stopping criterion by masking out regions with values lower than this SNR threshold, ensuring that only significant structures are included in the cleaning process. This helps avoid including noise or artefacts as part of the clean components. This parameter has also been varied throughout the imaging process, but it was set to 20 for the first image.

- `niter` - In addition to `auto-threshold`, the `niter` parameter sets the number of iterations for the minor cycle. This parameter has been varied throughout the imaging process, but it was set to 10,000 iterations for the first image.

- `mgain` - This parameter sets the major iteration gain. During every major iteration, the gain is reduced by the given factor. For this observation, `mgain` is set to 0.8.

Table 2.1 summarizes the parameters used in WSCLEAN to make the first clean image of 0955+696 (M82); the resulting image is the middle image of Fig. 2.4.

2.4.3 Self-Calibration

Amplitude calibration can be imperfect due to weather, pointing errors, inaccurately measured gains, and system variations. Phase errors arise from the troposphere,

© University of Pretoria

UNIVERSITEIT VAN PRETORIA
UNIVERSITY OF PRETORIA
YUNIBESITHI YA PRETORIA

TABLE 2.1: Parameters used in WSCLEAN to deconvolve the PSF (top image of Fig. 2.4) from the dirty image (bottom image of Fig. 2.4) to produce a clean image (middle image of Fig. 2.4) of 0955+696 (M82).

Parameter	Value
`gain`	10%
`scale`	32.340 masec
`weight`	`briggs` 0.5
`auto-threshold`	5
`auto-mask`	20
`niter`	10 000

ionosphere, imperfect clocks/frequency standards, and imprecise knowledge of array geometry and phase shifts in the electronics. The worst of these effects can be removed through a process known as self-calibration. When working with VLBI data, the phase errors are especially severe that without self-calibration, the phases are essentially random, and often, no meaningful image can be made.

To improve the image, we employ the hybrid CLEAN method (Readhead and Wilkinson, 1978). The core idea of hybrid CLEAN is to solve simultaneously for both the source image and the antenna calibration parameters. This is done by alternately generating a deconvolved (clean) image using assumed calibration parameters and then refining those parameters based on the clean image. To begin, an initial clean image (as shown in the middle image of Fig. 2.4) serves as the model. A FT is applied to this model to transform it into the *uv*-plane, generating model visibilities. These model visibilities are then compared with the measured visibilities.

It is known that measured visibilities contain phase errors, but since the model phases are more accurate (because the CLEAN algorithm tends to push the data towards a reasonable image), self-calibration allows the measured visibility phases to vary to better match the model. This iterative process improves the data set if the fit between the model and the measured data improves. For each time interval in the observation, all phases are allowed to vary, ensuring the best possible fit to the model. The improved data set is then used to create a new clean image, which serves as the model for the next round of self-calibration. This process repeats until no further improvements are observed in the fit between the model and the data.

The middle image of Fig. 2.4 is the first clean image of the target 0955+696 (M82) used in this work, which served as the model for the initial round of self-calibration. The CASA (CASA Team et al., 2022) package was used to generate and apply calibration tables for the improved data resulting from self-calibration. Table 2.2 summarizes the self-calibration process and the columns are described in caption. Column (1) list calibration tables generated from self-calibration. The 'p' next to the numerical value indicates phase correction, and the numerical value denotes the cycle number. The table includes seven cycles of self-calibration. The improvement is evident in the increase in peak flux denisity of the image (column 2), decrease in background noise (RMS; column 3) and increase in S/N (column 4). This indicates that the flux is being resolved, meaning the self-calibration process helps locate the flux contribution within the source. The last four columns of the table show variable parameters: column (5), column (6), and column (7), which are discussed in section 2.4.2, while column (8) represents the solution interval for the observation. The final

© University of Pretoria

UNIVERSITEIT VAN PRETORIA
UNIVERSITY OF PRETORIA
YUNIBESITHI YA PRETORIA

TABLE 2.2: This table shows self-calibration parameters used in the processing of 0955+696 (M82) to obtain the clean image shown in Fig. 3.1. Column (1) displays the calibration tables generated across seven self-calibration cycles, where 'p' signifies phase correction and the numerical value represents the cycle number. The increase in peak flux density (column 2), decrease in background RMS noise (column 3), and enhanced S/N (column 4) illustrate the effectiveness of self-calibration in resolving source flux. Columns (5), (6), and (7) contain variable parameters, as detailed in section 2.4.2, while column (8) indicates the solution interval for the observation. Section 2.4.3 provides detailed column descriptions.

Caltable	Peak (Jy beam^{-1})	RMS (Jy)	S/N	`auto-threshold`	`auto-mask`	`niter`	`solint`
(1)	(2)	(3)	(4)	(5)	(6)	(7)	(8)
0	51.511e-03	7.979e-05	645	5	20	10000	-
p1	58.925e-03	7.096e-05	830	4	17	15000	inf
p2	60.718e-03	6.352e-05	955	3	14	30000	210s
p3	61.111e-03	6.139e-05	995	2.5	10	40000	140s
p4	61.240e-03	6.087e-05	1006	2	8	45000	105s
p5	61.260e-03	6.025e-05	1016	1.5	7	60000	84s
p6	61.241e-03	5.968e-05	1026	1.0	6	70000	70s
p7	61.261e-03	5.935e-05	1032	0.9	5	90000	60s

image the target 0955+696 (M82) produced from table is displayed in Fig 3.1 in the next chapter (chapter 3) where we report the results of the observation.

© University of Pretoria

UNIVERSITEIT VAN PRETORIA
UNIVERSITY OF PRETORIA
YUNIBESITHI YA PRETORIA

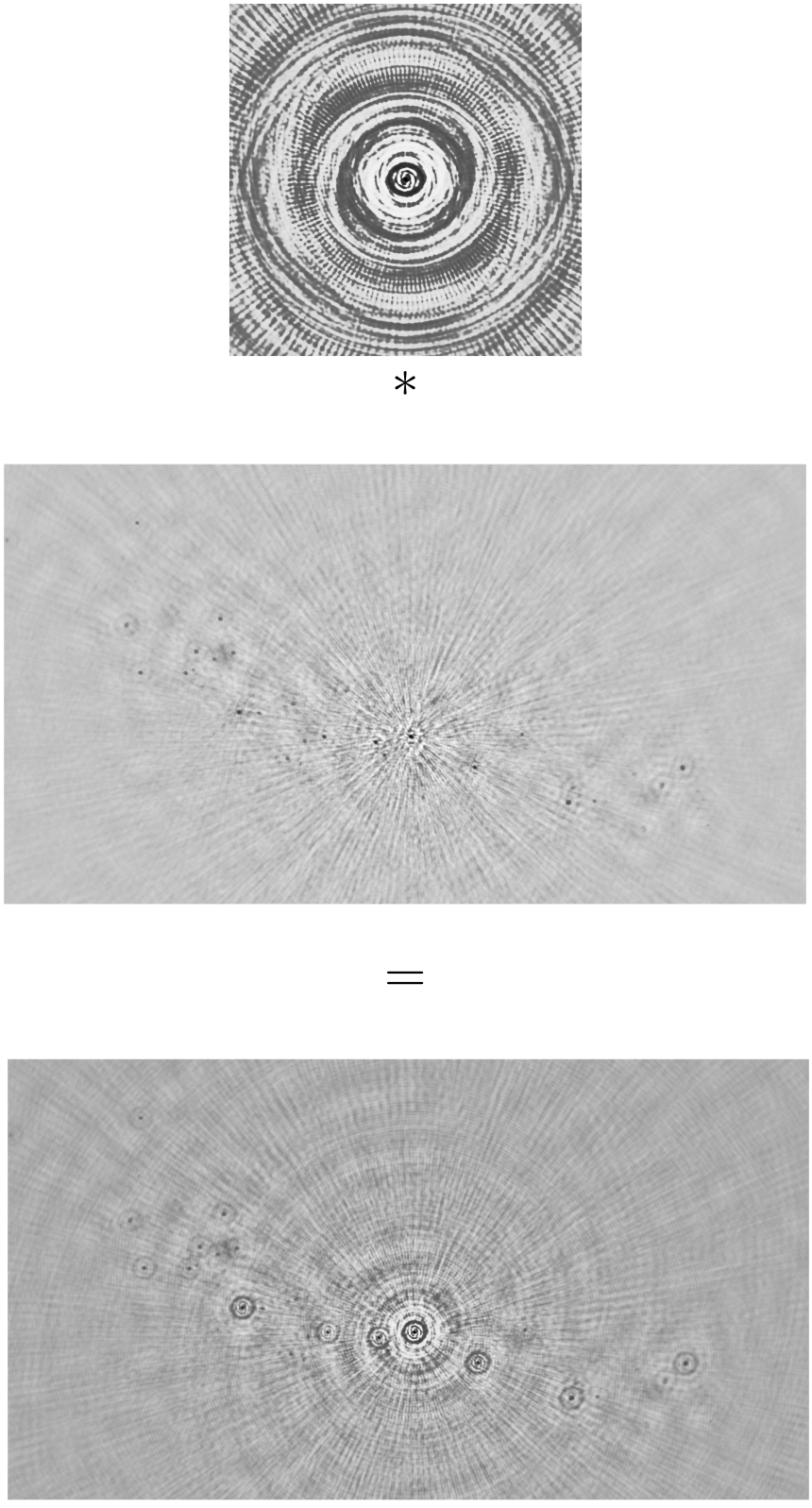

FIGURE 2.4: Convolution of the PSF distribution (top) with the sky brightness distribution (middle) results in the "dirty" image (bottom). This example is obtained from the 2016 L-Band data set observed at 1.5 GHz by the *e*-MERLIN telescope.

© University of Pretoria

Chapter 3

Results

This chapter begins with a summary of the data reduction steps described in section 2.4. The data is a 2016 L-Band data set observed at 1.5 GHz with the e-MERLIN interferometer on two occasions. The data calibration and reduction were done with CASA (CASA Team et al., 2022). The flux was calibrated by observing the primary flux calibrator 1331+305. Self-calibrations for both phases and amplitudes were used to improve the dynamic range. Briggs weighting (Briggs, 1995) was applied to the imaging process, yielding a clean beam size of 0.17 arcsec $\times$ 0.13 arcsec. Fig. 3.1 shows the 61.261 mJy beam^{-1} *e*-MERLIN image of M82 obtained from the observation.

The image reveals numerous distinguishable, discrete, and compact sources, most of which appear round, although a few are elongated. Superimposed on this is a background of scattered diffuse emission. The *e*-MERLIN interferometer baselines, while sufficient for detecting the emission, lacked the longer separations needed to resolve the detailed structure of this more diffuse component. However, since the main interest here is the compact radio sources in the central region of M82, the extended diffuse emission is not of primary concern.

Past extensive observations of M82 have detected over 50 compact radio sources, with many of them identified as young SNe and SNRs resulting from the deaths of massive stars in the galaxy's starburst region (Kronberg, Biermann, and Schwab, 1985; Kronberg and Sramek, 1985; Kronberg, 1988; Fenech et al., 2008). The same approach was followed in this study; SNe and SNR candidates were selected from the central region of M82 from the clean image shown in Fig. 3.1, following the criteria outlined below:

1. The signal-to-noise (S/N) ratio must be at least 6. The RMS noise of Fig. 3.1 as given in Table (2.2) is 59.36 μJy beam^{-1}. This gives a minimum detectable signal of 356.16 μJy beam^{-1}. This step was implemented using Python blob detection and source finder (PyBDSF; Mohan and Rafferty, 2015). High S/N is a requirement for accurate source identification, particularly in the presence of a bright source like SN 2008iz (SN 2008iz is discussed in section 4.1.1). Its high flux introduces calibration residuals and deconvolution artefacts, increasing the local RMS noise and raising the detection threshold in its vicinity. This can obscure faint sources or cause misidentifications in PyBDSF due to altered noise estimates. However, maintaining a high S/N helps mitigate these effects by ensuring that real sources stand out more clearly against noise and reducing the risk of spurious detections. A robust S/N threshold improves the reliability of detections even in regions affected by dynamic range limitations and residual imaging artefacts.

© University of Pretoria

UNIVERSITEIT VAN PRETORIA
UNIVERSITY OF PRETORIA
YUNIBESITHI YA PRETORIA

2. The source should not be contaminated by the diffuse emission. This is easily satisfied as described in paragraph 2 above that the baselines of the e-MERLIN interferometer are not short enough to detect the more diffuse emission.

3. Morphologically, a source must appear compact. This is a natural requirement for a young SN or SNR, although it is sometimes acceptable that they are elongated in their shape.

Using the criteria described above, a total of 36 sources were identified in the central region of M82. This region is approximately rectangular, spanning 0.05298 degrees in Right Ascension and 0.00839 degrees in Declination, corresponding to roughly 3.18 arcminutes in Right Ascension and 0.50 arcminutes in Declination. To determine the flux densities of these sources, two independent methods were employed: Gaussian fitting using the CASA task `imfit` and the source finding algorithm PyBDSF. Table (3.1) presents the results obtained from the CASA analysis, and the columns (1)–(7) are detailed below.

- Column (1) assigns a sequential number to each source.
- Column (2) provides a corresponding name following the notation in Fenech et al. (2008).
- Columns (3) and (4) list the sources' positions. The Right Ascension and declination measurements are given as offset from $09^{h}55^{m}00^{s}$ and $69^{\circ}40'00''$ (J2000). The positions were found using the image shown in Fig. 3.1.
- Columns (5) and (6) present the peak and integrated 1.5 GHz flux densities of the sources, respectively. These values were derived using the CASA task `imfit`. For each source, an elliptical region was manually defined, and the pixel coordinates of the bottom-left and top-right corners of this region were used as input to `imfit`. Elliptical regions were chosen over square regions as the morphology of most sources was better approximated by an ellipse, thus minimizing the inclusion of surrounding background noise within the fitting area compared to potentially larger square regions. The task then performed a Gaussian fit to the emission within the defined elliptical region, yielding the reported peak and integrated flux density values.
- Column (7) lists the S/N for each source.

The letter N next to sources 1, 3, 26, and 35 represents a newly detected source which is not present in previous observations.

The flux densities obtained from PyBDSF source finding algorithm are presented in Table (3.2). The columns in this table are similar to those in Table (3.1), with the key difference being that the peak and integrated 1.5 GHz flux densities presented in Columns (5) and (6) were obtained from the PyBDSF output, where the algorithm performs an automated detection and Gaussian fitting of the sources.

Fig. 3.2 displays contour images for each of the selected sources. The source numbers correspond to Column (1) of both Table (3.1 and 3.2).

An examination of the peak and integrated flux densities presented in Table (3.1) (derived from CASA) and Table (3.2) (derived from PyBDSF) reveals generally similar flux density values for the majority of the 36 identified sources. However, a notable inconsistency is observed in both tables for a subset of sources where the peak flux density is greater than the integrated flux density. Specifically, in the CASA-derived fluxes (Table 3.1), sources 2, 12, 18, and 36 exhibit this unusual characteristic.

© University of Pretoria

UNIVERSITEIT VAN PRETORIA
UNIVERSITY OF PRETORIA
YUNIBESITHI YA PRETORIA

The PyBDSF-derived fluxes (Table 3.2) show the same trend for these sources, and additionally for source 16.

This observation, where the integrated flux density is lower than the peak flux density, is unexpected for sources that are not point-like. Given that the contour maps of 35 (excluding source 1) identified sources (as shown in Figure 3.2) exhibit multiple closed contours extending beyond the synthesized beam, it suggests that these sources are indeed resolved. Typically, for resolved sources, the integrated flux, representing the total emission over the source area, should be equal to or greater than the peak flux, which measures the intensity at the brightest point. This discrepancy could arise from several factors, including: limitations in accurately defining the source boundaries during the fitting process, particularly if the sources have extended low-surface-brightness emission that is not fully captured by the elliptical Gaussian model; potential deconvolution artifacts that might affect the flux measurements; or the inherent challenges of interferometric observations in fully recovering the total flux of extended or complex sources.

Despite these inconsistencies in a few sources, we have decided to proceed with the flux density values presented in Table (3.1), derived from the CASA `imfit` task. This decision is based on the fact that the regions for the Gaussian fitting in CASA were manually defined for each source, allowing for a more tailored approach to encompass their individual morphologies as observed in our images. We believe this manual intervention provides a more reliable representation of the sources.

For the four sources in the CASA table (2, 12, 18, and 36) where the integrated flux density is lower than the peak flux density, we will adopt a conservative approach and use the peak flux density as the representative integrated flux density for these specific sources in our subsequent analysis. This is justified by the argument that the peak flux represents the highest detected intensity and provides a lower bound on the total emission, mitigating the potential underestimation implied by the lower integrated flux values.

© University of Pretoria

UNIVERSITEIT VAN PRETORIA
UNIVERSITY OF PRETORIA
YUNIBESITHI YA PRETORIA

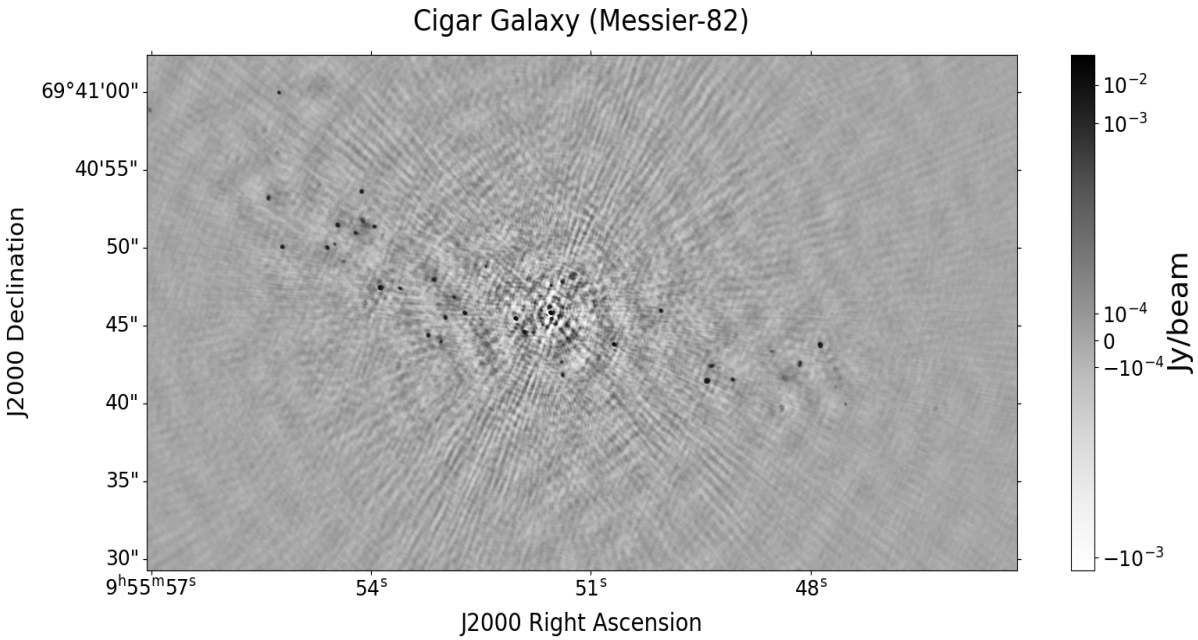

FIGURE 3.1: The 1.5 GHz e-MERLIN Clean radio map of M82 with rms noise of 59.36 μJy beam^{-1}, and a beam size of 0.17 arcsec $\times$ 0.13 arcsec. The peak flux of the map is 61.261 mJy beam^{-1}.

© University of Pretoria

UNIVERSITEIT VAN PRETORIA
UNIVERSITY OF PRETORIA
YUNIBESITHI YA PRETORIA

TABLE 3.1: Flux densities and signal-to-noise (S/N) ratios for the 36 sources selected from the central region of M82, as derived from Gaussian fitting using `imfit` in CASA. The observation was conducted with the *e*-MERLIN interferometer at 1.5 GHz. The positions of the sources are given as offset from $09^h55^m00^s$ and $69°40'00''$ (J2000).

Candidate	Name B1950	RA (09^h55^m) J2000	Dec ($+69°40'$) J2000	Peak (mJy/beam)	Int. Flux (mJy)	S/N
(1)	(2)	(3)	(4)	(5)	(6)	(7)
1.....	37.52+53.1 (N)	$46^s.314164$	$39.574498''$	0.224±0.022	0.522±0.052	3
2.....	38.76+53.5	$47^s.529197$	$39.932824''$	0.643±0.064	0.633±0.063	10
3.....	38.88+54.6 (N)	$47^s.664384$	$41.036215''$	0.407±0.041	0.479±0.048	6
4.....	39.10+57.3	$47^s.879000$	$43.719000''$	3.345±0.335	8.947±0.895	56
5.....	39.40+56.2	$48^s.151610$	$42.527620''$	1.000±0.100	3.450±0.345	16
6.....	39.64+53.3	$48^s.400100$	$39.696300''$	0.412±0.041	1.120±0.112	6
7.....	39.77+56.9	$48^s.551380$	$43.320035''$	0.569±0.057	2.396±0.240	9
8.....	40.32+55.2	$49^s.068507$	$41.533961''$	1.538±0.154	2.803±0.280	25
9.....	40.61+56.3	$49^s.370524$	$42.360193''$	1.225±0.123	8.231±0.823	20
10.....	40.68+55.1	$49^s.418200$	$41.435720''$	5.330±0.533	12.880±1.288	89
11.....	41.30+59.6	$50^s.046412$	$45.935470''$	2.840±0.284	3.980±0.398	47
12.....	41.95+57.5	$50^s.686002$	$43.766618''$	15.176±1.518	14.710±1.471	255
13.....	42.67+55.6	$51^s.387446$	$41.806625''$	1.403±0.140	3.222±0.322	23
14.....	42.67+56.3	$51^s.402028$	$42.637641''$	1.189±0.119	1.890±0.189	20
15.....	43.18+58.2	$51^s.908616$	$44.570339''$	6.150±0.615	7.749±0.775	103
16.....	43.31+59.2	$52^s.027754$	$45.425375''$	19.759±1.976	19.924±1.992	332
17.....	43.72+62.6	$52^s.435682$	$48.775565''$	1.054±0.105	1.389±0.139	17
18.....	44.01+59.6	$52^s.724810$	$45.780916''$	10.990±1.099	9.580±0.958	164
19.....	44.28+59.3	$52^s.988744$	$45.468517''$	2.010±0.201	4.160±0.416	33
20.....	44.34+57.8	$53^s.048946$	$43.937406''$	0.990±0.099	2.620±0.262	16
21.....	44.40+61.8	$53^s.147018$	$47.874267''$	1.282±0.128	5.400±0.540	21
22.....	44.51+58.2	$53^s.221011$	$44.351000''$	1.490±0.149	5.306±0.531	25
23.....	44.89+61.2	$53^s.608068$	$47.360855''$	1.586±0.159	2.258±0.226	26
24.....	45.17+61.2	$53^s.879524$	$47.407081''$	11.277±1.128	13.661±1.366	189
25.....	45.24+65.2	$53^s.960011$	$51.326502''$	1.626±0.163	3.243±0.324	27
26.....	45.38+05.5 (N)	$54^s.112720$	$51.663170''$	0.755±0.076	7.190±0.719	12
27.....	45.42+67.4	$54^s.134156$	$50.939000''$	1.972±0.197	4.586±0.459	33
28.....	45.52+64.7	$54^s.215965$	$50.914350''$	1.352±0.135	3.780±0.378	22
29.....	45.75+65.3	$54^s.458659$	$51.410569''$	1.852±0.185	5.236±0.524	31
30.....	45.79+64.0	$54^s.499553$	$50.204187''$	0.946±0.095	1.085±0.109	15
31.....	45.89+63.8	$54^s.599081$	$49.985914''$	2.434±0.243	3.559±0.356	41
32.....	46.52+63.9	$55^s.212964$	$50.023440''$	2.241±0.224	3.984±0.398	37
33.....	46.56+73.8	$55^s.260158$	$59.916315''$	1.470±0.147	2.109±0.211	24
34.....	46.70+67.1	$55^s.403080$	$53.160890''$	1.110±0.111	4.078±0.408	18
35.....	48.32+12.7 (N)	$57^s.021921$	$58.800331''$	0.568±0.057	1.184±0.118	9
36.....	SN 2008iz	$51^s.549838$	$45.790039''$	63.620±6.362	54.700±5.470	1071

© University of Pretoria

UNIVERSITEIT VAN PRETORIA
UNIVERSITY OF PRETORIA
YUNIBESITHI YA PRETORIA

TABLE 3.2: Flux densities and signal-to-noise (S/N) ratios for the 36 sources selected from the central region of M82, as derived from the PyBDSF source finding algorithm. The observation was conducted with the *e*-MERLIN interferometer at 1.5 GHz. The positions of the sources are given as offset from $09^h55^m00^s$ and $69°40'00''$ (J2000).

Candidate	Name B1950	RA (09^h55^m) J2000	Dec ($+69°40'$) J2000	Peak (mJy/beam)	Int. Flux (mJy)	S/N
(1)	(2)	(3)	(4)	(5)	(6)	(7)
1.....	37.52+53.1 (N)	$46^s.314164$	$39.574498''$	0.209±0.021	0.574±0.057	3
2.....	38.76+53.5	$47^s.529197$	$39.932824''$	0.642±0.064	0.635±0.064	10
3.....	38.88+54.6 (N)	$47^s.664384$	$41.036215''$	0.408±0.041	0.469±0.047	6
4.....	39.10+57.3	$47^s.879000$	$43.719000''$	3.439±0.344	7.809±0.781	57
5.....	39.40+56.2	$48^s.151610$	$42.527620''$	1.000±0.100	3.450±0.345	16
6.....	39.64+53.3	$48^s.400100$	$39.696300''$	0.412±0.009	1.120±0.310	6
7.....	39.77+56.9	$48^s.551380$	$43.320035''$	0.568±0.057	2.393±0.239	9
8.....	40.32+55.2	$49^s.068507$	$41.533961''$	1.504±0.150	2.871±0.287	25
9.....	40.61+56.3	$49^s.370524$	$42.360193''$	1.212±0.121	4.419±0.012	20
10.....	40.68+55.1	$49^s.418200$	$41.435720''$	5.016±0.502	12.659±1.266	84
11.....	41.30+59.6	$50^s.046412$	$45.935470''$	2.793±0.279	3.806±0.381	47
12.....	41.95+57.5	$50^s.686002$	$43.766618''$	15.333±1.533	14.309±1.431	258
13.....	42.67+55.6	$51^s.387446$	$41.806625''$	1.399±0.140	3.167±0.317	23
14.....	42.67+56.3	$51^s.402028$	$42.637641''$	1.178±0.118	1.680±0.168	19
15.....	43.18+58.2	$51^s.908616$	$44.570339''$	5.996±0.600	8.213±0.821	101
16.....	43.31+59.2	$52^s.027754$	$45.425375''$	20.064±2.006	19.130±1.913	338
17.....	43.72+62.6	$52^s.435682$	$48.775565''$	1.050±0.105	1.457±0.146	17
18.....	44.01+59.6	$52^s.724810$	$45.780916''$	9.962±0.996	9.509±0.951	168
19.....	44.28+59.3	$52^s.988744$	$45.468517''$	1.895±0.190	4.051±0.405	31
20.....	44.34+57.8	$53^s.048946$	$43.937406''$	0.992±0.099	2.174±0.217	16
21.....	44.40+61.8	$53^s.147018$	$47.874267''$	1.253±0.125	4.841±0.037	21
22.....	44.51+58.2	$53^s.221011$	$44.351000''$	1.519±0.152	4.163±0.416	25
23.....	44.89+61.2	$53^s.608068$	$47.360855''$	1.575±0.158	2.407±0.241	26
24.....	45.17+61.2	$53^s.879524$	$47.407081''$	10.030±1.003	10.699±1.070	168
25.....	45.24+65.2	$53^s.960011$	$51.326502''$	1.624±0.162	3.171±0.317	27
26.....	45.38+05.5 (N)	$54^s.112720$	$51.663170''$	0.750±0.005	6.710±0.480	12
27.....	45.42+67.4	$54^s.134156$	$50.939000''$	1.966±0.006	4.566±0.020	33
28.....	45.52+64.7	$54^s.215965$	$53.574350''$	1.953±0.195	4.016±0.402	32
29.....	45.75+65.3	$54^s.458659$	$51.410569''$	1.876±0.188	4.817±0.482	31
30.....	45.79+64.0	$54^s.499553$	$50.204187''$	0.947±0.095	1.076±0.108	15
31.....	45.89+63.8	$54^s.599081$	$49.985914''$	2.379±0.238	3.696±0.370	40
32.....	46.52+63.9	$55^s.212964$	$50.023440''$	2.246±0.225	3.935±0.394	37
33.....	46.56+73.8	$55^s.260158$	$59.916315''$	1.455±0.146	2.177±0.218	24
34.....	46.70+67.1	$55^s.403080$	$53.160890''$	1.054±0.105	3.903±0.390	17
35.....	48.32+12.7 (N)	$57^s.021921$	$58.800331''$	0.550±0.055	1.481±0.148	9
36.....	SN 2008iz	$51^s.549838$	$45.790039''$	63.182±6.318	55.233±5.523	1064

© University of Pretoria

UNIVERSITEIT VAN PRETORIA
UNIVERSITY OF PRETORIA
YUNIBESITHI YA PRETORIA

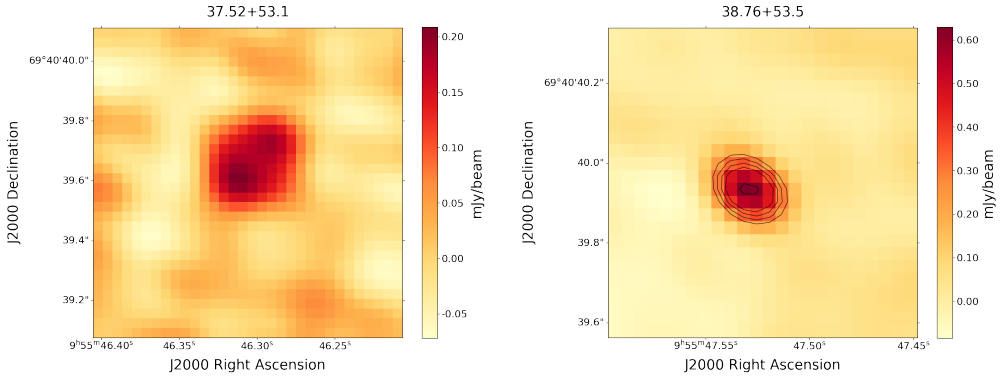

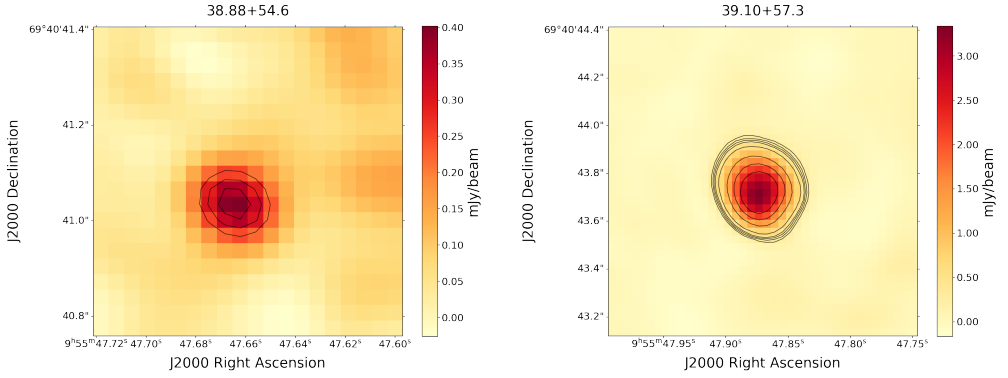

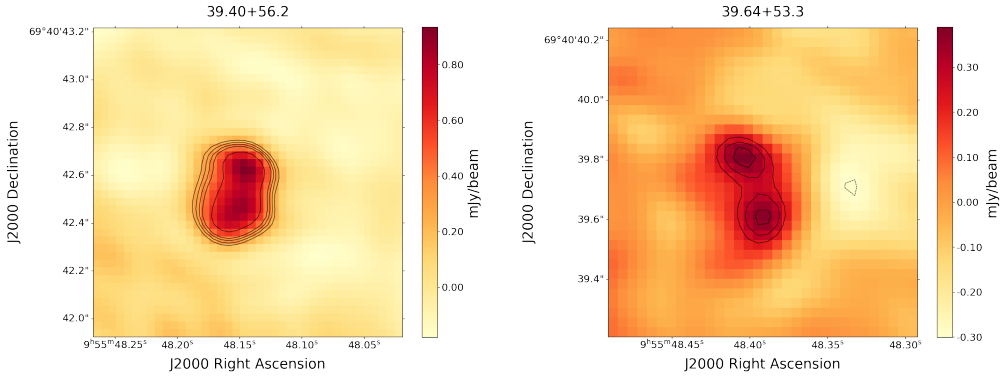

FIGURE 3.2: Contour maps of the individual sources in the central region of M82 as seen in the 2016 L-band observation at 1.5 GHz. The contours are plotted at (-5, 4, 5, 6, 7, 10, 20, 30, 40)$\times\sigma$ for all sources, where $\sigma = 59.36$ μJy is the background noise of the image (see Fig. 3.1).

© University of Pretoria

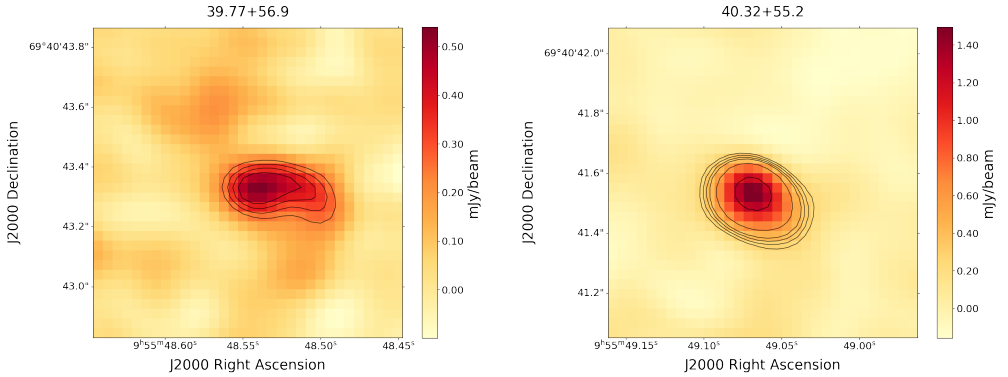

(7)

(8)

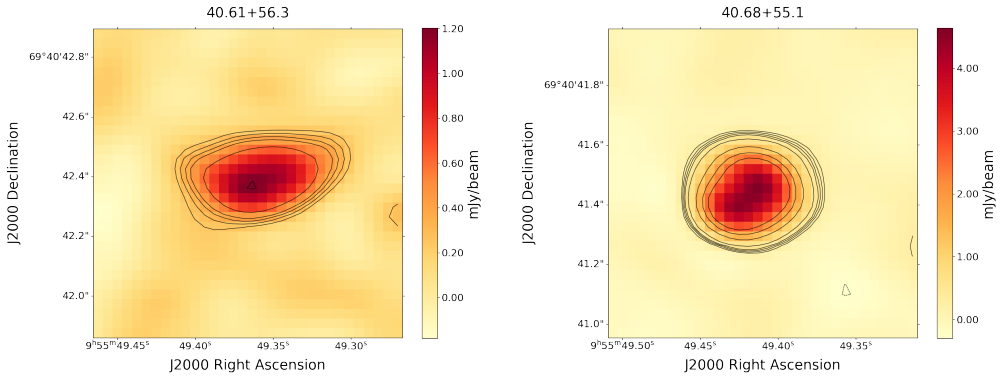

(9)

(10)

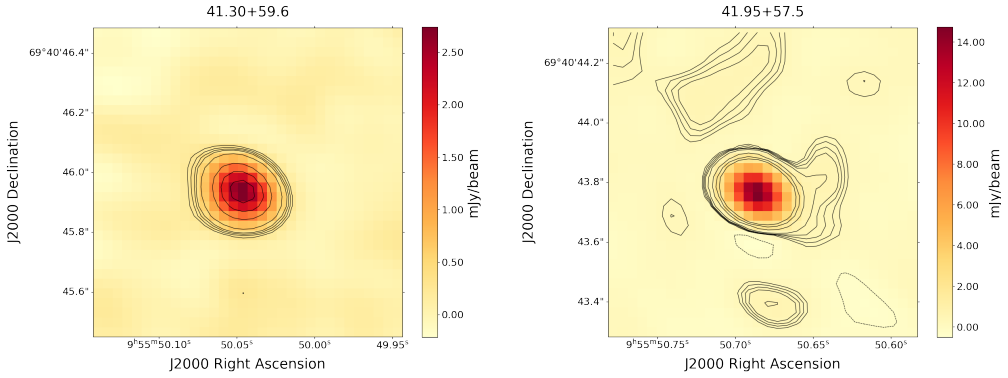

(11)

(12)

Figure 3.2 continued

© University of Pretoria

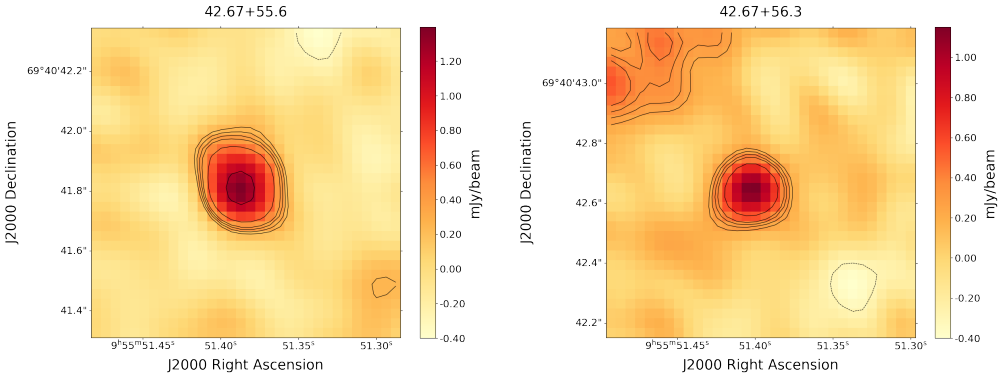

(13)

(14)

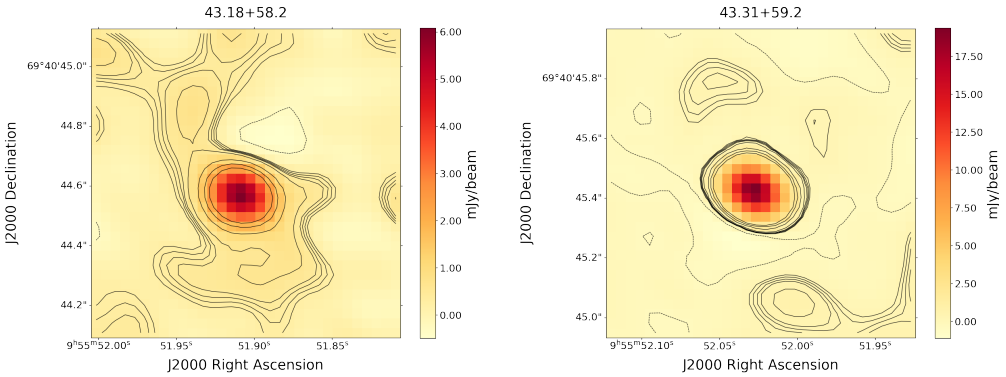

(15)

(16)

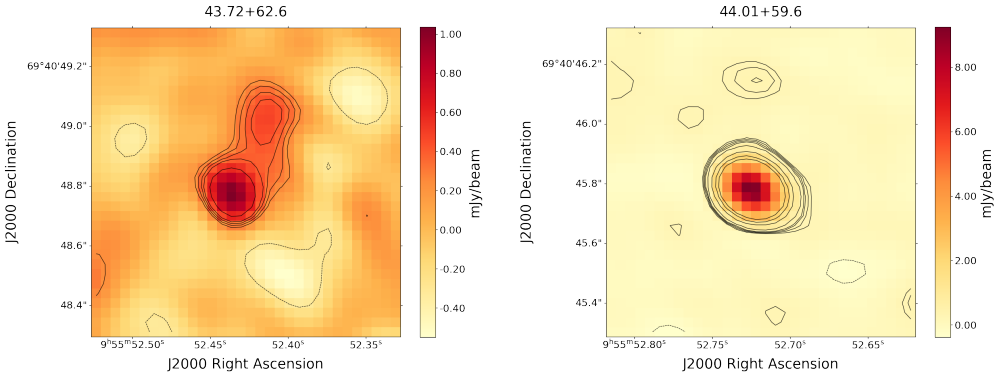

(17)

(18)

Figure 3.2 continued

© University of Pretoria

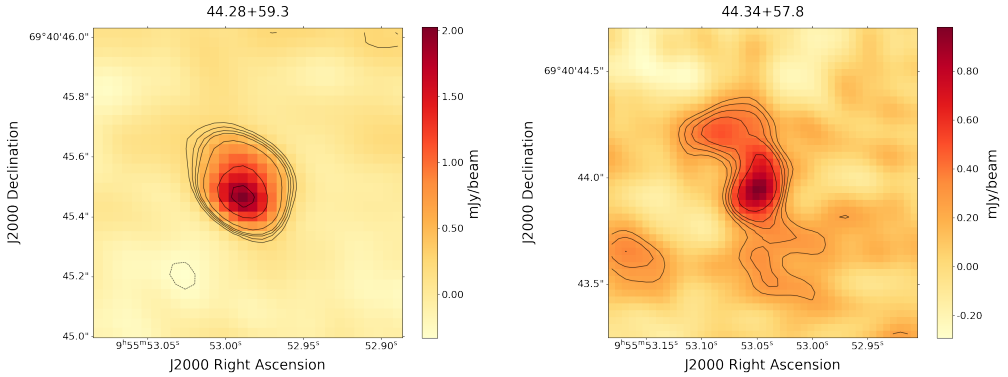

(19)

(20)

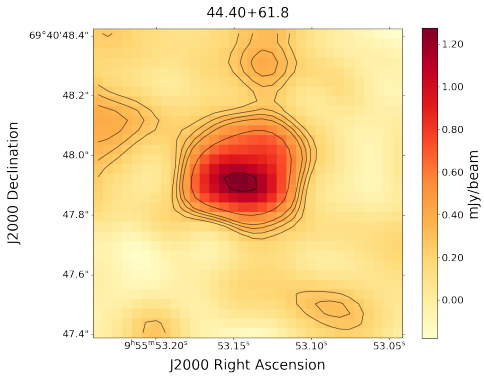

(21)

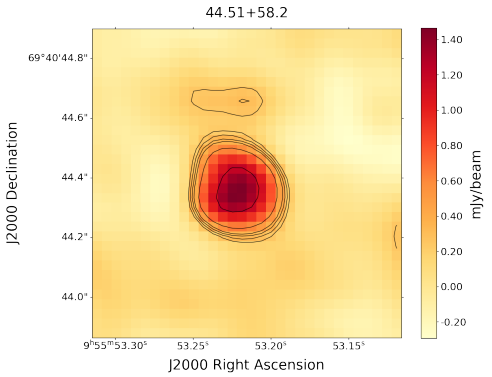

(22)

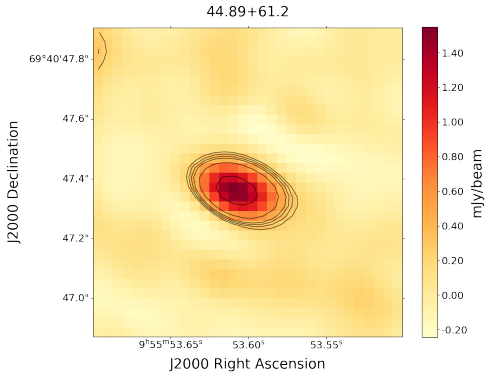

(23)

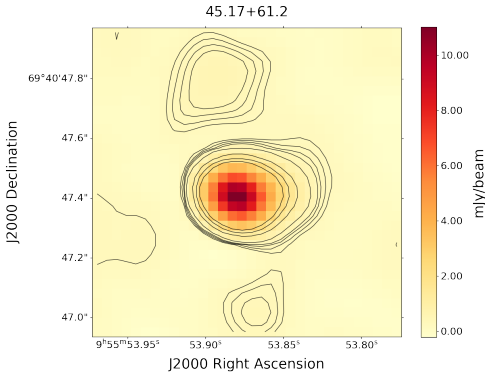

(24)

Figure 3.2 continued

© University of Pretoria

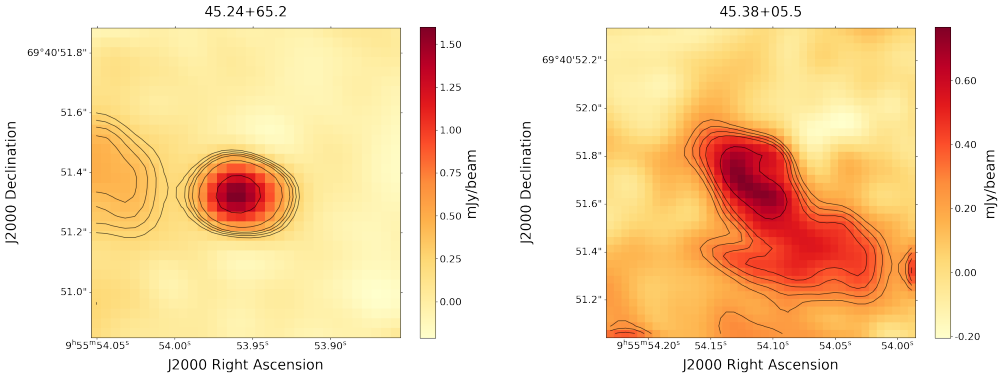

(25)

(26)

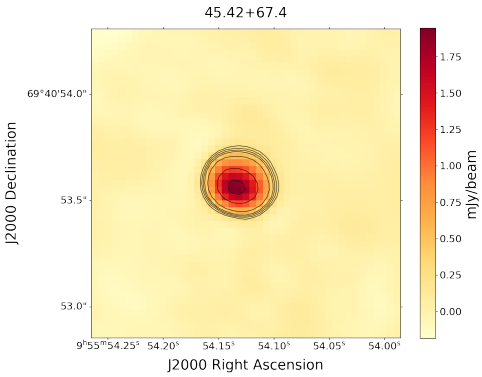

(27)

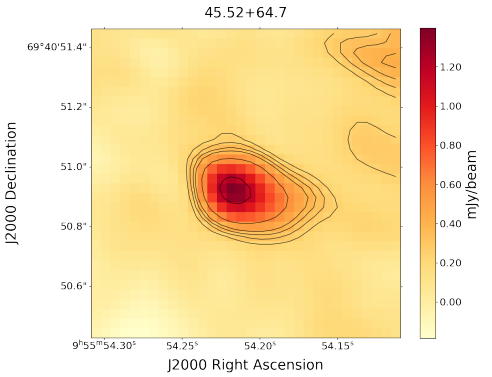

(28)

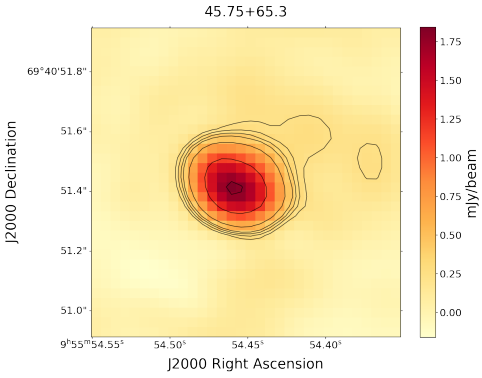

(29)

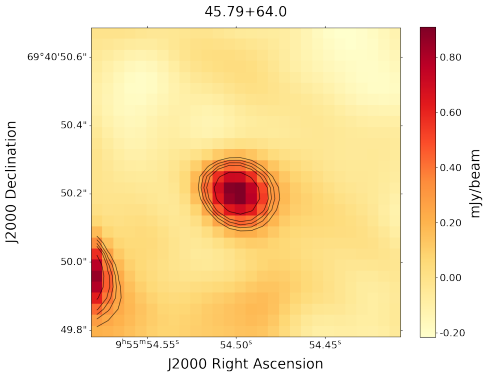

(30)

Figure 3.2 continued

© University of Pretoria

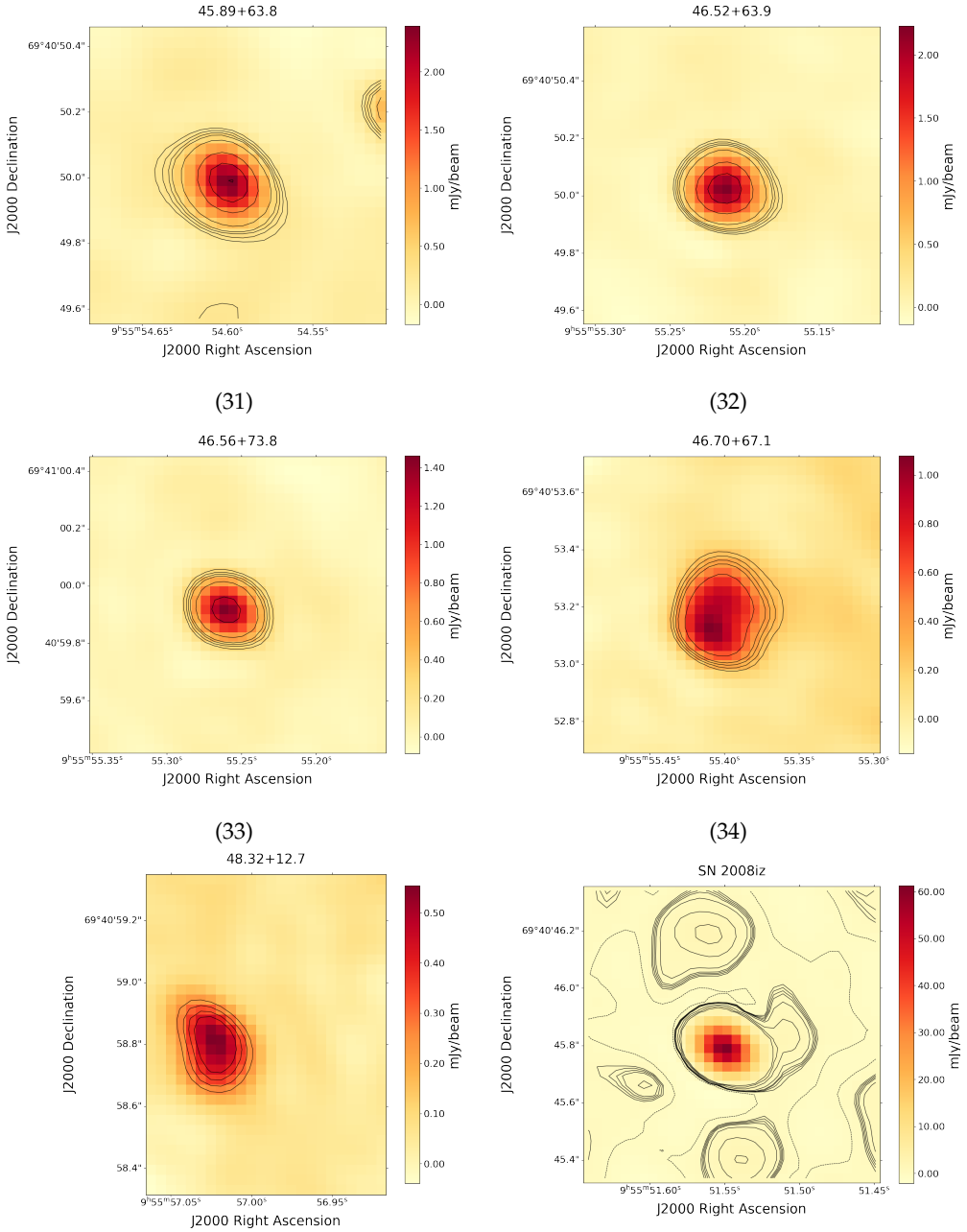

(31) (32)

(33) (34)

(35) (36)

Figure 3.2 continued

© University of Pretoria

UNIVERSITEIT VAN PRETORIA
UNIVERSITY OF PRETORIA
YUNIBESITHI YA PRETORIA

3.1 Derived Parameters

After completing the catalogue as shown in Table (3.1), the deconvolved major and minor axes angular sizes of the sources were measured using CASA. In CASA, these measurements are derived through an elliptical Gaussian fitting process, where the observed intensity distribution of each source is modelled as a two-dimensional Gaussian. As discussed in the introduction of this chapter, we have adopted the flux densities derived from CASA's `imfit` task for our analysis. While a subset of these measurements showed instances of integrated flux density being lower than peak flux density, the manual definition of elliptical regions for each source in CASA allowed for a visually controlled approach to encompass their individual morphologies. This tailored fitting process is considered crucial for obtaining reliable measurements of the sources' spatial extents and shapes. The Gaussian fitting within these manually defined regions, upon visual inspection, appeared to provide a reasonable model of the source shapes. Therefore, we utilize these CASA-derived fits not only for flux densities but also for the determination of the major and minor axes angular sizes. The observed (convolved) size, which includes contributions from both the intrinsic source size and the synthesized beam, is deconvolved using the relationship

$$\text{Observed Size}^2 \;=\; \text{Deconvolved Size}^2 + \text{Beam Size}^2. \tag{3.1}$$

The resulting deconvolved major and minor axes, expressed in arcseconds, represent the intrinsic angular dimensions of the sources.

After measuring the angular sizes of the 36 sources, their physical linear sizes were calculated using these angular measurements and the angular size distance (D_A) to M82. The physical size (l) of the source is related to its angular size (θ) by

$$l \;=\; \theta \times D_A, \tag{3.2}$$

where θ is in radians. The angular size distance (D_A) was calculated using Ned Wright's cosmology calculator (Wright, 2006). The input parameters are redshift (z) to M82 and the standard cosmological parameters ($H_0 = 69.6, \Omega_m = 0.286, \Omega_\Lambda = 0.714$), where H_0 is the Hubble constant, Ω_m is the matter density and Ω_Λ is the dark energy density parameter. The redshift to M82 is $z \approx 0.00067$ (NASA/IPAC Extragalactic Database), and the cosmological parameters are automatically updated on the cosmological calculator. These parameters give an angular size distance of $D_A = 2.927$ Mpc.

The radio luminosities (L_ν) of sources were also calculated. These provide important insight into the energetic output of the 36 sources at L-Band (1–2 GHz). The radio luminosities were calculated using the relation:

$$L_\nu \;=\; 4\pi d^2 S_\nu, \tag{3.3}$$

where d is the distance to M82, S_ν is the integrated flux density in Jy, and L_ν is expressed in W Hz^{-1}. We used the integrated flux densities as listed in column (6) of Table (3.1), and we adopted a distance to M82 of 3.4 Mpc as estimated in Freedman et al. (1994). This distance was converted to SI units using the conversion 1 Mpc $=$ 3.0857×10^{22} m.

The results of the physical linear sizes and radio luminosities of the sources are summarized in Table (3.3), and the columns (1)–(5) are detailed below:

- Columns (1) and (2) are the same as in Table (3.1).

© University of Pretoria

UNIVERSITEIT VAN PRETORIA
UNIVERSITY OF PRETORIA
YUNIBESITHI YA PRETORIA

- Column (3) lists the deconvolved major and minor angular sizes determined via elliptical Gaussian fitting in CASA.
- Column (4) lists the physical linear sizes of the sources in parsecs.
- Columns (5) lists the luminosities of the radio sources at 1.5 GHz in units of W Hz^{-1}.

© University of Pretoria

UNIVERSITEIT VAN PRETORIA
UNIVERSITY OF PRETORIA
YUNIBESITHI YA PRETORIA

TABLE 3.3: Properties of the detected radio sources in the central region of M82

Candidate	Name B1950	$\theta_{maj} \times \theta_{min}$ (arcsec)	Size (parsec)	L_ν (W Hz^{-1})
(1)	(2)	(3)	(4)	(5)
1.....	37.52+53.1 (N)	0.525×0.098	7.450×1.391	7.220×10^{43}
2.....	38.76+53.5	0.168×0.129	1.972×0.724	8.894×10^{43}
3.....	38.88+54.6 (N)	0.069×0.049	0.979×0.695	6.625×10^{43}
4.....	39.10+57.3	0.230×0.146	3.264×2.072	1.238×10^{45}
5.....	39.40+56.2	0.298×0.164	4.229×2.327	4.772×10^{44}
6.....	39.64+53.3	0.274×0.118	3.888×1.674	1.549×10^{44}
7.....	39.77+56.9	0.514×0.091	7.294×1.291	3.314×10^{44}
8.....	40.32+55.2	0.150×0.190	2.129×2.696	3.877×10^{44}
9.....	40.61+56.3	0.673×0.150	9.550×2.129	1.138×10^{45}
10.....	40.68+55.1	0.253×0.208	3.590×2.952	1.782×10^{45}
11.....	41.30+59.6	0.173×0.057	2.455×0.809	5.505×10^{44}
12.....	41.95+57.5	0.164 × 0.124	2.327 × 1.760	2.099×10^{45}
13.....	42.67+55.6	0.247×0.205	3.505×2.909	4.457×10^{44}
14.....	42.67+56.3	0.133 × 0.073	1.887 × 1.036	2.614×10^{43}
15.....	43.18+58.2	0.181×0.154	2.568×2.185	1.072×10^{45}
16.....	43.31+59.2	0.167×0.133	2.340×1.887	2.756×10^{45}
17.....	43.72+62.6	0.109×0.040	1.547×0.568	1.921×10^{44}
18.....	44.01+59.6	0.141×0.052	2.000×0.738	1.520×10^{45}
19.....	44.28+59.3	0.116×0.086	1.646×1.220	5.754×10^{44}
20.....	44.34+57.8	0.261×0.108	3.704×1.533	3.624×10^{44}
21.....	44.40+61.8	0.358×0.269	5.080×3.817	7.469×10^{45}
22.....	44.51+58.2	0.286×0.185	4.058×2.625	7.339×10^{44}
23.....	44.89+61.2	0.154×0.040	2.185×0.567	3.123×10^{44}
24.....	45.17+61.2	0.086×0.039	1.220×0.553	1.890×10^{45}
25.....	45.24+65.2	0.170×0.122	2.412×1.731	4.486×10^{44}
26.....	45.38+05.5 (N)	1.231 × 0.378	17.469 × 5.364	9.945×10^{44}
27.....	45.42+67.4	0.187×0.154	2.654×2.185	6.343×10^{44}
28.....	45.52+64.7	0.200×0.060	2.838×0.851	5.228×10^{44}

© University of Pretoria

UNIVERSITEIT VAN PRETORIA
UNIVERSITY OF PRETORIA
YUNIBESITHI YA PRETORIA

Table (3.3) continued

Candidate	Name	$\theta_{maj} \times \theta_{min}$ (arcsec)	Size (parsec)	L_ν (W Hz^{-1})
(1)	(2)	(3)	(4)	(5)
29.....	45.75+65.3	0.238×0.169	3.377×2.398	7.242×10^{44}
30.....	45.79+64.0	0.066×0.037	0.937×0.525	1.500×10^{44}
31.....	45.89+63.8	0.115×0.084	1.632×1.192	4.923×10^{44}
32.....	46.52+63.9	0.146×0.109	2.072×1.547	5.510×10^{44}
33.....	46.56+73.8	0.101×0.093	1.433×1.320	2.917×10^{44}
34.....	46.70+67.1	0.314×0.186	4.456×2.639	5.640×10^{44}
35.....	48.32+12.7 (N)	0.387×0.118	5.492×1.674	1.638×10^{44}
36.....	SN 2008iz	0.158×0.120	2.242×1.703	8.800×10^{45}

3.2 Source Classification

3.2.1 Morphology Analysis

In this section, we examined the morphology of the sources in Fig. 3.2 to classify them and to confirm previous classifications. Sources 3 and 35, two of the newly detected sources, show shell structure. Source 26, also a newly detected source, shows a partial shell structure. All sources with similar shapes, showing either shell or partial shell structure, were assumed to be SNRs.

Source 1, the last of the newly detected sources, presents a challenge for morphological analysis as no discernible contours are present in the image in Figure 3.2. This absence of contours is likely due to the source's low peak flux density of 0.224 mJy beam^{-1}, which is below our established minimum detectable signal of 0.356 mJy beam^{-1} (corresponding to a 6σ detection threshold, where $\sigma = 59.36$ μJy). Despite falling below this strict S/N cut, PyBDSF (Mohan and Rafferty, 2015) identified this source during the initial source detection phase. This detection, even with a flux below the nominal threshold, could be attributed to local variations in the noise or specific characteristics of the source's spatial distribution that triggered the PyBDSF algorithm. While the lack of contours prevents a robust assessment of its structure directly from the image, CASA analysis did yield deconvolved major and minor axes measurements (see Table 3.3), suggesting some level of resolved structure is inferred by the fitting process despite the faintness of the emission. The inclusion of this source in our catalogue highlights the complexities of source detection near the sensitivity limit and the potential for source finders to identify objects that may not be clearly visible through standard contouring levels based on the global RMS noise.

Out of the 36 detected sources, 31 have been detected and classified in a recent study by Fenech et al. (2008). Source 6, for example, was classified as an SNR and considering the radio structure in this study, it might have evolved into a bipolar SNR.

Since the goal was to make an updated catalogue, classification by morphology alone was insufficient. A spectral index analysis was necessary to complement the morphological analysis, particularly for the newly detected sources. Additionally, spectral index measurements were used to confirm previous classifications of the 31 sources by comparing them with the results from Fenech et al. (2008).

© University of Pretoria

UNIVERSITEIT VAN PRETORIA
UNIVERSITY OF PRETORIA
YUNIBESITHI YA PRETORIA

TABLE 3.4: Division of the observed L-Band into eight subbands. Each subband has a bandwidth of 64 MHz, with its central frequency listed alongside the frequency range covered. These subbands enable the study of spectral properties of sources in M82.

Subband	Central Frequency (GHz)	Frequency Range (GHz)	Bandwidth
0	1.285	1.253 - 1.317	64
1	1.349	1.317 - 1.381	64
2	1.413	1.381 - 1.445	64
3	1.477	1.445 - 1.509	64
4	1.541	1.509 - 1.573	64
5	1.605	1.573 - 1.637	64
6	1.669	1.637 - 1.701	64
7	1.733	1.701 - 1.765	64

3.2.2 Subbands and Spectral Indices

In the discussion of the CLEAN algorithm in section 2.4.2, it was discussed that the package used to implement the CLEAN algorithm is WSCLEAN (Offringa, McKinley, Hurley-Walker, et al., 2014; Offringa and Smirnov, 2017). WSCLEAN allows the total bandwidth of an observation to be split into small frequency ranges known as subbands by specifying the number of divisions during imaging. This division helps in analyzing how the radio emission from sources changes with frequency. For this dataset, the L-Band was divided into eight subbands, each with a bandwidth of 64 MHz. These subbands cover the frequency range from approximately 1.253 GHz to 1.765 GHz, with their central frequencies listed in Table (3.4).

Breaking the bandwidth into subbands serves two main purposes. First, it enables us to study the spectral properties of the detected sources by providing flux density measurements at multiple frequencies. Second, it helps identify and mitigate issues such as noise or interference that may affect specific frequency ranges. In this section, the flux density measurements from the subbands were used to calculate the spectral index (α), a parameter that describes how the flux density of a source varies with frequency. The spectral index can reveal important information about the physical processes responsible for the radio emission. For example, a spectral index of approximately $+0.1$ at radio frequencies indicates thermal free-free emission, which is characteristic of ionized gas in HII regions. In contrast, a steep negative spectral index, typically ranging from -0.5 to -1.0, indicates non-thermal synchrotron emission, commonly associated with SNRs or regions with relativistic electrons spiralling in magnetic fields. In rare instances, the synchrotron spectra can be steeper, reaching values as -3, often associated with young SNRs. The spectral index was then used to classify the source emitting the radiation.

The spectral index is calculated using the relationship:

$$S_\nu \propto \nu^\alpha \tag{3.4}$$

$$\alpha = \frac{\log(S_1/S_2)}{\log(\nu_1/\nu_2)} \tag{3.5}$$

where S_1 and S_2 are the flux densities of the source at central frequencies ν_1 and ν_2, respectively. For the classification in this section, subbands 1 and 7, with central frequencies of 1.349 GHz and 1.733 GHz, were used to calculate the spectral index.

© University of Pretoria

UNIVERSITEIT VAN PRETORIA
UNIVERSITY OF PRETORIA
YUNIBESITHI YA PRETORIA

These subbands were chosen to provide a sufficient frequency separation within the L-Band. Although subband 0 has the lowest frequency in the L-band, it was not used due to significant RFI contamination and was removed entirely during the imaging process, making subband 1 the lowest usable subband.

The flux densities for each source in subbands 1 and 7 were measured from the subband images using the same CASA procedure as described in the introductory section of this chapter, as used when recording the flux densities for Table 3.1. Peak flux density measurements were used to calculate the spectral index for each source across the selected subbands. Peak fluxes were chosen because they tend to be less sensitive to noise and contamination compared to integrated fluxes, especially for compact and unresolved sources. By using peak fluxes uniformly for all sources, the analysis ensures consistency and avoids potential biases arising from the varying spatial extents of the sources.

The reliability of the calculated spectral indices was assessed based on the following criteria:

1. A reliable spectral index requires a high S/N in both subbands 1 and 7. The calculated S/N range was 1 to 155 (excluding source 36). Measurements with S/N below 4 in both subbands were flagged as less reliable, especially if they failed criterion 3 as well. However, more emphasis was put on criterion 3.

2. Sources with large uncertainties or extreme flux variation between subbands were considered unreliable.

3. Spectral indices deviating from expected ranges ($-3 \leq \alpha \leq +1$) without clear justification were treated with caution.

Sources meeting these criteria were classified based on their spectral index. Table (3.5) summarizes the results, including classifications from Fenech et al. (2008), for comparison.

Out of the four newly detected sources, three of them (sources 1, 3, and 35) fail criterion 1 with a S/N below 4 in both subbands. The spectral indices of sources 1 and 35, however, point towards an SNR. This is consistent with the environment as SNRs in almost all evolutionary stages are expected in the starburst of M82. Although source 1 has a flux density below the minimum detectable signal, it was hard to dismiss it as a false detection due to being detected at 6σ; as a result, it was thought to be an SNR. For source 35, its radio structure, as seen in Fig. 3.2, strongly complements the spectral index pointing towards an SNR. Source 3 was hard to classify as it also failed criterion 3, showing an unreliable spectral index.

Source 26, the last newly detected source, has an S/N above 4 in both subbands. However, its morphology (source 26 in Fig. 3.2), though it appears as a partial shell, could be diffuse emission and its spectral index is unreliable; as a result, it was difficult to classify. These sources will be discussed more in section 4.2.

Out of the 31 sources included in Fenech et al. (2008), only sources 2, 6, 17 and 28 have S/N below 4 in one or both subbands. During source detection using PyBDSF, source six was detected as a double source as can be seen in its morphological structure (source 6 in Fig. 3.2). Its Spectral index points to an SNR and was also classified as an SNR in Fenech et al. (2008). The double-bright-spot morphology is consistent with shell-like or bipolar structures commonly observed in SNRs, arising from non-uniform shock expansion or enhanced emission regions where the shock interacts with denser ISM. As a result source 6 was then thought to be SNR. Source 17 spectral index points towards an SNR, and its morphological structure (source 17 in Fig.

© University of Pretoria

UNIVERSITEIT VAN PRETORIA
UNIVERSITY OF PRETORIA
YUNIBESITHI YA PRETORIA

3.2) is partially shell-like and could also be bipolar, so it was thought to be an SNR. Source 2, however, took an interesting turn. Its spectral index points towards a SNR, while it had been classified as an HII region in Fenech et al. (2008). A key challenge arose in classifying source 2; the spectral index derived from the subbands did not provide a clear-cut answer. Initially, this conflict of classification was attributed to its S/N being low in subband 1. That is because the same situation is evident in source 28; it has low S/N in subband 1 and a spectral index pointing towards an HII region, while it had been classified as an SNR in Fenech et al. (2008). However, this conclusion did not stand as source 18, although it has high S/N in both subbands, has a spectral index pointing towards an HII region while it had been classified as an SNR in Fenech et al. (2008).

Given the inconsistencies and potential unreliability observed in the spectral index classifications derived solely from our L-band subband data for several sources (as highlighted by the conflicting classifications with Fenech et al. 2008 for sources 2, 18, and 28, and the low S/N issues for some sources in one or both subbands), we adopted a cautious approach in our initial classification based on this dataset alone. Consequently, we only confidently proceeded with the classification of 18 sources where the spectral index derived from the subbands showed good agreement with their morphological features and exhibited high S/N in at least one subband (if its one subband then the spectral index should agree with its morphology), but preferably both subbands, such as sources 12 and 16, in particular, which seemed to be more accurate due to their morphological structure and very high S/N. The results are summarized in Table (3.5). For the remaining sources, it was not possible to conclude with confidence that the classifications obtained from the subbands spectral index results are more reliable than those in Fenech et al. (2008), as their study is based on more comprehensive and detailed data.

To improve the reliability of the spectral index analysis and to complete the classifications, the C-Band peak flux densities of the 31 sources from Fenech et al. (2008) were combined with the L-band peak flux densities obtained in this study to compute the spectral index using the relations in equations 3.4 and 3.5. This was possible because the sources in M82 have had steady fluxes over many years in the past, with little change (Ulvestad and Antonucci, 1994). The results are summarized in Table (3.6)

Combining the C-Band and L-Band fluxes, we were able to confirm the classifications in Fenech et al. (2008), except for source 2. Just like the subband spectral index analysis, the C-Band and L-Band combination also points towards an SNR when it had been identified as an HII region. Source 2 (38.76+54.6) is discussed further in the next chapter (chapter 4).

© University of Pretoria

UNIVERSITEIT VAN PRETORIA
UNIVERSITY OF PRETORIA
YUNIBESITHI YA PRETORIA

TABLE 3.5: This table classifies the 36 sources selected from the central region of M82 using L-band subband flux densities. Columns (4) and (6) list the peak flux densities from subbands 1 and 7, respectively. These subband peak flux densities were combined to calculate spectral indices for each source using the relations in equations 3.4 and 3.5. These calculated spectral indices were then compared to the C-band classifications from Fenech et al. (2008), summarised in column (8).

Candidate	Name	Subband 1 S_1	Subband 1 S/N	Subband 7 S_2	Subband 7 S/N	Spectral Index	Fenech et al. (2008)	This Study
	B1950	(mJy/beam)		(mJy/beam)		(α)	comments	comments
(1)	(2)	(3)	(4)	(5)	(6)	(7)	(8)	(9)
1.....	37.52+53.1 (N)	0.452±0.014	1	0.362±0.026	3	-0.886	SNR	SNR
2.....	38.76+53.5	0.639±0.116	2	0.562±0.032	4	-0.513	HII	-
3.....	38.88+54.6 (N)	0.787±0.033	2	0.291±0.042	2	-3.972	SNR	-
4.....	39.10+57.3	4.230±0.190	14	2.690±0.130	23	-1.807	SNR	SNR
5.....	39.40+56.2	1.840±0.130	6	0.856±0.085	7	-3.055	SNR	SNR
6.....	39.64+53.3	0.389±0.177	1	0.341±0.045	2	-0.526	SNR	SNR
7.....	39.77+56.9	1.280±0.110	4	0.481±0.031	4	-3.907	SNR	-
8.....	40.32+55.2	1.410±0.250	4	1.100±0.110	9	-0.991	SNR	SNR
9.....	40.61+56.3	1.190±0.280	4	0.895±0.070	7	-1.137	SNR	SNR
10.....	40.68+55.1	6.930±0.300	23	4.060±0.210	34	-2.135	SNR	-
11.....	41.30+59.6	3.000±0.110	10	2.411±0.086	20	-0.873	SNR	SNR
12.....	41.95+57.5	15.320±0.590	52	13.340±0.190	114	-0.552	Bipolar ?	SNR
13.....	42.67+55.6	1.390±0.380	4	0.934±0.139	7	-1.587	SNR	SNR
14.....	42.67+56.3	1.560±0.140	5	1.040±0.300	8	-1.619	SNR	SNR
15.....	43.18+58.2	7.110±0.660	24	5.060±0.430	43	-1.358	SNR	SNR
16.....	43.31+59.2	22.070±0.970	75	18.120±0.350	155	-0.787	SNR	SNR
17.....	43.72+62.6	1.070±0.089	3	0.951±0.159	8	-0.471	SNR	SNR
18.....	44.01+59.6	6.410±0.330	21	10.560±0.240	90	1.993	SNR	-
19.....	44.28+59.3	2.210±0.280	7	1.460±0.160	12	-1.655	SNR	SNR
20.....	44.34+57.8	1.700±0.140	5	0.794±0.142	6	-3.039	SNR	-
21.....	44.40+61.8	1.230±0.340	4	1.480±0.150	12	0.739	SNR	-
22.....	44.51+58.2	2.280±0.340	7	1.010±0.140	8	-3.251	SNR	-
23.....	44.89+61.2	2.210±0.340	7	1.101±0.097	9	-2.782	SNR	-
24.....	45.17+61.2	10.950±0.430	37	9.190±0.250	78	-0.700	SNR	SNR
25.....	45.24+65.2	1.900±0.150	6	1.139±0.070	9	-2.043	SNR	-
26.....	45.38+05.5 (N)	1.360±0.210	4	0.621±0.107	5	-3.129	SNR	-
27.....	45.42+67.4	2.580±0.190	8	1.490±0.100	12	-2.192	SNR	-
28.....	45.52+64.7	0.987±0.135	3	1.052±0.089	9	0.255	SNR	-
29.....	45.75+65.3	2.770±0.190	9	1.390±0.120	11	-2.753	SNR	-
30.....	45.79+64.0	1.390±0.130	4	0.744±0.048	6	-2.495	SNR	-
31.....	45.89+63.8	2.690±0.170	9	1.750±0.130	14	-1.716	SNR	SNR
32.....	46.52+63.9	2.740±0.130	9	1.859±0.071	15	-1.549	SNR	SNR
33.....	46.56+73.8	1.800±0.070	6	1.053±0.032	9	-2.140	SNR	-
34.....	46.70+67.1	1.190±0.140	4	0.831±0.109	7	-1.434	SNR	SNR
35.....	48.32+12.7 (N)	0.818±0.039	2	0.404±0.030	3	-2.816	SNR	SNR
36.....	SN 2008iz	60.000±1.400	204	57.080±0.930	488	-0.199	SN	-

© University of Pretoria

UNIVERSITEIT VAN PRETORIA
UNIVERSITY OF PRETORIA
YUNIBESITHI YA PRETORIA

TABLE 3.6: This table classifies the 31 sources observed in the C-band by Fenech et al. (2008). Columns (3) and (4) list the peak and integrated flux densities from those C-band observations. The peak flux densities from column (3) were combined with the L-band peak flux densities from this study (Table 3.1, column 5) to calculate spectral indices using equations 3.4 and 3.5. These calculated spectral indices were then compared to the original C-band classifications, summarised in column (7). The newly detected source and SN 2008iz lack spectral indices as they were not present in the C-band observations.

Candidate	Name B1950	Peak (mJy/beam)	Int. Flux (mJy)	S/N	Spectral Index (α)	Fenech et al. (2008)	This Study
(1)	(2)	(3)	(4)	(5)	(6)	(7)	(8)
1.....	37.52+53.1 (N)	-	-	-	-	-	-
2.....	38.76+53.5	0.181±0.017	0.272±0.030	10	-1.054	HII	SNR
3.....	38.88+54.6 (N)	-	-	-	-	-	
4.....	39.10+57.3	0.381±0.019	3.555±0.084	22	-1.806	SNR	SNR
5.....	39.40+56.2	0.154±0.018	0.820±0.071	9	-1.555	SNR	SNR
6.....	39.64+53.3	0.099±0.016	1.120±0.310	5	-1.186	SNR	SNR
7.....	39.77+56.9	0.089±0.016	0.180±0.022	5	-1.542	SNR	SNR
8.....	40.32+55.2	0.114±0.017	0.253±0.030	6	-2.163	SNR	SNR
9.....	40.61+56.3	0.104±0.016	0.409±0.039	6	-2.051	SNR	SNR
10.....	40.68+55.1	0.484±0.016	6.093±0.080	28	-1.995	SNR	SNR
11.....	41.30+59.6	0.565±0.027	2.296±0.081	33	-1.343	SNR	SNR
12.....	41.95+57.5	14.395±0.028	17.035±0.073	846	-0.044	SNR	SNR
13.....	42.67+55.6	0.161±0.024	1.104±0.082	9	-1.800	SNR	SNR
14.....	42.67+56.3	0.239±0.021	0.843±0.063	14	-1.334	SNR	SNR
15.....	43.18+58.2	0.943±0.027	3.908±0.088	55	-1.559	SNR	SNR
16.....	43.31+59.2	5.273±0.018	9.530±0.051	310	-1.098	SNR	SNR
17.....	43.72+62.6	0.154±0.017	0.274±0.030	9	-1.599	SNR	SNR
18.....	44.01+59.6	9.984±0.024	19.435±0.072	587	-0.080	SNR	SNR
19.....	44.28+59.3	0.335±0.019	1.642±0.063	19	-1.490	SNR	SNR
20.....	44.34+57.8	0.242±0.019	0.954±0.061	14	-1.171	SNR	SNR
21.....	44.40+61.8	0.142±0.023	0.631±0.063	8	-1.829	SNR	SNR
22.....	44.51+58.2	0.212±0.018	1.446±0.067	12	-1.621	SNR	SNR
23.....	44.89+61.2	0.212±0.017	0.858±0.049	12	-1.673	SNR	SNR
24.....	45.17+61.2	2.427±0.021	6.310±0.069	142	-1.277	SNR	SNR
25.....	45.24+65.2	0.193±0.019	1.065±0.063	11	-1.772	SNR	SNR
26.....	45.38+05.5 (N)	-	-	-			
27.....	45.42+67.4	0.271±0.016	1.152±0.059	15	-1.650	SNR	SNR
28.....	45.52+64.7	0.095±0.017	0.173±0.029	5	-2.208	SNR	SNR
29.....	45.75+65.3	0.228±0.019	1.522±0.087	13	-1.742	SNR	SNR
30.....	45.79+64.0	0.121±0.015	0.192±0.025	7	-1.710	SNR	SNR
31.....	45.89+63.8	0.482±0.016	1.240±0.044	28	-1.346	SNR	SNR
32.....	46.52+63.9	0.130±0.018	0.650±0.068	7	-2.367	SNR	SNR
33.....	46.56+73.8	0.130±0.018	0.556±0.054	7	-2.017	SNR	SNR
34.....	46.70+67.1	0.159±0.018	1.440±0.097	9	-1.616	SNR	SNR
35.....	48.32+12.7 (N)	-	-	-	-	-	-
36.....	SN 2008iz	-	-	-	-	-	-

© University of Pretoria

Chapter 4

Discussion

This chapter presents the findings from the analysis of 1.5 GHz *e*-MERLIN L-Band observations of M82, as described in the previous chapter (chapter 3). The study focuses on identifying and analyzing compact radio sources in the central starburst region of M82 using the high sensitivity and resolution of the *e*-MERLIN interferometer. The observations achieved a peak flux density of 61.261 mJy beam^{-1} and a noise level of 59.36 μJy beam^{-1}, corresponding to a dynamic range in excess of a thousand. This has allowed the identification of compact sources in this dense and complex environment.

In total, 36 sources were detected, 31 of which match sources listed in the earlier study by Fenech et al. (2008), which reported 55 sources from deep 5 GHz MERLIN observations. The difference in the number of detected sources highlights the challenges of determining the exact population of compact sources in M82. Differences in observing frequencies, sensitivity, and resolution affect which sources can be detected. For example, the 5 GHz observations in (Fenech et al., 2008) had a much lower noise level of 17 μJy beam^{-1}, making them more sensitive to faint sources. Additionally, the higher frequency of 5 GHz is better suited for detecting compact HII regions with flat spectral indices, which are harder to identify at lower frequencies like 1.5 GHz.

Four sources detected in this study had not been reported in earlier work. However, detecting a source that was not previously observed does not necessarily mean it is young. Many factors, such as observational sensitivity, background emission, or source variability, can affect whether a source is detected. These factors make it difficult to determine the exact number of compact sources in M82.

This chapter will discuss the implications of these findings, including the spatial distribution and flux densities of the detected sources, their potential classifications, and comparisons with previous studies. The analysis will also address the limitations of these observations and the challenges in interpreting the population of compact radio sources in a complex starburst galaxy like M82.

4.1 Some Unique Sources in The Central Region of M82

This section focuses on sources from the 1.5 GHz *e*-MERLIN L-Band observations of M82 that exhibit unique characteristics, setting them apart from typical SNRs or HII regions. These include sources showing significant morphological evolution, notable flux variability, or unusual features such as bipolar or asymmetric structures. The newly detected or previously unclassified sources are discussed in section 4.2.

© University of Pretoria

UNIVERSITEIT VAN PRETORIA
UNIVERSITY OF PRETORIA
YUNIBESITHI YA PRETORIA

4.1.1 SN 2008iz

The source that completes the total number of the detected sources in this study to 36 is supernova SN 2008iz. Located in the starburst galaxy M82, this source provides an exceptional case for studying the evolution of a core-collapse SN, particularly due to its location in a highly obscured environment. First detected in 2009 as a bright radio transient (Brunthaler et al., 2009a; Brunthaler et al., 2009b; Brunthaler et al., 2009c), its explosion date has been estimated to be February 18, 2008 (Marchili et al., 2010). The source remains undetected in optical and X-ray wavelengths due to the high extinction in its environment, with estimates ranging from $A_v \sim 24.4$ to 48.9 mag (Brunthaler et al., 2009b; Mattila et al., 2013). Consequently, radio observations have been instrumental in understanding its evolution.

From the 2016 L-band observations at 1.5 GHz in this study, we measured a peak flux density of 63.620 mJy beam^{-1}. The integrated flux density was initially measured as 54.700 mJy. However, following the approach outlined in chapter 3, where for some resolved sources the peak flux density was qualified as the representative flux density when the integrated flux was lower, we adopt the peak flux density of 63.620 mJy as the effective integrated flux for SN 2008iz.

The measured peak flux density of SN 2008iz (63.620 mJy beam^{-1}) is notably higher than the peak flux density of the overall image (Fig. 3.1, 61.261 mJy beam^{-1}). This apparent discrepancy can be attributed to several factors. Firstly, the overall image peak value represents the intensity of a single pixel, which can be influenced by residual calibration errors or deconvolution artifacts present across the image, potentially suppressing the true peak of the brightest source. Secondly, the peak flux density of SN 2008iz was derived from a Gaussian fit using CASA's `imfit` task, which models the source emission as a smooth distribution. The peak of this fitted Gaussian can sometimes provide a more robust estimate of the true convolved peak intensity compared to a single pixel value. Furthermore, self-calibration procedures often optimize the image quality around the brightest sources, potentially leading to a more accurate recovery of their peak fluxes. Given that SN 2008iz is the dominant source in the field and was likely a primary driver for the self-calibration, its fitted peak flux is considered a reliable measurement, even if it exceeds the nominal peak value of the final image.

The deconvolved major and minor dimensions are 0.158×0.120 arcseconds. The spectral index derived from subband fluxes in section 3.2.2 was -0.199, which, given the high S/N in both subbands for SN 2008iz, is considered reliable. This steep spectral index suggests the SN has transitioned into the later stages of evolution, aligning with ongoing interaction between the expanding shock wave and the dense CSM, where synchrotron emission dominates (Brunthaler et al., 2010; Marchili et al., 2010).

Previous VLBI studies revealed a shell-like morphology for SN 2008iz, expanding at an early velocity of ~ 21000 km s^{-1}, with a deceleration index $m = 0.89 \pm 0.03$, indicating interaction with a dense medium (Brunthaler et al., 2010). The asymmetry observed in later epochs, with bright structures in the southern part of the shell, suggests variations in the density of the surrounding CSM (Kimani et al., 2016). These results are consistent with the behaviour of core-collapse SNe, where the radio emission arises from relativistic particles accelerated in magnetic fields amplified at the shock front (Weiler et al., 2002).

Further supporting this evolutionary stage, the steep decline in the radio light curve aligns with models that exclude significant synchrotron self-absorption, but account for early free-free absorption (Marchili et al., 2010). Comparisons with SN

© University of Pretoria

UNIVERSITEIT VAN PRETORIA
UNIVERSITY OF PRETORIA
YUNIBESITHI YA PRETORIA

1993J highlight environmental differences, notably the asymmetric expansion of SN 2008iz compared to SN 1993J's circular symmetry (Kimani et al., 2016).

Overall, the 2016 observations, coupled with VLBI and light curve data (Gendre et al., 2013), indicate SN 2008iz has evolved into a SNR. The spectral index of -0.199, the decelerating expansion, and the asymmetric structure, particularly in the southern regions, suggest a transition from CSM to ISM interaction. This transition, along with the observed light curve decline, confirms SN 2008iz is in a later evolutionary phase, moving beyond a young SN.

4.1.2 38.76+53.5

The source 38.76+53.5 in M82 has been the subject of extensive study, with earlier classifications identifying it as an HII region. This classification was primarily based on observations of its brightness, temperature, and spectral properties. McDonald et al. (2002) identified this source as an HII region due to its relatively low brightness temperature ($\sim$ 10000 K) and a spectral index consistent with thermal free-free emission. Additional support for this classification came from earlier works by Wills et al. (1997), and Allen and Kronberg (1999), who noted that sources with flat or slightly inverted spectra ($\alpha \sim -0.1$ to 0.0) were characteristic of ionized gas in HII regions. These studies relied on high-resolution observations, including MERLIN and VLA data, to distinguish between thermal and non-thermal sources in the crowded central region of M82.

In this study, we reanalyzed the nature of 38.76+53.5 using the data obtained from the 2016 *e*-MERLIN L-band observation at 1.5 GHz. The imaging resolution, with a clean beam size of 0.17×0.13 arcseconds, was sufficient to resolve the compact structure of the source. The source exhibited a peak flux density of 0.643 mJy beam^{-1} and an integrated flux density of 0.633 mJy. By the same procedure outlined in chapter 3, the integrated flux density for this source is qualified to be the peak flux density. These measurements are consistent with the compact radio sources previously catalogued in M82 (Kronberg, Biermann, and Schwab, 1985; Kronberg and Sramek, 1985; Kronberg, 1988). Furthermore, the deconvolved dimensions of the source were derived to be 0.168 arcseconds for the major axis and 0.129 arcseconds for the minor axis. These sizes are comparable to other compact sources in M82, which include both HII regions and SNRs (Fenech et al., 2008).

A key part of this analysis involved determining the spectral index of the source. Using subband images at L-band as described in section 3.2.2, we calculated a spectral index of -0.513. This value deviates significantly from the flat or slightly positive spectral indices expected for HII regions dominated by thermal free-free emission. Instead, it strongly indicates a non-thermal synchrotron origin, which is characteristic of SNRs. To further investigate this result, we incorporated flux densities from C-band (4.994 GHz) data published by Fenech et al. (2008). Combining the L-band and C-band peak flux densities, we derived a steeper spectral index of -1.054, further reinforcing the conclusion that the emission mechanism is non-thermal.

The findings of this study highlight a potential misclassification of 38.76+53.5 in earlier works. Previous studies may have been influenced by lower-resolution observations or assumptions that thermal emission dominated the detected flux. For instance, the classification of HII regions in M82 often relied on flat spectral indices and brightness temperatures near the detection limit for such sources. In contrast, the spectral index measurements in this study clearly align with synchrotron radiation, which is a hallmark of SNRs. This discrepancy suggests that 38.76+53.5 was incorrectly identified as an HII region and is more accurately classified as an SNR.

© University of Pretoria

UNIVERSITEIT VAN PRETORIA
UNIVERSITY OF PRETORIA
YUNIBESITHI YA PRETORIA

In conclusion, the source 38.76+53.5 in M82, long thought to be an HII region, exhibits spectral characteristics and flux density behaviour that is inconsistent with thermal free-free emission. The derived spectral indices of -0.513 (L-band) and -1.054 (L-band and C-band) point conclusively toward a non-thermal origin consistent with an SNR. This reclassification not only contributes to our understanding of the compact radio source population in M82 but also underscores the importance of multi-frequency, high-resolution observations in accurately identifying the nature of such sources.

4.1.3 41.95+57.5

First detected in 1965 (Bash, 1968), the source 41.95+57.5 used to hold the title of being the brightest and most compact radio source in the central region of M82 (Kronberg and Sramek, 1985; Bartel et al., 1987; Wilkinson and de Bruyn, 1990). Using the 2016 L-Band dataset, we measured its peak flux density to be 15.176 mJy beam^{-1}, with an integrated flux density of 14.710 mJy. By the same procedure outlined in chapter 3, the integrated flux density for this source is qualified to be the peak flux density value. Its dimensions were found to be 0.164 arcseconds along the major axis and 0.124 arcseconds along the minor axis, with a position angle of 62.3°.

Looking at previous studies, Its spectral evolution has been followed since the early 1970s, when the source showed a strong low-frequency turnover. The source has since declined in brightness, and its spectral turnover has moved to lower frequencies (Huang et al., 1994). Its decay rate has been estimated to be 8.8 % per year (Muxlow et al., 2005), suggesting that this source was incredibly bright in the past, with a peak flux likely exceeding 100 Jy. 41.95+57.5 was confirmed through high-resolution global VLBI imaging (McDonald et al., 2001; Muxlow et al., 2001) to have a double-lobed shape, which is quite different from the usual shell-like appearance of SNRs. Over time, researchers, including Muxlow et al. (2005), measured its expansion rate at about 1800 kms^{-1}, giving it an estimated age of around 100 years.

When comparing the 2016 observations with these earlier studies, it is clear that the source has remained structurally consistent. The alignment of the major and minor axes and the measured position angle match well with previous high-resolution VLBI observations (Beswick et al., 2006). This consistency reinforces the idea that 41.95+57.5 is an evolving object, but its exact nature is still debated.

Some researchers suggest that 41.95+57.5 could be the radio afterglow of a gamma-ray burst (GRB; Muxlow et al., 2005). According to Paczyński (1998), GRB afterglows, often called "hypernovae" can result from the collapse of massive stars in star-forming regions, producing intense, focused jets. The double-lobed structure and extremely high inferred luminosity of $\sim 2 \times 10^{30}$ erg/s/Hz are similar to GRB afterglows. Additionally, its location in a compact HII region, roughly 100 light-years across, supports the idea that this source might have formed in a dense, star-forming environment.

On the other hand, it's also possible that 41.95+57.5 is an unusual SNR. The moderate expansion velocity and non-spherical shape could be explained by the influence of a dense and uneven surrounding medium (Pedlar et al., 1999). While this explanation doesn't fully account for all its properties, it's still a plausible scenario given the complex environments within starburst galaxies like M82.

The 2016 data confirm that 41.95+57.5 has been evolving steadily over the years, supporting earlier observations of its morphology and brightness changes. Whether it's a GRB afterglow or a rare type of SNR, this source highlights the complex interactions between massive SF, stellar death, and high-energy processes in galaxies like

© University of Pretoria

UNIVERSITEIT VAN PRETORIA
UNIVERSITY OF PRETORIA
YUNIBESITHI YA PRETORIA

M82. Future observations and detailed analyses are needed to understand its origin and evolution fully, but studying sources like this gives us valuable insights into the extreme conditions in starburst galaxies.

4.1.4 43.31+59.2

The source 43.31+59.2 in the starburst galaxy M82 has been identified as a prominent young SNR through extensive studies, including those by McDonald et al. (2001), and Fenech et al. (2010). The L-band observations in this study provide further insights into its characteristics and evolutionary stage, confirming its status as a highly compact and luminous SNR embedded in the dense ISM of M82.

From our analysis, the derived peak flux density of 19.753 mJy/beam and integrated flux density of 19.913 mJy are consistent with the source's previously reported brightness levels. McDonald et al. (2001) reported comparable flux densities at 1.6 GHz, supporting the conclusion that 43.31+59.2 is among the most luminous SNRs in M82. The dimensions of the source, measured as a major axis of 0.167 arcseconds and a minor axis of 0.133 arcseconds, align with the scale of young SNRs interacting with a dense ISM, as observed in previous MERLIN and wide-field Global VLBI studies (Fenech et al., 2010). The clean beam size of 0.17 arcseconds $\times$ 0.13 arcseconds ensures reliable resolution of the source's structure, further validating these measurements.

Additionally, the spectral index of -1.098 derived from comparing the L-band data from this study with archival C-band observations (Fenech et al., 2008) reveals steep synchrotron emission. This steep index is indicative of ageing electron populations and possibly enhanced absorption effects in the dense environment of M82. Fenech et al. (2008) noted similar spectral properties for compact SNRs in M82, emphasizing the unique conditions of the starburst region.

Historical observations have consistently identified 43.31+59.2 as a rapidly expanding remnant. McDonald et al. (2001) measured expansion velocities of 9000 to 11000 km s^{-1}, highlighting its energetic origin and rapid interaction with the surrounding ISM. The results of this study, particularly the compact dimensions and high flux densities, support these conclusions and suggest that the remnant's expansion is constrained by the high-pressure environment of M82's central region. Moreover, the deceleration parameters reported by Fenech et al. (2010) align with characteristics of SNRs transitioning into an interaction-dominated phase, consistent with the observations in this study.

The significance of these findings extends beyond the characterization of 43.31+59.2 itself. This remnant serves as a key tracer for the intense SF and feedback processes occurring in M82. Its rapid evolution and luminous radio emission underscore the role of young SNRs in driving ISM enrichment and shaping the dynamics of starburst galaxies. Moreover, the observed compactness and steep spectral index provide valuable insights into SNR evolution under the extreme conditions of high-density environments.

4.2 Newly Detected Sources

In Section 3.2.2, we attempted to classify four newly detected sources—37.52+53.1, 38.88+54.6, 45.38+05.5, and 48.32+12.7—using subband flux densities. Only sources

© University of Pretoria

UNIVERSITEIT VAN PRETORIA
UNIVERSITY OF PRETORIA
YUNIBESITHI YA PRETORIA

TABLE 4.1: The radio properties for the newly detected sources

Candidate	Name B1950	Peak (C-band, 2015) (mJy/beam)	Int. Flux (C-band, 2015) (mJy/beam)	Spectral Index (α)	comments
(1)	(2)	(3)	(4)	(5)	(6)
1.....	37.52+53.1 (N)	0.046 ± 0.004	0.045 ± 0.004	-1.185	SNR
3.....	38.88+54.6 (N)	0.075 ± 0.008	0.144 ± 0.014	-1.267	SNR
26.....	45.38+05.5 (N)	0.065 ± 0.007	0.987 ± 0.099	-1.832	SNR
35.....	48.32+12.7 (N)	0.056 ± 0.006	0.301 ± 0.030	-1.733	SNR

37.52+53.1 and 45.38+05.5 could be classified, albeit with low confidence. The C-band data from Fenech et al. (2008) could not be used, as none of these sources were among the 55 previously detected therein.

In this section we introduce a 2015 C-band data set in which the new sources were also detected. The C-band observations were conducted at a central frequency of 5.7 GHz, with a frequency range spanning 5.26 GHz to 5.95 GHz. Both left-left (LL) and right-right (RR) polarizations were utilized. The observations commenced on 2015-05-28 at 16h20 and concluded on 2015-05-31 at 09h59. The total bandwidth of 1024 MHz was divided into 8 spectral windows (spw), each with a bandwidth of 128 MHz, further subdivided into 128 channels, each 1.00 MHz wide.

This study was aimed at L-band studies of the sources in M82 using the 2016 L-band data set. However, a comparison of the 2016 L-band data with the 2015 C-band data set allowed us to compute the spectral index of the newly detected sources to classify them in order to complete the catalogue. The source 37.52+53.1 (source 1 in Fig. 3.2) corresponds to 37.53+53.2 in the 2015 C-band data. Similarly, 38.88+54.6 (source 3 in Fig. 3.2) corresponds to 38.90+54.4, 45.38+05.5 (source 26 in Fig. 3.2) corresponds to 45.42+65.5, and 48.32+12.7 corresponds to 48.34+72.7 . Fig. 4.1 show contour maps of the sources as seen in the 2015 C-band data (viewed using CASA `imview` task; CASA Team et al., 2022), and their peak and integrated flux densities are summarized in Table (4.1).

As can be seen in Fig. 4.1, the images have been numbered the same as in Fig. 3.2 to make it easier to compare the figures.

The correspondence between the sources was established from the positions of the sources. For example, the RA of 37.52+53.1 (2016 L-band data in this study) and 37.53+53.2 (2015 C-band data) differ by only 0.090 arcseconds. This offset is significantly smaller than the synthesized beam, indicating that both positions correspond to the same astronomical source. The source positions as derived from the 2015 C-band data are summarized in Table (4.1) together with their flux densities. Below, we describe the process of deriving the flux densities at C-band using the CASA imaging tool:

- 37.52+53.1: This source was detected at five sigma. As can be seen in image (1) of Fig. 4.1, the source is resolved into multiple components, and so the flux was taken from fitting the brightest component. Fitting was done by drawing a region across 3 sigma areas and summing them. From this we derived a peak flux density of 0.046 ± 0.004 mJy beam^{-1} and integrated flux density of 0.045 ± 0.004 mJy. The same procedure outlined in chapter 3 was followed to qualify the integrated flux density to match the peak flux density value. This C-band peak flux density was used together with the peak flux density of the source at L-band as summarized in column (5) of Table (3.1) to obtain a spectral index of -1.185. From this result, we concluded that we were observing an SNR.

© University of Pretoria

UNIVERSITEIT VAN PRETORIA
UNIVERSITY OF PRETORIA
YUNIBESITHI YA PRETORIA

- 38.88+54.6: This source (along with the next two sources discussed) was analyzed using the same approach as the previous source. We derived a peak flux density of 0.075 ± 0.008 mJy beam^{-1} and an integrated flux density of 0.144 ± 0.014 mJy. Combining these results with the L-band measurements, we calculated a spectral index of $\alpha = -1.267$, which is consistent with an SNR. Examination of its structure in both bands (source 3 in Fig. 3.2 and Fig. 4.1) reveals a shell-like morphology, further supporting the classification of this source as an SNR.

- 45.38+05.5: From the images of the source in both bands (source 26 in Fig. 3.2 and Fig. 4.1), it appears highly resolved and diffuse, indicating that it is not a compact object but rather an extended emission region, likely a supernova remnant (SNR) or diffuse non-thermal emission within the starburst region of M82. Using the same approach as previously stated, we measured a peak flux density of 0.065 ± 0.007 mJy beam^{-1} and a total flux density within a 3σ region of 0.987 ± 0.099 mJy. The significant difference between peak and total flux confirms that the source is not point-like but extended, with emission spread over multiple beams, further supporting its classification as a resolved structure rather than a compact, unresolved object. Using the peak flux along with the L-band flux, we calculated a spectral index of $\alpha = -1.832$. This steep spectral index is consistent with synchrotron emission from an evolved shell-type SNR, where radiative energy losses have steepened the spectrum over time.

- 48.32+12.7: The source shows an extended structure. To estimate flux densities, a region was drawn around the 3 σ contour. The peak flux density was measured as 0.056 ± 0.006 mJy beam^{-1}, while the total flux within the 3 σ region was 0.301 ± 0.030 mJy, giving a flux ratio of 5.375 . This confirms that the source is extended rather than point-like. Using the peak flux together with the L-band flux, we calculated a spectral index of -1.733, pointing towards an SNR.

Table (4.1) summarizes the results of the newly detected sources. Given the steep spectral indices and their relatively high L-band fluxes, we conclude that these four sources are indeed newly detected SNRs within M82. The confirmation of their non-thermal nature provides further insights into the population of remnants within the galaxy, contributing to our understanding of its recent supernova activity and starburst-driven feedback processes.

4.3 Supernovae Rate in M82

There are various methods for measuring the supernova (SN) rate. Previous studies, such as that conducted by Muxlow et al. (1994), combined supernova remnant (SNR) luminosities and diameters to estimate the SN rate in M82. However, the accuracy of this approach has been questioned, as it relies on an estimate of the average expansion velocities of the SNRs. Expansion velocities are challenging to measure due to the possibility that SNRs expand into regions of varying densities. Using this method, Muxlow et al. (1994) determined a supernova rate of 0.05 year^{-1}.

The approach adopted in this study is based on SNR luminosities and is potentially more precise. The data presented in Table (3.1) provide the basis for estimating

© University of Pretoria

UNIVERSITEIT VAN PRETORIA
UNIVERSITY OF PRETORIA
YUNIBESITHI YA PRETORIA

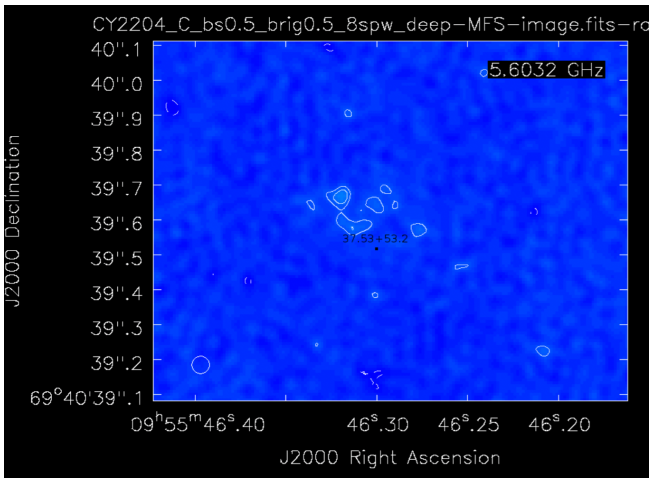

(1): 37.52+53.1

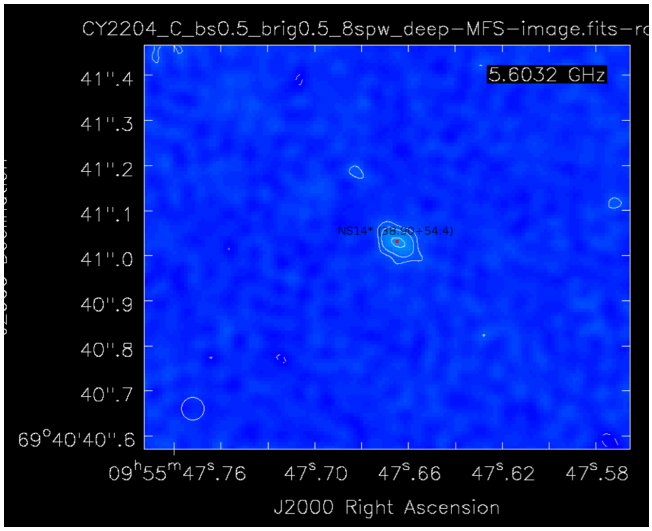

(3): 38.88+54.6

FIGURE 4.1: Contour maps of the newly detected sources as seen in the 2015 C-band data set. The contours are plotted at (for all images) C-band: (-3, 3, 5, 10)×12 μJy beam^{-1}.

the SN rate. To achieve this, flux density values were converted into luminosities, as shown in Table (3.3). These luminosities were then compared to that of Cassiopeia A, a well-studied Galactic SNR with a known age of approximately 350 years (Orlando et al., 2022). The similarity between Galactic SNRs and those in M82, inferred from the radio surface brightness–diameter ($\Sigma - D$) relation (Mills et al., 1984), enables a meaningful comparison between them.

The distance of a Galactic SNR is typically estimated using the $\Sigma - D$ relation. This relationship, which links the radio surface brightness at frequency ν to the SNR's diameter (Pavlovic et al., 2014), is expressed as

$$\Sigma_\nu(D) \;=\; AD^{-\beta}\,, \tag{4.1}$$

where A is thought to depend on various factors, including the SN explosion energy, the mass of ejected material, and interstellar medium (ISM) properties such as

© University of Pretoria

UNIVERSITEIT VAN PRETORIA
UNIVERSITY OF PRETORIA
YUNIBESITHI YA PRETORIA

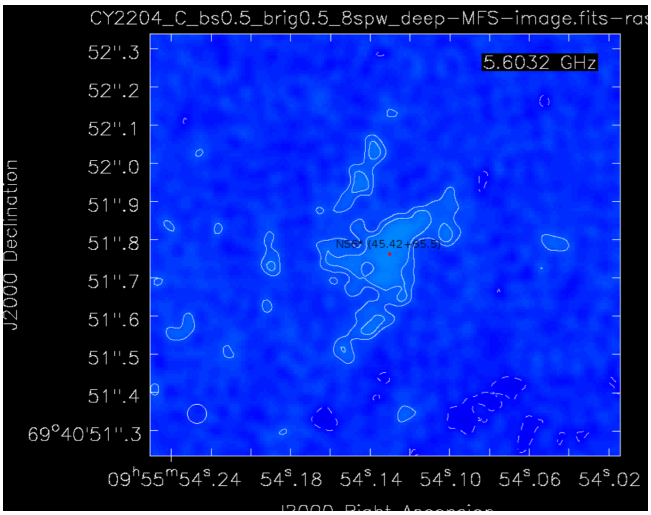

(26): 45.38+58.2

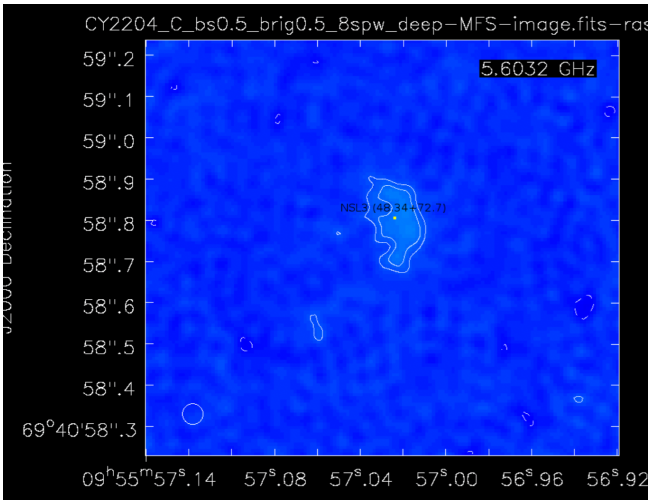

(35): 48.32+12.7

Figure 4.1 continued

density and magnetic field strength. The parameter β, however, is considered independent of these properties (Arbutina et al., 2004) and is explicitly dependent on the spectral index α of the integrated radio emission from the SNR (Pavlovic et al., 2014).

It is assumed that SNRs in M82 with luminosities exceeding that of Cassiopeia A are younger. Consequently, the supernova rate can be estimated using the relation:

$$\nu_{\mathrm{SN}} \approx \frac{\text{Number of SNRs above the Cassiopeia A luminosity}}{\text{Age of Cassiopeia A}} \,. \tag{4.2}$$

Cassiopeia A has an estimated luminosity of 6×10^{26} W (Pavlov and Luna, 2009). Since the observation in this study is at an observing frequency of 1.5 GHz with a bandwidth of 512 MHz, the bandwidth was used to estimate the spectral luminosity of Cassiopeia A,

$$L_{\nu,\mathrm{Cas\ A}} = \frac{L_{\mathrm{Cas\ A}}}{\Delta\nu} = \frac{6 \times 10^{26}\ \mathrm{W}}{512 \times 10^{6}\ \mathrm{Hz}} \approx 1.17 \times 10^{18}\ \mathrm{W\ Hz^{-1}} \,. \tag{4.3}$$

© University of Pretoria

UNIVERSITEIT VAN PRETORIA
UNIVERSITY OF PRETORIA
YUNIBESITHI YA PRETORIA

All 36 sources in this study have been identified as SNR candidates. Comparing the spectral luminosity of Cassiopeia A with the spectral luminosities of the 36 sources as seen in Table (3.3), whose luminosities range from $10^{43} - 10^{45}$ W Hz^{-1}, it is evident that the M82 SNRs are significantly more luminous. This suggests that they are much younger or intrinsically powerful than Cassiopeia A, reinforcing the notion that M82 is undergoing an intense period of star formation (SF) and SN activity.

Given that all 36 sources are much brighter than Cassiopeia A and that its age is approximately 350 years, this yields an SN rate of 0.102 year^{-1}. This estimate is in good agreement with previous calculations, including those of Fenech et al. (2008), who reported a rate of $0.07 - 0.08$ year^{-1}, and Allen (1999), who estimated 0.09 year^{-1}.

M82 is often considered a scaled-down version of Arp 220, a galaxy with a reported SN rate of 0.75 year^{-1} (Parra et al., 2007). Given that Arp 220's luminosity is approximately 50 times greater than that of M82, one might expect its SN rate to be similarly enhanced. However, the observed rate is significantly lower than this predicted value. It is worth noting that dust extinction may contribute to an underestimation of the true SN rate.

M82 can also be compared to other systems, such as Arp 299, a merging galaxy system located at a distance of 41 Mpc. Arp 299, which consists of two galaxies in an advanced state of merger, has an estimated SN rate of $0.5 - 1.0$ year^{-1} (Neff, Ulvestad, and Teng, 2004), a value comparable to that of Arp 220. Arp 299's luminosity is approximately 11 times greater than that of M82, so its SN rate should also be roughly 11 times higher, which is consistent with observations. These findings suggest that M82 and Arp 299 may share more similar characteristics than M82 and Arp 220.

4.4 Star Formation Rate in M82

The star formation rate (SFR) of M82 can be inferred from its supernova (SN) rate, providing a direct means of estimation. By considering the average formation rate of stars with masses exceeding 5 $M_\odot$ (Cram et al., 1998), If we assume a Miller-Scalo initial mass function (IMF; Miller and Scalo, 1979), and take lower and upper limits of stellar mass to range from 0.1 to 100 $M_\odot$ (Cram et al., 1998), the SN rate can be translated into a corresponding SFR following the relation (Condon, 1992)

$$\mathrm{SFR}(M \geq 5M_\odot) = 25\, \nu_{\mathrm{SN}}\, M_\odot \text{ year}^{-1}\,. \tag{4.4}$$

Substituting the SN rate (ν_{SN}) of 0.102 year^{-1}, as estimated in section 4.3, yields a SFR of 2.55 $M_\odot$year^{-1}. This aligns closely with previous determinations, including the $\sim 2\ M_\odot$ year^{-1} inferred from far-infrared (FIR), Hα, and ultraviolet (UV) observations (Young et al., 1996), as well as more recent estimates of $\sim$ 1.8–2 $M_\odot$ year^{-1} (Fenech et al., 2008). However, it is crucial to recognize that such models rely on the assumption of a constant SFR, which may not accurately reflect the dynamic nature of star formation (SF) in M82 (Gallagher, Hunter, and Tutukov, 1984).

One possibility is that the SFR in M82 fluctuates over timescales comparable to the lifetimes of massive stars. If this is the case, it could explain why the current SFR and SN rate appear slightly elevated relative to earlier estimates, suggesting that we may be observing a transient phase of heightened SF that could diminish over time. To confirm this hypothesis, future observations will be necessary to determine whether the trend persists or declines. Additionally, it is important to note that the integrated radio emission reflects a cumulative history of SF, capturing contributions

© University of Pretoria

UNIVERSITEIT VAN PRETORIA
UNIVERSITY OF PRETORIA
YUNIBESITHI YA PRETORIA

from supernovae (SNe) that have long since merged into the interstellar medium (ISM). Consequently, the observed supernova rate, and by extension, the inferred SF rate, could actually be decreasing over time.

© University of Pretoria

UNIVERSITEIT VAN PRETORIA
UNIVERSITY OF PRETORIA
YUNIBESITHI YA PRETORIA

Chapter 5

Conclusions

In this study, we aim to create a new catalogue of compact radio sources in the central starburst region of M82. The goal was to classify these sources as either supernova remnants (SNRs) or HII regions while also identifying possible new supernovae (SNe) and transient objects. By using high-resolution 1.5 GHz e-MERLIN L-Band observations from 2016, we were able to detect 36 compact sources. Among them, four had never been reported before. This is a significant discovery because it means that M82 is still an evolving galaxy with new sources appearing over time.

Our observations were very sensitive, allowing us to pick up faint signals. The RMS noise level of 59.36 µJy beam^{-1} meant that even weak radio sources could be detected. A clean beam size of 0.17 arcsec $\times$ 0.13 arcsec helped us see the details of these sources clearly. To make sure we only studied real sources and not noise, we applied a strict signal-to-noise ratio (S/N $\geq$ 6). This step ensured that the sources we detected were truly present and not just random fluctuations in the data.

One of the most important parts of this study was classifying these sources. We did this by studying their shapes and measuring their brightness at different frequencies. When we combined our new L-Band measurements with older C-Band data, we were able to confirm the identity of 31 sources that had been previously studied by Fenech et al. (2008). However, not all of them remained in the same category. The source 38.76 + 53.5, which had previously been labeled as an HII region, was reclassified as a SNR. This suggests that some past classifications may need to be revised and that additional studies at different wavelengths are needed.

The detection of four new sources (37.52+53.1, 38.88+54.6, 45.38+05.5, and 48.32+12.7) is particularly exciting. These sources had not been seen in previous studies, meaning they might be young SNRs that have only recently become bright enough to detect. If that is true, then M82 is still producing SNe at a high rate. This is important because SNe play a key role in shaping galaxies. They release huge amounts of energy, stir up gas clouds, and create new elements that will eventually form new stars and planets. By studying these newly detected sources over time, astronomers can learn more about how galaxies like M82 evolve and how often massive stars explode.

However, it is very likely that we have missed a considerable number of sources. Previous studies, such as those by Huang et al. (1994), Muxlow et al. (1994), and Fenech et al. (2008), reported over 50 compact sources in M82. The difference between our 36 detected sources and the more than 50 previously observed suggests that some sources may have fallen below our detection threshold due to sensitivity limitations, variations in observing frequencies, or changes in the emission of the sources themselves. Some SNRs can fade over time, while others may become visible at different frequencies, meaning that multi-wavelength studies are essential to fully cataloguing all sources in M82.

© University of Pretoria

UNIVERSITEIT VAN PRETORIA
UNIVERSITY OF PRETORIA
YUNIBESITHI YA PRETORIA

Another limitation is the nature of our observational setup. e-MERLIN, while providing excellent resolution, may not be as sensitive to extended emission as other radio interferometers with shorter baselines, such as the Very Large Array (VLA). This means that some diffuse emission sources or weakly emitting remnants could have gone undetected. Additionally, our strict $S/N \geq 6$ criterion ensures that we only include reliable detections, but it also means we may be missing real but faint sources near this threshold.

One of the most interesting sources in our study is 41.95+57.5. This source was first discovered in 1965 (Bash, 1968) and has been observed many times since then. It does not look like a typical SNR. Instead, it has two bright spots, which is unusual. Some scientists think it might be a special kind of explosion called a gamma-ray burst (GRB) afterglow (Muxlow et al., 2005). GRBs are some of the most powerful explosions in the universe, and they happen when massive stars collapse into black holes. If 41.95+57.5 is indeed a GRB afterglow, that would make M82 one of the closest galaxies to host such an event. On the other hand, it could still be a strange type of SNR, meaning that its explosion interacted with something in the galaxy in a unique way. Either way, this source remains a mystery, and more observations are needed to understand it.

Another key finding from this study was our confirmation of SN 2008iz as an SNR. This supernova was first detected in 2009 (Brunthaler et al., 2009a; Brunthaler et al., 2009b; Brunthaler et al., 2009c), but we were able to observe it again in 2016 and measure how it has changed. The fact that we can still see it means that the explosion left behind a dense cloud of material that continues to glow in radio waves. Its measured spectral index, $\alpha = -0.199$, suggests that synchrotron radiation is still the dominant process at work. This supports the idea that SN 2008iz is now in the later stages of its evolution, where its expanding shock wave is interacting with the surrounding interstellar medium.

A broader implication of this work is its contribution to estimating the SN rate in M82. Using our catalogue of sources and their radio brightness, we compared them to Cassiopeia A, a well-known SNR in our own Milky Way galaxy. This comparison helps estimate how often SNe occurs in M82. From our calculation we obtained a rate of 2.55 $M_{\odot}$ year^{-1}. This was found to be slightly higher compared to previous studies (Young et al., 1996; Fenech et al., 2008). However, this high rate of SNe is consistent with the idea that M82 is a starburst galaxy, meaning that it has a lot of young, massive stars that live fast and die young.

The findings of this study have several important implications. First, they confirm that M82 is still an active and evolving galaxy. The presence of newly detected SNRs means that massive stars are still exploding regularly. Second, the reclassification of some sources, such as 38.76+53.5, highlights the importance of multi-frequency observations in correctly identifying objects in space. Third, the continued evolution of sources like SN 2008iz and 41.95+57.5 shows that long-term monitoring is crucial to understanding how these objects change over time.

Future studies aimed at updating this catalogue should focus on deeper observations at even higher frequencies, such as C-Band and X-Band, to get a clearer picture of the spectral properties of these sources. Additionally, more VLBI studies could provide even better resolution, allowing us to resolve the fine details of the sources' structures. Finally, studying M82 in other wavelengths, such as infrared and X-ray, could help us learn more about the environments surrounding these sources and what role they play in the evolution of the galaxy.

In conclusion, this study has significantly expanded our understanding of the compact radio source population in M82. It has provided an updated catalogue,

© University of Pretoria

UNIVERSITEIT VAN PRETORIA
UNIVERSITY OF PRETORIA
YUNIBESITHI YA PRETORIA

identified new SNRs, corrected previous misclassifications, and contributed valuable data to the ongoing study of SN activity in starburst galaxies. These findings emphasize the dynamic and ever-changing nature of M82, highlighting its role as an excellent laboratory for studying star formation (SF), stellar evolution, and the impact of SNe on galactic environments.

© University of Pretoria

Chapter 6

Future Prospects

This study of compact radio sources in M82 helps to understand how supernova remnants (SNRs), HII regions, and star formation (SF) work in a starburst galaxy. This thesis identified and analyzed 36 compact sources using 1.5 GHz e-MERLIN observations. There are several ways to continue this research to learn more about radio sources in M82.

Long-Term Monitoring of Compact Radio Emission: The compact radio sources in starburst galaxies change over time, so long-term monitoring is important to track changes in brightness and structure. Argo (2006) presented a five-year monitoring programme using both MERLIN and the VLA to regularly observe a sample of nearby starburst galaxies, primarily to detect new radio supernovae (RSNe) missed by optical surveys and to monitor the flux densities of known SNRs. The programme also aimed to estimate star formation rates (SFR) and compare them with values obtained from other indicators. A similar approach, utilising e-MERLIN (which offers improved sensitivity over its predecessor MERLIN) and the European VLBI Network (EVN), could be used for monitoring the sources identified in this study. In this case, the EVN is preferred over the VLA due to its significantly higher angular resolution for compact sources. The EVN, comprising a network of telescopes across Europe and beyond, achieves angular resolutions down to 0.28 milliarcseconds at 43 GHz (Akiyama et al., 2022), making it the most sensitive VLBI array globally thanks to its collection of large telescopes (Baan et al., 2006). Some sources, like SN 2008iz and 41.95+57.5, are especially valuable to monitor due to their variable flux densities, which provide insight into their evolution. Additionally, continued observations of sources such as 38.76+53.5 could help confirm or refine their classifications.

Studying OH Masers: Argo (2006) also found OH masers in M82 and studied their relationship with SNRs and HII regions. This thesis focused on continuum radio sources, but future studies could also examine OH masers to learn more about SF and SNe activity. A future study could:

- Use past MERLIN and VLA data to find OH masers at 1665 and 1667 MHz.
- Compare the positions of masers and compact sources to see if they are related to SNRs or star-forming regions.
- Study gas movement using HI and CO data to understand how gas moves in M82's center.

Multi-Frequency and High-Resolution VLBI Observations: The spectral index analysis in this thesis helped classify sources, but observations at more frequencies and higher resolution can improve the results. Future work could use:

- Use EVN or global VLBI observations at L-band and C-band to study source structure and spectral properties.

© University of Pretoria

UNIVERSITEIT VAN PRETORIA
UNIVERSITY OF PRETORIA
YUNIBESITHI YA PRETORIA

- Compare radio sources with X-ray and infrared data to learn more about their nature.
- Continue monitoring 41.95+57.5 to find out if it is a SNR, a gamma-ray burst afterglow, or another type of transient source.

This thesis improved knowledge of compact radio sources in M82, but further work is needed to understand their changes over time, their connections to OH masers, and their role in SF. Future research using long-term monitoring, multiple wavelengths, and VLBI can help give a better picture of starburst galaxies like M82.

© University of Pretoria

UNIVERSITEIT VAN PRETORIA
UNIVERSITY OF PRETORIA
YUNIBESITHI YA PRETORIA

Bibliography

Akiyama, Kazunori et al. (Dec. 2022). "Overview of the Observing System and Initial Scientific Accomplishments of the East Asian VLBI Network (EAVN)". In: *Galaxies* 10.6, 113, p. 113. DOI: 10.3390/galaxies10060113. arXiv: 2212.07040 [astro-ph.IM].

Allen, M. L. and P. P. Kronberg (Jan. 1999). "Separation of Thermal and Non-Thermal Emission in the Nucleus of M82". In: *New Perspectives on the Interstellar Medium*. Ed. by A. R. Taylor, T. L. Landecker, and G. Joncas. Vol. 168. Astronomical Society of the Pacific Conference Series, p. 205.

Allen, Michael Leonard (Dec. 1999). "Radio continuum studies of the evolved starburst in M82". PhD thesis. University of Toronto, Canada.

Arbutina, B. et al. (May 2004). "L-D dependence for supernova remnants and its connection with the Σ-D relation". In: *MNRAS* 350.1, pp. 346–350. DOI: 10.1111/j.1365-2966.2004.07654.x.

Argo, Megan Kristy (Jan. 2006). "Radio studies of starburst galaxies". PhD thesis. University of Manchester, UK.

Armus, Lee, Timothy M. Heckman, and George K. Miley (Dec. 1990). "The Optical Emission-Line Nebulae of Powerful Far-Infrared Galaxies". In: *ApJ* 364, p. 471. DOI: 10.1086/169431.

Baan, Willem et al., eds. (Jan. 2006). *8th European VLBI Network Symposium*.

Bajaja, E. and G. D. van Albada (May 1979). "Complementing aperture synthesis radio data by short spacing components from single dish observations." In: *A&A* 75.1-2, pp. 251–254.

Bajkova, A. T. (Dec. 2008). "Multi-frequency synthesis of VLBI images using a generalized maximum entropy method". In: *Astronomy Reports* 52.12, pp. 951–962. DOI: 10.1134/S1063772908120019. arXiv: 0810.3304 [astro-ph].

Barger, A. J., L. L. Cowie, and E. A. Richards (May 2000). "Mapping the Evolution of High-Redshift Dusty Galaxies with Submillimeter Observations of a Radio-selected Sample". In: *AJ* 119.5, pp. 2092–2109. DOI: 10.1086/301341. arXiv: astro-ph/0001096 [astro-ph].

Barnes, Joshua E. (May 2004). "Shock-induced star formation in a model of the Mice". In: *MNRAS* 350.3, pp. 798–808. DOI: 10.1111/j.1365-2966.2004.07725.x. arXiv: astro-ph/0402248 [astro-ph].

Bartel, N. et al. (Nov. 1985). "Hubble's constant determined using very-long baseline interferometry of a supernova". In: *Nature* 318.6041, pp. 25–30. DOI: 10.1038/318025a0.

Bartel, N. et al. (Dec. 1987). "VLBI Observations of 23 Hot Spots in the Starburst Galaxy M82". In: *ApJ* 323, p. 505. DOI: 10.1086/165847.

Bash, F. N. (Nov. 1968). "Brightness Distributions of Radio Sources at 2695 MHz". In: *ApJS* 16, p. 373. DOI: 10.1086/190177.

Beck, S. C. et al. (Feb. 1996). "The Central Star Cluster of the Star-forming Dwarf Galaxy NGC 5253". In: *ApJ* 457, p. 610. DOI: 10.1086/176757.

Bell, A. R. (Jan. 1978). "The acceleration of cosmic rays in shock fronts - I." In: *MNRAS* 182, pp. 147–156. DOI: 10.1093/mnras/182.2.147.

© University of Pretoria

UNIVERSITEIT VAN PRETORIA
UNIVERSITY OF PRETORIA
YUNIBESITHI YA PRETORIA

Beswick, R. J. et al. (July 2006). "15 years of very long baseline interferometry observations of two compact radio sources in Messier 82". In: *MNRAS* 369.3, pp. 1221–1228. DOI: 10.1111/j.1365-2966.2006.10363.x. arXiv: astro-ph/0603629 [astro-ph].

Biermann, L. (Jan. 1955). "On the Mass Balance of the Interstellar Medium". In: *Gas Dynamics of Cosmic Clouds*. Vol. 2. IAU Symposium, p. 212.

Blumenthal, George R. and Robert J. Gould (Jan. 1970). "Bremsstrahlung, Synchrotron Radiation, and Compton Scattering of High-Energy Electrons Traversing Dilute Gases". In: *Reviews of Modern Physics* 42.2, pp. 237–271. DOI: 10.1103/RevModPhys.42.237.

Borkowski, K. M. and A. J. Kus (June 1983). "Very long baseline interferometry. I - an introduction". In: *Postepy Astronomii Krakow* 31, pp. 99–128.

Briggs, Daniel Shenon (Jan. 1995). "High fidelity deconvolution of moderately resolved sources". PhD thesis. New Mexico Institute of Mining and Technology.

Brown, R. Hanbury and C. Hazard (Jan. 1959). "The radio emission from normal galaxies, I. Observations of M31 and M33 at 158 Mc/s and 237 Mc/s". In: *MNRAS* 119, p. 297. DOI: 10.1093/mnras/119.3.297.

Brunthaler, A. et al. (May 2009a). "Discovery of a bright radio transient in M 82: a new radio supernova?" In: *A&A* 499.2, pp. L17–L20. DOI: 10.1051/0004-6361/200912327. arXiv: 0904.2388 [astro-ph.CO].

— (Apr. 2009b). "Discovery of a bright radio transient in M82: a new radio supernova?" In: *The Astronomer's Telegram* 2020, p. 1.

Brunthaler, A. et al. (May 2009c). "Supernova 2008iz in M82". In: *Central Bureau Electronic Telegrams* 1803, p. 1.

Brunthaler, A. et al. (June 2010). "VLBI observations of SN 2008iz. I. Expansion velocity and limits on anisotropic expansion". In: *A&A* 516, A27, A27. DOI: 10.1051/0004-6361/201014133. arXiv: 1003.4665 [astro-ph.CO].

Caldwell, Nelson and M. M. Phillips (Mar. 1989). "Star Formation in NGC 5253". In: *ApJ* 338, p. 789. DOI: 10.1086/167236.

Calzetti, Daniela et al. (Nov. 1997). "Dust and Recent Star Formation in the Core of NGC 5253". In: *AJ* 114, p. 1834. DOI: 10.1086/118609. arXiv: astro-ph/9708056 [astro-ph].

CASA Team et al. (Nov. 2022). "CASA, the Common Astronomy Software Applications for Radio Astronomy". In: *PASP* 134.1041, 114501, p. 114501. DOI: 10.1088/1538-3873/ac9642. arXiv: 2210.02276 [astro-ph.IM].

Chapman, S. C. et al. (Apr. 2005). "A Redshift Survey of the Submillimeter Galaxy Population". In: *ApJ* 622.2, pp. 772–796. DOI: 10.1086/428082. arXiv: astro-ph/0412573 [astro-ph].

Chevalier, R. A. (Aug. 1982a). "Are young supernova remnants interacting with circumstellar gas". In: *ApJ* 259, pp. L85–L89. DOI: 10.1086/183853.

— (Aug. 1982b). "The radio and X-ray emission from type II supernovae." In: *ApJ* 259, pp. 302–310. DOI: 10.1086/160167.

Condon, J. J. (Jan. 1992). "Radio emission from normal galaxies." In: *ARA&A* 30, pp. 575–611. DOI: 10.1146/annurev.aa.30.090192.003043.

Cottrell, G. A. (Mar. 1977). "21-cm observations of the interacting galaxies M81 and M82." In: *MNRAS* 178, pp. 577–589. DOI: 10.1093/mnras/178.4.577.

Cram, L. et al. (Nov. 1998). "Star Formation Rates in Faint Radio Galaxies". In: *ApJ* 507.1, pp. 155–160. DOI: 10.1086/306333. arXiv: astro-ph/9805327 [astro-ph].

Crutcher, R. M., D. H. Rogstad, and K. Chu (Nov. 1978). "Aperture-synthesis observations of H I in the galaxy M82." In: *ApJ* 225, pp. 784–789. DOI: 10.1086/156543.

© University of Pretoria

UNIVERSITEIT VAN PRETORIA
UNIVERSITY OF PRETORIA
YUNIBESITHI YA PRETORIA

Dewdney, P. E. et al. (Aug. 2009). "The Square Kilometre Array". In: *IEEE Proceedings* 97.8, pp. 1482–1496. DOI: 10.1109/JPROC.2009.2021005.

Dulk, G. A. (Jan. 1985). "Radio emission from the sun and stars." In: *ARA&A* 23, pp. 169–224. DOI: 10.1146/annurev.aa.23.090185.001125.

Eales, Stephen et al. (Apr. 1999). "The Canada-UK Deep Submillimeter Survey: First Submillimeter Images, the Source Counts, and Resolution of the Background". In: *ApJ* 515.2, pp. 518–524. DOI: 10.1086/307069. arXiv: astro-ph/9808040 [astro-ph].

Felli, M. et al. (Apr. 1993). "The radio continuum morphology of the Orion Nebula: from 10' to 0.1" resolution." In: *A&AS* 98, pp. 137–164.

Fenech, D. et al. (Oct. 2010). "Wide-field Global VLBI and MERLIN combined monitoring of supernova remnants in M82". In: *MNRAS* 408.1, pp. 607–621. DOI: 10.1111/j.1365-2966.2010.17144.x. arXiv: 1006.1504 [astro-ph.CO].

Fenech, D. M. et al. (Dec. 2008). "Deep MERLIN 5GHz radio imaging of supernova remnants in the M82 starburst". In: *MNRAS* 391.3, pp. 1384–1402. DOI: 10.1111/j.1365-2966.2008.13986.x. arXiv: 0810.0424 [astro-ph].

Fermi, Enrico (Apr. 1949). "On the Origin of the Cosmic Radiation". In: *Physical Review* 75.8, pp. 1169–1174. DOI: 10.1103/PhysRev.75.1169.

Filippenko, Alexei V. (Jan. 1997). "Optical Spectra of Supernovae". In: *ARA&A* 35, pp. 309–355. DOI: 10.1146/annurev.astro.35.1.309.

Fomalont, E. B. (Sept. 1973). "Earth-rotation aperture synthesis." In: *IEEE Proceedings* 61, pp. 1211–1218. DOI: 10.1109/PROC.1973.9247.

Freedman, Wendy L. et al. (June 1994). "The Hubble Space Telescope Extragalactic Distance Scale Key Project. I. The Discovery of Cepheids and a New Distance to M81". In: *ApJ* 427, p. 628. DOI: 10.1086/174172.

Gallagher III, J. S., D. A. Hunter, and A. V. Tutukov (Sept. 1984). "Star formation histories of irregular galaxies." In: *ApJ* 284, pp. 544–556. DOI: 10.1086/162437.

Garrington, Simon and Rob Beswick (June 2016). "The development of e-MERLIN". In: *Astronomy and Geophysics* 57.3, pp. 3.28–3.30. DOI: 10.1093/astrogeo/atw101.

Garrington, Simon T. et al. (Oct. 2004). "e-MERLIN". In: *Ground-based Telescopes*. Ed. by Jr. Oschmann Jacobus M. Vol. 5489. Society of Photo-Optical Instrumentation Engineers (SPIE) Conference Series, pp. 332–343. DOI: 10.1117/12.553235.

Gendre, M. A. et al. (May 2013). "Flux density variations of radio sources in M82 over the last three decades". In: *MNRAS* 431.2, pp. 1107–1120. DOI: 10.1093/mnras/stt231. arXiv: 1209.6478 [astro-ph.CO].

Giavalisco, M. et al. (Jan. 2004). "The Rest-Frame Ultraviolet Luminosity Density of Star-forming Galaxies at Redshifts z>3.5". In: *ApJ* 600.2, pp. L103–L106. DOI: 10.1086/381244. arXiv: astro-ph/0309065 [astro-ph].

Gioia, I. M., L. Gregorini, and U. Klein (Dec. 1982). "High frequency radio continuum observations of bright spiral galaxies". In: *A&A* 116.1, pp. 164–174.

Gorjian, Varoujan (Nov. 1996). "WFPC2 Imaging of the Starburst Galaxy NGC 5253". In: *AJ* 112, p. 1886. DOI: 10.1086/118150.

Gottesman, S. T. and L. Weliachew (Jan. 1977). "A high angular resolution study of the neutral hydrogen in the Irr II galaxy M82." In: *ApJ* 211, pp. 47–61. DOI: 10.1086/154902.

Green, D. A. (Jan. 2025). "An updated catalogue of 310 Galactic supernova remnants and their statistical properties". In: *Journal of Astrophysics and Astronomy* 46.1, 14, p. 14. DOI: 10.1007/s12036-024-10038-4. arXiv: 2411.03367 [astro-ph.GA].

Green, D. A. and S. F. Gull (Dec. 1984). "Two new young galactic supernova remnants". In: *Nature* 312.5994, pp. 527–529. DOI: 10.1038/312527a0.

© University of Pretoria

UNIVERSITEIT VAN PRETORIA
UNIVERSITY OF PRETORIA
YUNIBESITHI YA PRETORIA

Green, D. A. et al. (June 2008). "The radio expansion and brightening of the very young supernova remnant G1.9+0.3". In: *MNRAS* 387.1, pp. L54–L58. DOI: 10.1111/j.1745-3933.2008.00484.x. arXiv: 0804.2317 [astro-ph].

Hargrave, P. J. (Sept. 1974). "Observations of M82 at 5 GHz with the 5-km radio telescope". In: *MNRAS* 168, pp. 491–504. DOI: 10.1093/mnras/168.3.491.

Högbom, J. A. (June 1974). "Aperture Synthesis with a Non-Regular Distribution of Interferometer Baselines". In: *A&AS* 15, p. 417.

Hogbom, J. A. and W. N. Brouw (July 1974). "The Synthesis Radio Telescope at Westerbork. Principles of Operation, Performance and Data Reduction". In: *A&A* 33, p. 289.

Hopkins, Andrew M. and John F. Beacom (Nov. 2006). "On the Normalization of the Cosmic Star Formation History". In: *ApJ* 651.1, pp. 142–154. DOI: 10.1086/506610. arXiv: astro-ph/0601463 [astro-ph].

Houck, John C and Glenn E Allen (2006). "Models for nonthermal photon spectra". In: *The Astrophysical Journal Supplement Series* 167.1, p. 26.

Huang, Z. P. et al. (Mar. 1994). "Compact Radio Sources in the Starburst Galaxy M82 and the Sigma -D Relation for Supernova Remnants". In: *ApJ* 424, p. 114. DOI: 10.1086/173876.

Hughes, David H. et al. (July 1998). "High-redshift star formation in the Hubble Deep Field revealed by a submillimetre-wavelength survey". In: *Nature* 394.6690, pp. 241–247. DOI: 10.1038/28328. arXiv: astro-ph/9806297 [astro-ph].

James, J. F. (2011). *A Student's Guide to Fourier Transforms*.

James, Philip A and JP Anderson (2006). "The H Galaxy Survey-III. Constraints on supernova progenitors from spatial correlations with H emission". In: *Astronomy & Astrophysics* 453.1, pp. 57–65.

Katz, Neal (June 1992). "Dissipational Galaxy Formation. II. Effects of Star Formation". In: *ApJ* 391, p. 502. DOI: 10.1086/171366.

Kawara, Kimiaki, Minoru Nishida, and M. M. Phillips (Feb. 1989). "Brackett alpha and gamma Observations of Starburst and Seyfert Galaxies". In: *ApJ* 337, p. 230. DOI: 10.1086/167099.

Kennicutt Jr., Robert C. (May 1998). "The Global Schmidt Law in Star-forming Galaxies". In: *ApJ* 498.2, pp. 541–552. DOI: 10.1086/305588. arXiv: astro-ph/9712213 [astro-ph].

Kim, Ji-hoon, John H. Wise, and Tom Abel (Apr. 2009). "Galaxy Mergers with Adaptive Mesh Refinement: Star Formation and Hot Gas Outflow". In: *ApJ* 694.2, pp. L123–L127. DOI: 10.1088/0004-637X/694/2/L123. arXiv: 0902.3001 [astro-ph.GA].

Kimani, N. et al. (Aug. 2016). "Radio evolution of supernova SN 2008iz in M 82". In: *A&A* 593, A18, A18. DOI: 10.1051/0004-6361/201628800. arXiv: 1606.08742 [astro-ph.HE].

Kirk, J. G., P. Duffy, and Lewis Ball (Feb. 1994). "Radio Emission from SNR 1987A". In: *ApJS* 90, p. 807. DOI: 10.1086/191906.

Klein, U. and D. T. Emerson (Jan. 1981). "A survey of the distributions of 2.8 cm radio continuum in nearby galaxies." In: *A&A* 94, pp. 29–44.

Kronberg, P. P., P. Biermann, and F. R. Schwab (Apr. 1985). "The nucleus of M 82 at radio and X-ray bands : discovery of a new radio population of supernova candidates." In: *ApJ* 291, pp. 693–707. DOI: 10.1086/163108.

Kronberg, P. P. and R. A. Sramek (Jan. 1985). "Discovery of New Variable Radio Sources in the Nucleus of the nearby Galaxy Messier 82". In: *Science* 227.4682, pp. 28–31. DOI: 10.1126/science.227.4682.28.

© University of Pretoria

UNIVERSITEIT VAN PRETORIA
UNIVERSITY OF PRETORIA
YUNIBESITHI YA PRETORIA

Kronberg, Philipp P. (Jan. 1988). "The Starburst Galaxy M82". In: *Galactic and Extragalactic Star Formation*. Ed. by Ralph E. Pudritz and Michel Fich. Vol. 232. NATO Advanced Study Institute (ASI) Series C, p. 391. DOI: 10.1007/978-94-009-2973-9_24.

Larson, R. B. and B. M. Tinsley (Jan. 1978). "Star formation rates in normal and peculiar galaxies." In: *ApJ* 219, pp. 46–59. DOI: 10.1086/155753.

Lawrence, A. et al. (Apr. 1986). "Studies of IRAS sources at high galactic latitudes - II. Results froma redshift survey at b>60 : distribution in depth, luminosity function, and physical nature of IRAS galaxies." In: *MNRAS* 219, pp. 687–701. DOI: 10.1093/mnras/219.3.687.

Lilly, S. J. et al. (Mar. 1996). "The Canada-France Redshift Survey: The Luminosity Density and Star Formation History of the Universe to Z approximately 1". In: *ApJ* 460, p. L1. DOI: 10.1086/309975. arXiv: astro-ph/9601050 [astro-ph].

Longair, Malcolm S. (2011). *High Energy Astrophysics*.

Madau, Piero, Lucia Pozzetti, and Mark Dickinson (May 1998). "The Star Formation History of Field Galaxies". In: *ApJ* 498.1, pp. 106–116. DOI: 10.1086/305523. arXiv: astro-ph/9708220 [astro-ph].

Madau, Piero et al. (Dec. 1996). "High-redshift galaxies in the Hubble Deep Field: colour selection and star formation history to z$\sim$4". In: *MNRAS* 283.4, pp. 1388–1404. DOI: 10.1093/mnras/283.4.1388. arXiv: astro-ph/9607172 [astro-ph].

Marcaide, J. M. et al. (Sept. 1997). "Deceleration in the Expansion of SN 1993J". In: *ApJ* 486.1, pp. L31–L34. DOI: 10.1086/310830. arXiv: astro-ph/9708262 [astro-ph].

Marchili, N. et al. (Jan. 2010). "The radio lightcurve of SN 2008iz in M82 revealed by Urumqi observations". In: *A&A* 509, A47, A47. DOI: 10.1051/0004-6361/200913126. arXiv: 0909.5535 [astro-ph.CO].

Marr, Jonathan M., Ronald L. Snell, and Stanley E. Kurtz (2015). *Fundamentals of Radio Astronomy: Observational Methods (Series in Astronomy and Astrophysics)*.

Martí-Vidal, I. et al. (Feb. 2011a). "Radio emission of SN1993J: the complete picture. I. Re-analysis of all the available VLBI data". In: *A&A* 526, A142, A142. DOI: 10.1051/0004-6361/200913831. arXiv: 1007.2552 [astro-ph.HE].

— (Feb. 2011b). "Radio emission of SN1993J: the complete picture. II. Simultaneous fit of expansion and radio light curves". In: *A&A* 526, A143, A143. DOI: 10.1051/0004-6361/201014517. arXiv: 1007.1224 [astro-ph.HE].

Mattila, S. et al. (May 2013). "Supernovae and radio transients in M82". In: *MNRAS* 431.3, pp. 2050–2062. DOI: 10.1093/mnras/stt202. arXiv: 1207.1889 [astro-ph.CO].

McDonald, A. R. et al. (Mar. 2001). "Global very long-baseline interferometry observations of compact radio sources in M82". In: *MNRAS* 322.1, pp. 100–106. DOI: 10.1046/j.1365-8711.2001.04109.x. arXiv: astro-ph/0010466 [astro-ph].

McDonald, A. R. et al. (Aug. 2002). "A parsec-scale study of the 5/15-GHz spectral indices of the compact radio sources in M82". In: *MNRAS* 334.4, pp. 912–924. DOI: 10.1046/j.1365-8711.2002.05580.x. arXiv: astro-ph/0207158 [astro-ph].

Meurer, G. R. et al. (Dec. 1995). "Starbursts and Star Clusters in the Ultraviolet". In: *AJ* 110, p. 2665. DOI: 10.1086/117721. arXiv: astro-ph/9509038 [astro-ph].

Miller, G. E. and J. M. Scalo (Nov. 1979). "The Initial Mass Function and Stellar Birthrate in the Solar Neighborhood". In: *ApJS* 41, p. 513. DOI: 10.1086/190629.

Mills, B. Y. et al. (Jan. 1984). "A new look at radio supernova remnants." In: *Australian Journal of Physics* 37, pp. 321–357. DOI: 10.1071/PH840321.

Minkowski, R. (Aug. 1941). "Spectra of Supernovae". In: *PASP* 53.314, p. 224. DOI: 10.1086/125315.

© University of Pretoria

UNIVERSITEIT VAN PRETORIA
UNIVERSITY OF PRETORIA
YUNIBESITHI YA PRETORIA

Mohan, Niruj and David Rafferty (Feb. 2015). *PyBDSF: Python Blob Detection and Source Finder*. Astrophysics Source Code Library, record ascl:1502.007.

Moldon, Javier (Sept. 2021). *eMCP: e-MERLIN CASA pipeline*. Astrophysics Source Code Library, record ascl:2109.006. ascl: 2109.006.

Muxlow, T. W. B. et al. (Jan. 1994). "The structure of young supernova remnants in M82." In: *MNRAS* 266, pp. 455–467. DOI: 10.1093/mnras/266.2.455.

Muxlow, T. W. B. et al. (Jan. 2001). "VLBI observations of SNR in M82 - Is 41.95+575 an anomalous SNR or something else ?" In: *Galaxies and their Constituents at the Highest Angular Resolutions*. Ed. by R. T. Schilizzi. Vol. 205. IAU Symposium, p. 376.

Muxlow, T. W. B. et al. (Jan. 2005). "Is 41.95+575 in M82 actually an SNR? ." In: *Mem. Soc. Astron. Italiana* 76, p. 586.

Napier, P. J., A. R. Thompson, and R. D. Ekers (Nov. 1983). "The Very Large Array: design and performance of a modern synthesis radio telescope." In: *IEEE Proceedings* 71, pp. 1295–1320.

Napier, P. J. et al. (May 1994). "The Very Long Baseline Array." In: *IEEE Proceedings* 82.5, pp. 658–672. DOI: 10.1109/5.284733.

Neff, Susan G., James S. Ulvestad, and Stacy H. Teng (Aug. 2004). "A Supernova Factory in the Merger System Arp 299". In: *ApJ* 611.1, pp. 186–199. DOI: 10.1086/383608. arXiv: astro-ph/0406421 [astro-ph].

Norman, Colin et al. (June 2004). "The X-Ray-derived Cosmological Star Formation History and the Galaxy X-Ray Luminosity Functions in the Chandra Deep Fields North and South". In: *ApJ* 607.2, pp. 721–738. DOI: 10.1086/383487. arXiv: astro-ph/0402140 [astro-ph].

O'Connell, R. W. and J. J. Mangano (Apr. 1978). "The central regions of M82." In: *ApJ* 221, pp. 62–79. DOI: 10.1086/156005.

O'Dell, C. R. (Jan. 2001). "The Orion Nebula and its Associated Population". In: *ARA&A* 39, pp. 99–136. DOI: 10.1146/annurev.astro.39.1.99.

Offringa, A. R., B. McKinley, Hurley-Walker, et al. (2014). "WSClean: an implementation of a fast, generic wide-field imager for radio astronomy". In: *MNRAS* 444.1, pp. 606–619. DOI: 10.1093/mnras/stu1368.

Offringa, A. R. and O. Smirnov (2017). "An optimized algorithm for multiscale wideband deconvolution of radio astronomical images". In: *MNRAS* 471.1, pp. 301–316. DOI: 10.1093/mnras/stx1547.

Orlando, S. et al. (Oct. 2022). "Evidence for past interaction with an asymmetric circumstellar shell in the young SNR Cassiopeia A". In: *A&A* 666, A2, A2. DOI: 10.1051/0004-6361/202243258. arXiv: 2202.01643 [astro-ph.HE].

Pacholczyk, A. G. (1970). *Radio astrophysics. Nonthermal processes in galactic and extragalactic sources*.

Paczyński, Bohdan (Feb. 1998). "Are Gamma-Ray Bursts in Star-Forming Regions?" In: *ApJ* 494.1, pp. L45–L48. DOI: 10.1086/311148. arXiv: astro-ph/9710086 [astro-ph].

Panagia, Nino et al. (Aug. 2007). "Radio Observations of Supernovae". In: *The Multicolored Landscape of Compact Objects and Their Explosive Origins*. Ed. by Tiziana di Salvo et al. Vol. 924. American Institute of Physics Conference Series. AIP, pp. 407–414. DOI: 10.1063/1.2774888. arXiv: astro-ph/0703411 [astro-ph].

Parra, Rodrigo et al. (Apr. 2007). "The Radio Spectra of the Compact Sources in Arp 220: A Mixed Population of Supernovae and Supernova Remnants". In: *ApJ* 659.1, pp. 314–330. DOI: 10.1086/511813. arXiv: astro-ph/0612248 [astro-ph].

Pavlov, G. G. and G. J. M. Luna (Sept. 2009). "A Dedicated Chandra ACIS Observation of the Central Compact Object in the Cassiopeia A Supernova Remnant". In:

© University of Pretoria

UNIVERSITEIT VAN PRETORIA
UNIVERSITY OF PRETORIA
YUNIBESITHI YA PRETORIA

ApJ 703.1, pp. 910–921. DOI: 10.1088/0004-637X/703/1/910. arXiv: 0905.3190 [astro-ph.HE].

Pavlovic, M. Z. et al. (Dec. 2014). "Updated Radio Sigma-D Relation for Galactic Supernova Remnants". In: *Serbian Astronomical Journal* 189, pp. 25–40. DOI: 10.2298/SAJ1489025P. arXiv: 1411.2234 [astro-ph.HE].

Pedlar, A. et al. (Aug. 1999). "VLBI observations of supernova remnants in Messier 82". In: *MNRAS* 307.4, pp. 761–768. DOI: 10.1046/j.1365-8711.1999.02642.x.

Readhead, A. C. S. and P. N. Wilkinson (July 1978). "The mapping of compact radio sources from VLBI data." In: *ApJ* 223, pp. 25–36. DOI: 10.1086/156232.

Reynolds, S. P. (Sept. 2008). "Supernova remnants at high energy." In: *ARA&A* 46, pp. 89–126. DOI: 10.1146/annurev.astro.46.060407.145237.

Reynolds, Stephen P. et al. (June 2008). "The Youngest Galactic Supernova Remnant: G1.9+0.3". In: *ApJ* 680.1, p. L41. DOI: 10.1086/589570. arXiv: 0803.1487 [astro-ph].

Rieke, G. H. and M. J. Lebofsky (May 1986). "The Luminosity Function for Field Galaxies in the Infrared". In: *ApJ* 304, p. 326. DOI: 10.1086/164167.

Rieke, G. H., M. J. Lebofsky, and C. E. Walker (Feb. 1988). "NGC 253 and a Proposed Sequence for Nuclear Starbursts". In: *ApJ* 325, p. 679. DOI: 10.1086/166038.

Rieke, G. H. et al. (May 1980). "The nature of the nuclear sources in M82 and NGC 253". In: *ApJ* 238, pp. 24–40. DOI: 10.1086/157954.

Rybicki, George B. and Alan P. Lightman (1986). *Radiative Processes in Astrophysics*.

Saitoh, Takayuki R. et al. (June 2009). "Toward First-Principle Simulations of Galaxy Formation: II. Shock-Induced Starburst at a Collision Interface during the First Encounter of Interacting Galaxies". In: *PASJ* 61, p. 481. DOI: 10.1093/pasj/61.3.481. arXiv: 0805.0167 [astro-ph].

Sanders, D. B. et al. (Feb. 1988a). "Ultraluminous Infrared Galaxies and the Origin of Quasars". In: *ApJ* 325, p. 74. DOI: 10.1086/165983.

Sanders, D. B. et al. (May 1988b). "Warm Ultraluminous Galaxies in the IRAS Survey: The Transition from Galaxy to Quasar?" In: *ApJ* 328, p. L35. DOI: 10.1086/185155.

Sanders, David B., Jason Surace, and Catherine Mie Ishida (1999). "Ultraluminous infrared galaxies". In: URL: https://api.semanticscholar.org/CorpusID:14294774.

Schweizer, François (2009). "Globular Cluster Formation in Mergers". In: *Globular Clusters - Guides to Galaxies*. Ed. by Tom Richtler and Søren Larsen, p. 331. DOI: 10.1007/978-3-540-76961-3_78.

Smail, Ian, R. J. Ivison, and A. W. Blain (Nov. 1997). "A Deep Sub-millimeter Survey of Lensing Clusters: A New Window on Galaxy Formation and Evolution". In: *ApJ* 490.1, pp. L5–L8. DOI: 10.1086/311017. arXiv: astro-ph/9708135 [astro-ph].

Springel, Volker, Tiziana Di Matteo, and Lars Hernquist (Aug. 2005). "Modelling feedback from stars and black holes in galaxy mergers". In: *MNRAS* 361.3, pp. 776–794. DOI: 10.1111/j.1365-2966.2005.09238.x. arXiv: astro-ph/0411108 [astro-ph].

Springel, Volker and Lars Hernquist (Feb. 2003). "Cosmological smoothed particle hydrodynamics simulations: a hybrid multiphase model for star formation". In: *MNRAS* 339.2, pp. 289–311. DOI: 10.1046/j.1365-8711.2003.06206.x. arXiv: astro-ph/0206393 [astro-ph].

Steidel, Charles C. et al. (July 1999). "Lyman-Break Galaxies at z>∼4 and the Evolution of the Ultraviolet Luminosity Density at High Redshift". In: *ApJ* 519.1, pp. 1–17. DOI: 10.1086/307363. arXiv: astro-ph/9811399 [astro-ph].

Stinson, Greg et al. (Dec. 2006). "Star formation and feedback in smoothed particle hydrodynamic simulations - I. Isolated galaxies". In: *MNRAS* 373.3, pp. 1074–

© University of Pretoria

UNIVERSITEIT VAN PRETORIA
UNIVERSITY OF PRETORIA
YUNIBESITHI YA PRETORIA

1090. DOI: 10.1111/j.1365-2966.2006.11097.x. arXiv: astro-ph/0602350 [astro-ph].

Sugimoto, D., D. Q. Lamb, and D. N. Schramm, eds. (Jan. 1981). *Fundamental problems in the theory of stellar evolution*. Vol. 93. IAU Symposium.

Thackeray, A. D. (Feb. 1948). "On some possible evolutionary trends in the interstellar medium". In: *The Observatory* 68, pp. 22–26.

Thomasson, Peter (Sept. 1986). "MERLIN." In: *QJRAS* 27, pp. 413–431.

Thompson, A. Richard, James M. Moran, and Jr. Swenson George W. (2017). *Interferometry and Synthesis in Radio Astronomy, 3rd Edition*. DOI: 10.1007/978-3-319-44431-4.

Turner, Jean L., Sara C. Beck, and Robert L. Hurt (Jan. 1997). "A CO Map of the Dwarf Starburst Galaxy NGC 5253". In: *ApJ* 474.1, pp. L11–L14. DOI: 10.1086/310412.

Turner, Jean L., Paul T. P. Ho, and Sara C. Beck (Sept. 1998). "The Radio Properties of NGC 5253 and Its Unusual H II Regions". In: *AJ* 116.3, pp. 1212–1220. DOI: 10.1086/300485.

Ulvestad, James S. and Robert R. J. Antonucci (Mar. 1994). "Do the Compact Radio Sources in NGC 253 and M82 Fade over Time?" In: *ApJ* 424, p. L29. DOI: 10.1086/187267.

van den Bergh, S. (Jan. 1957). "Interstellar Gas and Star Creation". In: *Z. Astrophys.* 43, p. 236.

Vink, Jacco (Dec. 2012). "Supernova remnants: the X-ray perspective". In: *A&ARv* 20, 49, p. 49. DOI: 10.1007/s00159-011-0049-1. arXiv: 1112.0576 [astro-ph.HE].

Ward-Thompson, Derek and Anthony P. Whitworth (2011). *An Introduction to Star Formation*.

Weedman, Daniel W. (May 1987). "Starburst Galaxies". In: *NASA Conference Publication*. Ed. by Carol J. Lonsdale Persson. Vol. 2466. NASA Conference Publication, pp. 351–361.

Weiler, Kurt W., Nino Panagia, and Richard A. Sramek (Dec. 1990). "Radio Emission from Supernovae. II. SN 1986J: A Different Kind of Type II". In: *ApJ* 364, p. 611. DOI: 10.1086/169444.

Weiler, Kurt W. et al. (Jan. 2002). "Radio Emission from Supernovae and Gamma-Ray Bursters". In: *ARA&A* 40, pp. 387–438. DOI: 10.1146/annurev.astro.40.060401.093744.

Whipple, Fred L. (July 1946). "Concentrations of the Interstellar Medium." In: *ApJ* 104, p. 1. DOI: 10.1086/144829.

Wilkinson, P. N. and A. G. de Bruyn (Feb. 1990). "Shell-like structure in 41.9+58, a powerful supernova remnant in M 82." In: *MNRAS* 242, pp. 529–534. DOI: 10.1093/mnras/242.4.529.

Williams, Jonathan P. and Christopher F. McKee (Feb. 1997). "The Galactic Distribution of OB Associations in Molecular Clouds". In: *ApJ* 476.1, pp. 166–183. DOI: 10.1086/303588.

Wills, K. A. et al. (Nov. 1997). "Low-frequency observations of supernova remnants in M82". In: *MNRAS* 291.3, pp. 517–526. DOI: 10.1093/mnras/291.3.517.

Wilson, Gillian et al. (Sept. 2002). "Star Formation History since z=1.5 as Inferred from Rest-Frame Ultraviolet Luminosity Density Evolution". In: *AJ* 124.3, pp. 1258–1265. DOI: 10.1086/341818. arXiv: astro-ph/0203168 [astro-ph].

Wilson, T. L. and D. Downes (1975). *H II regions and related topics*. Vol. 42. DOI: 10.1007/3-540-07409-0.

Wilson, Thomas L., Kristen Rohlfs, and Susanne Hüttemeister (2013). *Tools of Radio Astronomy*. DOI: 10.1007/978-3-642-39950-3.

© University of Pretoria

UNIVERSITEIT VAN PRETORIA
UNIVERSITY OF PRETORIA
YUNIBESITHI YA PRETORIA

Woosley, S. E., R. E. Taam, and T. A. Weaver (Feb. 1986). "Models for Type I Supernova. I. Detonations in White Dwarfs". In: *ApJ* 301, p. 601. DOI: 10.1086/163926.

Wright, E. L. (Dec. 2006). "A Cosmology Calculator for the World Wide Web". In: *PASP* 118.850, pp. 1711–1715. DOI: 10.1086/510102. arXiv: astro-ph/0609593 [astro-ph].

Yan, Lin et al. (July 1999). "The Hα Luminosity Function and Global Star Formation Rate from Redshifts of 1-2". In: *ApJ* 519.1, pp. L47–L50. DOI: 10.1086/312099. arXiv: astro-ph/9904427 [astro-ph].

Young, Judith S. et al. (Nov. 1996). "The Global Rate and Efficiency of Star Formation in Spiral Galaxies as a Function of Morphology and Environment". In: *AJ* 112, p. 1903. DOI: 10.1086/118152.

Yun, M. S., P. T. P. Ho, and K. Y. Lo (Dec. 1994). "A high-resolution image of atomic hydrogen in the M81 group of galaxies". In: *Nature* 372.6506, pp. 530–532. DOI: 10.1038/372530a0.

Zensus, J. A. and E. Ros (Jan. 2015). "European VLBI Network: Present and Future". In: *arXiv e-prints*, arXiv:1501.05079, arXiv:1501.05079. DOI: 10.48550/arXiv.1501.05079. arXiv: 1501.05079 [astro-ph.IM].

© University of Pretoria